WEARABLE BIO-IMPEDANCE SENSING METHODS FOR CONTINUOUS MONITORING OF HEMODYNAMIC PARAMETERS

A Dissertation

by

BASSEM AHMED ZAKI IBRAHIM

Submitted to the Graduate and Professional School of
Texas A&M University
in partial fulfillment of the requirements for the degree of

DOCTOR OF PHILOSOPHY

Chair of Committee,	Roozbeh Jafari
Committee Members,	Jose Silva-Martinez
	Jiang Hu
	Srinivas Shakkottai
	John C. Criscione
Head of Department,	Miroslav M. Begovic

December 2021

Major Subject: Computer Engineering

ABSTRACT

Continuous monitoring of hemodynamic parameters such as blood pressure (BP) provides significant advantages in predicting future cardiovascular disease. Traditional BP measurement methods are based on a cuff, which is bulky, obtrusive, and not applicable to continuous monitoring. Measurement of blood pulsatile is one of the prominent cuffless methods for continuous BP monitoring. The pulse morphology and pulse transit time (PTT) which is the time taken by the pressure pulse to travel between two points in an arterial vessel are highly correlated with the BP. In this dissertation, we present a new cuffless BP method using an array of wrist-worn bio-impedance (Bio-Z) sensors placed on the wrist arteries to monitor the arterial pressure pulse from the blood volume changes. The Bio-Z sensing method is a non-invasive technique that can measure blood volume changes by injecting alternating current (AC) signal that flows deep into the tissue via a pair of electrodes and then, sensing the potential difference on another pair. We present the design of our custom Bio-Z sensing hardware and electrode array wristband that provide high-quality pulse signals through multi-channel Bio-Z sensing from the wrist. BP is accurately estimated by using the AdaBoost regression model based on selected arterial pressure pulse features. Post-exercise BP was accurately estimated with an average correlation coefficient of 0.77 for the diastolic BP and 0.86 for the systolic BP. In addition, we present a Bio-Z simulation platform that models the tissue and arterial pulse wave using a 3D circuit model based on a time-varying impedance grid. The proposed model will enable researchers to create time-varying blood flow models and rapidly test the effectiveness of the sensing methods and algorithms without the need for extensive experimentation. Furthermore, we propose a new multi-source multi-frequency Bio-Z sensing method that provides more localized pulsatile monitoring for improved PTT. Another Bio-Z method is proposed based on a convolutional neural network (CNN) autoencoder that estimates an accurate arterial pulse signal independent of sensing location from multiple pulse signals. The proposed methods contribute to reliable and accurate continuous monitoring of hemodynamic parameters from wrist-worn devices, which can contribute to more effective monitoring and management of the cardiovascular disease.

ACKNOWLEDGEMENTS

I would like to thank my committee chair, Dr. Roozbeh Jafari, and my committee members Dr. Jose Silva-Martinez, Dr. Jiang Hu, Dr. Srinivas Shakkottai and, Dr. John C. Criscione for their guidance and support throughout the course of this research.

Thanks also go to my friends and colleagues and the department faculty and staff for making my time at Texas A&M University a great experience.

Finally, thanks to my mother and father for their encouragement and to my wife for her patience and love.

CONTRIBUTORS AND FUNDING SOURCES

Contributors

This work was supervised by a dissertation committee consisting of Professor Roozbeh Jafari and Professors Jose Silva-Martinez, Jiang Hu, and Srinivas Shakkottai of the Department of Electrical and Computer Engineering and Professor John C. Criscione of the Department of Biomedical Engineering.

All work conducted for the dissertation was completed by the student independently.

Funding Sources

This work was supported in part by the National Institutes of Health, under Grants 1R01EB028106-01 and 1R01HL151240-01A1. Its contents are solely the responsibility of the authors and do not necessarily represent the official views of the National Institutes of Health.

TABLE OF CONTENTS

Page

LIST OF FIGURES

Page

LIST OF TABLES

Page

1. INTRODUCTION

1.1. Objectives

The main objective of our research is to enable continuous monitoring of hemodynamic parameters with a focus on cuffless blood pressure monitoring in order to improve the management and diagnosis of cardiovascular disease. Our approach is based on extracting blood pressure features from multiple arterial pulse signals using an array of bio-impedance sensors placed on the wrist that can be integrated into wrist-worn devices which are the most common and comfortable wearable devices for daily usage such as smart watches.

Cardiovascular disease is the leading global cause of death, accounting for more than 17.3 million deaths per year in 2013 (31% of all global deaths), a number that is expected to grow to more than 23.6 million by 2030. In 2010, the estimated global cost of cardiovascular disease was $863 billion, and it is estimated to rise to $1044 billion by 2030 according to the predictions of the American Heart Association. Hemodynamic parameters such as blood pressure and cardiac output provide prognostic information regarding cardiovascular risk, which helps clinicians in choosing effective treatment options for their patients. Blood pressure (BP) is a leading risk factor for the prediction of cardiovascular disease. Many studies have now confirmed that ambulatory BP measured continuously every half-hour over a 24-hour period is better than traditional office-based BP measurement in predicting future cardiovascular events. Moreover, the nighttime pressure is superior to daytime pressure in predicting cardiovascular disease. BP is commonly measured by a sphygmomanometer or oscillometric method using an inflatable cuff which is bulky, obtrusive and allows only sporadic measurements. Therefore, cuffless BP monitoring methods are essential to achieving continuous BP measurement during daily activities and sleeping in order to provide better predictions for cardiovascular disease. Our objective in this research is to develop a cuffless BP monitoring method for a wrist-worn device, which is comfortable and easy-to-use to provide continuous and accurate BP measurements autonomously without user intervention. A prominent method for continuous BP monitoring without using a cuff is pulse transit time (PTT) [7]. This method relies on modeling the correlation between BP and PTT which is the time taken by the pressure pulse to travel through the arteries between two fixed points during each cardiac cycle. PTT increases as BP decreases according to Moens–Korteweg equation [8]. The pressure pulse can be measured by bio-impedance (Bio-Z) signal which is an electrical non-invasive signal measured by injecting AC current in the human body and sensing the voltage difference using separate pairs of electrodes. The changes in bio-impedance over time (ΔBio-Z) corresponds to the blood volume changes inside the arteries at the sensing location, which is used to measure the arterial pressure pulse. Bio-impedance has wide applications in monitoring health parameters such as respiration rate and body dehydration in addition to imaging methods such as electrical impedance tomography (EIT) [9]. Bio-Z signal provides a more accurate and reliable measurement of arterial blood volume changes compared to other modalities such as photoplethysmography (PPG) signal. The injected current from the Bio-Z sensor can reach deeper tissue compared to the propagation depth of light used by PPG sensors. In addition, bio-impedance is not affected by ambient light and skin tone, which affect the PPG signal. Bio-impedance sensors are suitable for wearable devices because they are low power, low cost, and portable and often can be placed in a small form factor. Additionally, bio-impedance offers the possibility of imaging, for example, to identify the location of arteries, leveraging an array of voltage sensors and activating current sources in specific patterns.

1.2. Previous Work

The high potential for using PTT method for continuous BP measurement has led to significant interest in the research community. The predominant method of estimating PTT in the literature measures the time delay between each R-peak of the electrocardiogram (ECG) signal and a characteristic point on a corresponding pulse wave measured by a distally placed sensor of a different modality, e.g., photoplethysmography (PPG) or bio-impedance (Bio-Z) [4, 5, 7, 10-12]. These PTT measurement methods rely on ECG, which has two main issues. First, ECG is monitored from the potential between two electrodes across the two sides of the heart, which can be realized in a small form factor device as a chest patch. However, this patch is not conveniently wearable and cannot be integrated with the distal pulse arrival sensor in a single wearable device. Second, the time delay measured using ECG includes the pre-ejection period (PEP), which is the time from the onset of the R-peak to the start of the physical pumping of blood out of the heart. PEP is not included in PTT and is not correlated with BP, which leads to higher errors in BP estimation [13]. In a previous study, a wrist-worn device was used to monitor BP based on PTT measured from ECG and PPG signals. However, the user needs to press a finger on an electrode on the device to get a measurement by monitoring ECG between both hands [14]. BP was also monitored through a watch using seismocardiogram (SCG) and PPG sensors only when the user holds his arm with the watch towards his chest for a specific time [15]. In another prior investigation, BP was measured without ECG using PTT calculated from dual PPG sensors placed on the forearm and the wrist with 17cm distance between them, which cannot fit in a small form factor wearable device [16]. In a more recent investigation, a smartphone-based approach was used to measure BP via the oscillometric finger-pressing method, which requires the user to press his finger towards a PPG sensor with gradual pressure increase constrained by a specific range [17]. These methods, although providing interesting and important insights into BP monitoring, are not applicable for continuous BP monitoring because they require user intervention or cannot be incorporated into a smart watch form factor for a true wearable experience. A recent investigation estimated BP using PTT measured from a pair of bio-impedance sensors placed on the wrist where each sensor covers both arteries [6]. This method measures a global PTT from both arteries, which results in a larger BP error compared to our approach that depends on local measurements from each artery.

PPG sensors are commonly used for measuring hemodynamic parameters including heart rate, PTT, and cuffless BP monitoring leveraging optics. In previous work, a multi-wavelength PPG sensor on the finger was used to measure the pulse delay through the arterioles and the capillaries, which was found to be correlated to BP [18]. On the other side, the proposed approach depends on measuring the pulse transit time through the arteries, which are the main blood vessels that branch into multiple smaller arterioles,

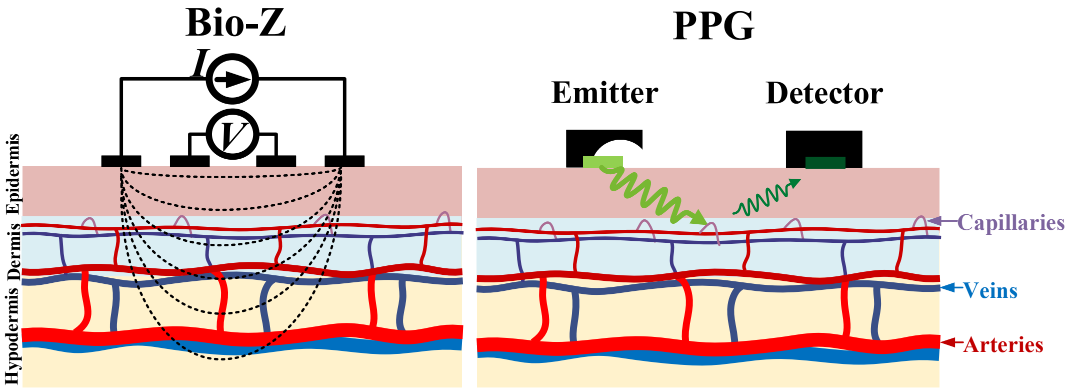

Figure 1. (a) Shallow penetration of the optical PPG sensor, which can only detect the blood pulse at the capillaries, (b) Deep penetration of the current signal of bio-impedance sensor, which reaches the arteries and detect arterial pulse wave; therefore, can provide an accurate estimation for blood pressure.

which branch into further smaller capillaries. BP is mainly controlled by the stiffness of the arteries rather than the arterioles and the capillaries. In the arteries, the pulse pressure (PP) and blood velocity near the heart are very high and decrease in the arterioles and the capillaries where the rate of flow is slowed by the narrow openings of the arterioles and the capillaries till BP becomes constant inside the capillaries. Therefore, the estimation of pulse transit time through the arteries is more accurate than the arterioles and the capillaries. In addition, the challenge with optical modalities is the light cannot travel far and can only capture blood volume changes in skin surface (i.e. from capillaries). On the other hand, since Bio-Z injects a current, it can reach deeper tissue compared to the propagation depth of light used by PPG sensors as shown in Figure 1. Thus, the Bio-Z signal provides a more accurate measurement of arterial blood volume changes since it can reach deep arterial sites. PPG signals can be affected by ambient light and skin tone, which is not applicable for bio-impedance. In addition, the PPG signal requires optical components such as a light source and a photo detector, which consume large power to penetrate the skin.

Other pulse waveform measurement methods are available such as flexible strain or pressure sensors placed over a superficial artery, which can measure waveforms indicative of BP via the tonometric principle [19]. The strain sensor measures the force on the skin surface due to the pulsation of the artery that is deep inside the tissue. Therefore, the measured signal is corrupted by external sources of skin movements such as muscle contractions. On the other side, the Bio-Z sensor injects current into the body and senses the voltage difference using separate pairs of electrodes (4-probe Kelvin sensing) to measures the impedance of the underlying tissue and blood volume changes inside the arteries with the minimum effect from skin surface movements.

Recently, an ultra-thin ultrasound device was presented for cuffless BP monitoring by measuring blood flow velocity [20]. However, ultrasound methods use a highly directive beam, which is extremely sensitive to the placement location of the device relative to the artery, and require an expert to place the sensor directly over the artery to get the arterial pulse signal. On the other side, the Bio-Z sensor has lower directivity, which makes it less sensitive to the artery's location. In addition, the Bio-Z sensor has lower power consumption compared to ultrasound because Bio-Z operates at a low frequency of a few kHz compared to a few MHz for ultrasound. Furthermore, the simplicity of the hardware implementation of the Bio-Z sensor is preferable for our method, which relies on an array of sensors integrated into a small-form factor wearable device.

1.3. Approach

The objective of this dissertation is to develop the first wearable device that demonstrates the effectiveness of the array of bio-impedance sensors to measure blood pressure and other physiological phenomena. The bio-impedance sensor is designed using low-noise analog front-end, digital synchronous demodulation and digital signal processing algorithms to detect accurately small variations as low as 50mΩ with resistance resolution better than 1mΩ and small delays less than 10ms with a time resolution better than 0.1ms [21, 22]. Multi-channel bio-impedance sensing is implemented and synchronized together to measure simultaneous pulse signals from the array of electrodes. Furthermore, different types of wet and dry electrodes are considered by studying their electrode-skin impedance as a measure of contact quality in the presence of wrist movements in order to provide a reliable and friendly interface between the skin and the device.

In addition, a simulation platform for bio-impedance is developed to model the tissue and the blood flow in the arteries using a 3D time-varying impedance grid to model dynamic activity inside the body [23]. We model the body tissue using a 3D grid of small, interconnect, time-varying impedance elements (voxels). Each voxel consists of the equivalent circuit of cells within tissues. A parameterized SPICE model describes the geometry and conductivity of the modeled tissue, diameter, depth, and location of the arteries, and the location and spacing of the electrodes on the skin. The proposed model

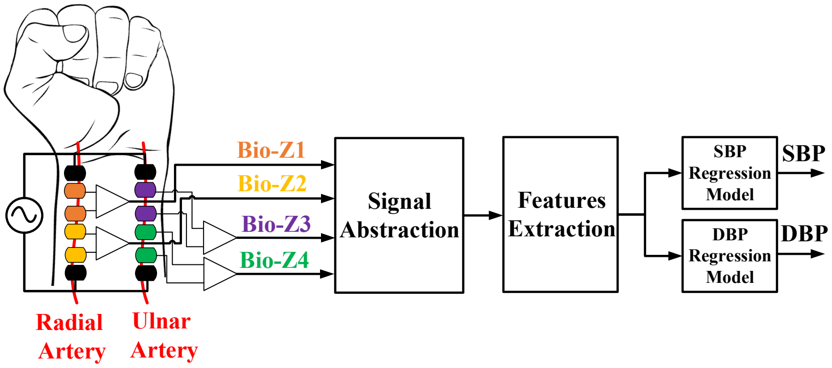

Figure 2. The block diagram of the BP estimation hardware and signal processing from wrist-worn bio-impedance sensors array.

can be integrated with the sensing circuits in SPICE simulations using our source code, which is available online to help designers and researchers understand design decisions and tradeoffs. The simulation platform is able to show how the sensed bio-impedance pulse signal is affected by the sensing electrodes' size and spacing, and the artery's location, diameter, and depth. As a result, we can optimize our sensing and signal processing methods to improve the measurement of the arterial pulse signal in order to enhance hemodynamics parameters monitoring.

For BP estimation, our approach is based on placing an array of sensors on the wrist arteries, which provide local measurements of the cardiac activity of both the radial and ulnar arteries for accurate estimation of the PTT and consequently the BP [1, 24, 25]. In our approach, we use a model for the vascular properties of the radial and ulnar arteries of the wrist to estimate the systolic and diastolic BP by subject-specific regression model based on PTT and other features extracted from a 2×2 array of bio-impedance sensors placed on the wrist arteries as shown in Figure 2. A pair of bio-impedance sensors are placed on each of the radial and ulnar arteries to measure the local blood volume changes of the arteries to estimate the local PTT of each artery for accurate BP measurements. A subject-specific model is generated for each user to characterize the unique vascular properties of the wrist arteries, which vary from person to person.

Furthermore, we present two novel methods for enhancing the measurement of the arterial pulse wave to improve PTT and BP monitoring. For the first method, PTT and BP monitoring require the measurement of multiple pulse signals along the artery through the placement of multiple sensors within a small distance. Conventionally, these Bio-Z sensors are excited by a single shared current source, which results in low directivity and distortion of pulse signal due to the interaction of the different sensors together. For localized pulse sensing, each sensor should focus on a certain point on the artery to provide the most accurate arterial pulse wave, which improves PTT and BP readings. In this method, we propose a multi-source multi-frequency method for multi-sensor Bio-Z measurement that relies on using separate current sources for each sensor with different frequencies to allow the separation of these signals in the frequency domain, which results in isolation in the spatial domain. The effectiveness of the new method was demonstrated by a reduction in the inter-beat-interval (IBI) root mean square error (RMSE) by 19% and an increase of average PTT by 15% compared to the conventional method.

For the second method, local blood pulsatile sensors from wrist-worn devices are affected by the change of sensing location relative to the arteries due to movements of the wearable device which degrade the BP estimation accuracy. This chapter presents a cuffless BP monitoring method based on a novel bio-impedance (Bio-Z) sensor array using a wristband that provides a robust blood pulsatile sensing and blood pressure estimation without calibration methods for the sensing location. The wristband is flexible and has a wearable form factor that includes an array of small built-in electrodes that conforms with the wrist shape to provide high-quality biosensing of the blood activity from multiple locations on the wrist. We use a convolutional neural network (CNN) autoencoder that reconstructs an accurate estimate of the arterial pulse signal independent of sensing location from a group of six Bio-Z sensors within the sensor array. Furthermore, we propose new BP features extracted from the dicrotic notch and the histogram of the arterial pulse signal to improve the accuracy of BP estimation. We rely on an Adaptive Boosting regression model which maps the features of the estimated arterial pulse signal to systolic and diastolic BP readings. Subject-specific BP models are created to capture the individual properties of the arterial blood pulsation. The performance of the BP monitoring system was demonstrated for 6 hours of BP data collected from 4 participants. The data included large BP changes of about 50 mmHg repeated 12 times for each participant at four different sensing locations. BP was accurately estimated at a fixed location with an average correlation coefficient and root-mean-square error (RMSE) of 0.80 and 5.0±0.5 mmHg for diastolic BP and 0.79 and 6.6±0.7 mmHg for systolic BP, respectively. Furthermore, our proposed methods of the sensor array with the CNN autoencoder improved BP estimation at different sensing locations by 34.1% for correlation coefficient and 15.9% for RMSE compared to using a single sensor method. Based on the proposed sensing methods and simulation platform, we continuously monitor physiological phenomena accurately and reliably from wearable devices.

1.4. Innovation

In this section, we summarize the innovation of our research compared to the previous work in the literature. In this work, we present a novel concept of an array of bio-impedance sensors on the wrist with multi-channel sensing at different locations that provides several unique features for continuous monitoring of hemodynamic parameters as follows:

- Measuring the arterial pulse signal from both the radial and ulnar arteries improves the BP estimation accuracy.
- Comparing the pulse signals from the different locations on the wrist allows automatic detection of the location of the artery for optimized sensing of the arterial pulse independent of the placement of the device on the wrist.
- Multi-source multi-frequency bio-impedance method provides localized multi-channel pulse signals that improve the PTT monitoring.
- Calibration-free algorithm combines multiple pulse signals using CNN autoencoder to provide an accurate estimate of the arterial pulse independent of sensing location which provides accurate BP with device movements on the wrist.

In addition, the proposed simulation platform based on a grid of time-varying impedance to model the tissue and the artery in SPICE simulation environment enables the following advantages:

- Fast experimentation of the bio-impedance sensing circuits and electrode configuration for optimizing the sensing methods and algorithms.

- Understanding the effects of the injection frequency, the location of the sensor relative to the artery and the depth of the artery inside the tissue on the sensed pulse signal.
- This method is general and can be applied on any part of the body, for example, the chest to model the heart and lung movements.

2. WEARABLE BIO-IMPEDANCE SENSING METHODS[1]

2.1. Overview

Cuffless blood pressure (BP) monitoring relies on the translation of significant features in the blood pulsatile signals into blood pressure readings through regression models. The quality of the blood pulsatile signals is critical for the estimation of the BP. The pulse signals should have high quality by minimizing the noise in the sensing circuits and signal processing algorithms. The skin-electrode interface is crucial for good contact quality with the skin which is controlled by the sensing electrode and the shape of the wearable device. The skin-electrode impedance is a function of electrode material, size, and shape and affects the sensing circuits. In this chapter, we present the fundamentals of wearable bio-impedance sensing methods for blood pulsatile activity monitoring. The circuits and signal processing algorithms are presented for multi-channel sensing with a high signal-to-noise ratio, with high time resolution and long-term acquisition of continuous pulse data. In addition, we present the design of the wristband that includes a 2D array of electrodes that allows for multiple configurations of Bio-Z array sensing from the wrist. We also illustrate the skin-electrode impedance versus frequency for multiple types of electrodes.

---

[1] Part of this chapter is reprinted with permission from "Cuffless Blood Pressure Monitoring from an Array of Wrist Bio-impedance Sensors using Subject-Specific Regression Models: Proof of Concept," by B. Ibrahim and R. Jafari, 2019. *IEEE transactions on biomedical circuits and systems,* vol. 13, no. 6, pp. 1723-1735, 2019, Copyright 2019 by IEEE.

2.2. Bio-impedance Theory

Electrical conduction happens inside the human body at the cellular level, building up a large impedance network over the whole body. The whole process is governed by the ionic exchange mechanism that is controlled by the cell membranes to generate an imbalance in the charge distribution and trigger the electrical current transfer. Since the cell membrane is physically a lipid bilayer of several nanometers in size, it acts as a capacitive barrier that requires alternating current (AC) to penetrate within the intracellular medium. This capacitive barrier is much apparent on a larger scale to the human skin itself that protects the inner fragile conductive medium from the outside disturbances.

Bio-impedance is a non-invasive electrical method that allows monitoring the properties of the cellular and tissue properties and dynamics of the structural changes upon time [26]. The body, different tissue, different cells, different organs and constructs have different levels of electrical conductivity and permittivity as shown in Table 1 [27]. For

Table 1: The dielectric properties of human tissues at frequency of 10 kHz.

Tissue	**Conductivity (S/m)**	**Permittivity**
Skin	2.04E-4	1.13E+3
Bone	2.0E-2	5.0E+2
Fat (Subcutaneous)	4.3E-2	9.12E+2
Muscles	3.4E-1	2.59E+4
Blood	7.0E-1	5.25E+3

example, muscles are more conductive than fat, and they both are more conductive than skin epidermis. Bio-impedance in a wide range of its meaning is the expression of how well the electrical current is conducted within or impeded by the biological cells. Bio-impedance is measured by applying AC electrical current of low intensity to the tissue through a pair of electrodes connected to the skin.

The tissue, consisting of cellular constructs, includes intracellular fluids (ICF) inside the cell membrane and surrounded by extracellular fluids (ECF) [28]. The current and voltage distribution are generated inside the tissue depending on the electrical properties of the excited regions. The voltage difference across certain regions can be measured by a separate pair of electrodes (Kelvin Sensing) to eliminate the effect of skin impedance and focus only on the tissue impedance. The higher the potential drop, the higher the electrical impedance. The frequency of the AC current signal plays a major role in understanding the bio-impedance measurements and understanding the tissue properties that include resistive and capacitive electrical properties.

As discussed above, the cell membrane act as a capacitor C_M, while ICF and ECF act as resistors R_I and R_E respectively. At lower frequencies (<1kHz), the current typically does not pass through the cell membrane [29]. At such modality, the current fluctuations would only represent the changes in the ECF by following through R_E only. At the higher frequencies (>1kHz) the current passes through the cell membrane, allowing for more precise bioanalysis of the ECF and ICF and the equivalent impedance can be approximated by the parallel equivalent resistance of R_I and R_E ($R_I||R_E$) as shown in Figure 3 (a). The trends of the resistance and reactive parts of bio-impedance versus frequency are plotted in the Cole-Cole plot as illustrated in Figure 3 (b). The resistive part of bio-impedance is maximum and equal to R_E at DC and decreases to $R_I||R_E$ at high frequencies, while the reactive part is zero at DC and high frequencies and is maximum at frequency $fc = 1/(2\,\pi\, C_M(R_E\ +\ R_I))$.

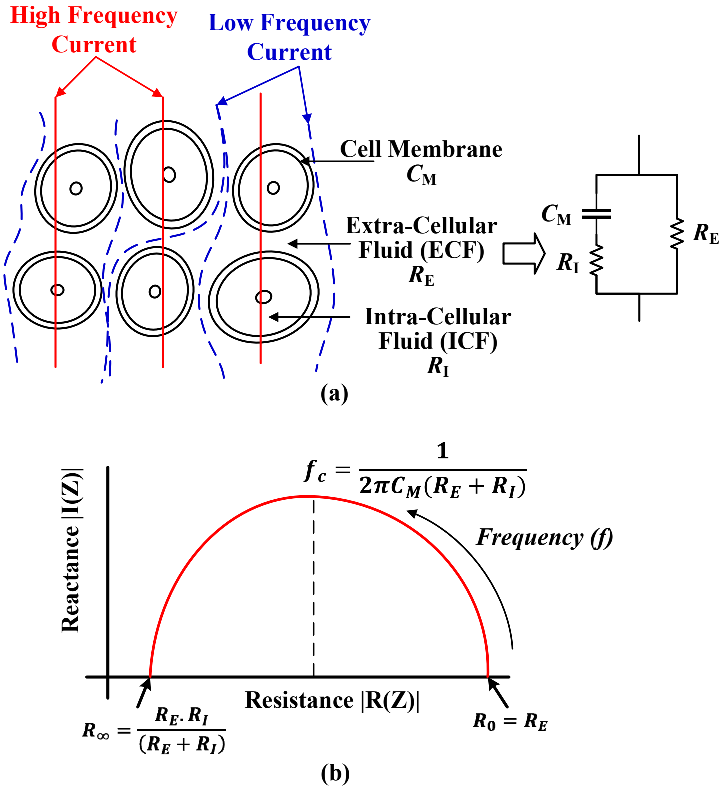

Figure 3. (a) Bio-impedance equivalent circuit, (b) Cole-Cole plot

AC current signal is commonly used for tissue excitation instead of direct current (DC) signals because DC current signal produces polarization at the electrode by the accumulation of charges at the tissue below the electrode which prevents continuous current from flowing. In addition, the stimulation of the tissue and organs decreases by using AC current signal as the frequency increases which reduces the electrical hazards. Another advantage for higher frequency currents is the decrease of the skin-electrode impedance which allows injecting higher current amplitudes in the body to increase the accuracy of measuring the body impedance. However, for safety considerations, there is a current limit determined by safety standards and regulations such as IEC 60601 to ensure a safe connection with the human body and avoid electrical shocks and hazards [30]. This current limit is determined by 100µA for frequencies less than 1 kHz. As the frequency increases, the tissue and nerves become less sensitive to the current signal which all increasing the current limit linearly with frequency up to 10mA at 100 kHz and remains constant for higher frequencies [31].

Due to vague labels and a wide range of technique interpretations, the bio-impedance when applied for certain tasks have been given multiple different names. Such, when used to measure cardiograms of the heart, it is called Impedance Cardiography (ICG). Careful analysis of the ICG signals, their shape and dynamics allow the researchers and clinicians to diagnose heart-related diseases and parameters, such as stroke, cardiac output, etc.

Bio-impedance itself has been investigated for more than six decades in numerous studies within the efforts of understanding human physiology and biology. These efforts partially focused on assessing the body composition leveraging from the differences in the impedance of the current through different types of tissues (i.e. fat, muscle, etc.) and the amount of water within the body. In a common clinician practice, the measurements are routine, and the measurements at different frequencies are subtracted to measure the intracellular impedance, and used to calculate the body fat mass. Such studies, however, are very rudimentary and not suitable for wearable applications. The wearable bio-

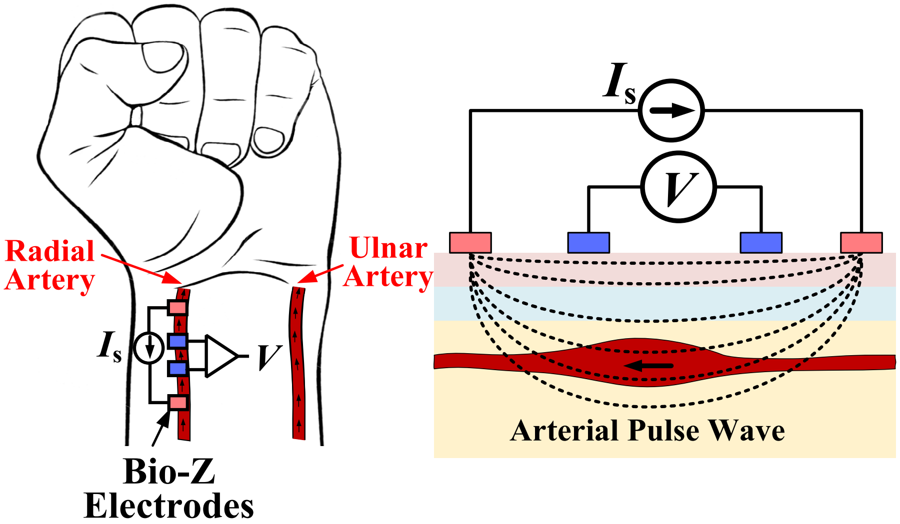

Figure 4. Overview of Bio-Z sensing of arterial pulse wave from the wrist arteries using 4 electrodes of the 4-point Kelvin sensing.

impedance, in the narrower terms, as will be presented in this work is a modular and task-specific sensor technology that can be used for numerous health applications. The applications include monitoring heart rate and its variability, blood pressure, temperature, physical activity, respiration rate, etc. In this research, we focus on wearable bio-impedance sensing for hemodynamic monitoring such as blood pressure monitoring.

2.3. Bio-Z Sensing Concepts

The bio-impedance is measured by applying an AC sinusoidal current through a pair of electrodes and sensing the voltage with two different electrodes near the excitation electrode (Kelvin connection) as shown in Figure 4. The measured voltage is a sinusoidal voltage at the same frequency as the applied current with amplitude and phase modulated by the bio-impedance. Quadrature demodulation is used to obtain the real R(Z) and imaginary I(Z) components of the impedance by multiplying the sensed signal by the in-phase (I) and quadrature (Q) carriers.

There are several challenges for measuring BP based on PTT using bio-impedance signals from the wrist. The wrist Bio-Z signal variations ΔBio-Z due to blood volume changes in the arteries are extracted after removing the Bio-Z DC offset. At every heart beat, the Bio-Z signal descends from the first main peak to the first notch, which indicates a sudden increase in the blood volume due to the arrival of the pressure pulse to the sensing location as shown in Figure 5. The Bio-Z peak point represents the diastolic phase while the notch point represents the systolic phase of the pressure pulse. In addition, the back reflection of the pressure pulse due to higher vascular resistance causes the second smaller peak and notch in the middle of the cardiac cycle.

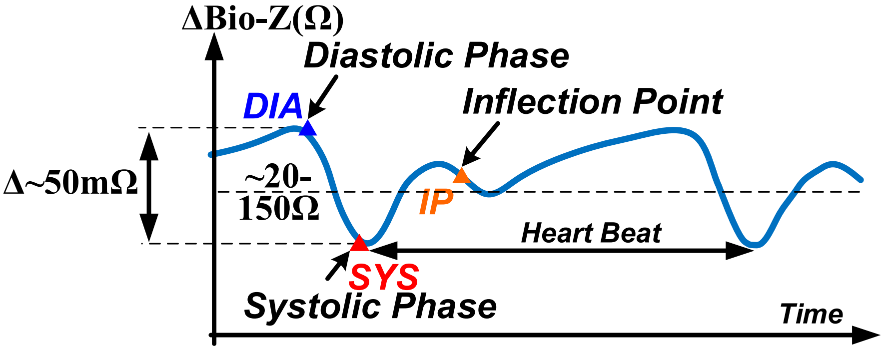

Figure 5. A typical blood pulsatile activity as extracted from Bio-Z signal with the illustration of the systolic and diastolic phases of the pulse and the typical impedance values of the DC component and the peak-to-peak amplitude of the pulse signal.

In order to measure PTT from the wrist arteries, two sensors should be placed along the wrist arteries to measure the delay between the pulse arrival time at the two locations. In order to target a small form factor wrist-worn device, the sensors should be placed within a few centimeters over the wrist arteries with each sensor focuses on a localized region of the artery. At such a small distance between the bio-impedance electrodes, the amplitude of the sensed bio-impedance signal becomes less than 50mΩ in the presence of large DC resistance in the order of 100Ω. In addition. the measured PTT over a small distance is a very small value less than 10ms compared to the cardiac cycle which is around 1 second. Therefore, accurate bio-impedance sensing with low noise and high time resolution is essential in order to detect the very small amplitude variations due to blood flow and measure very small delays over a small distance on the wrist.

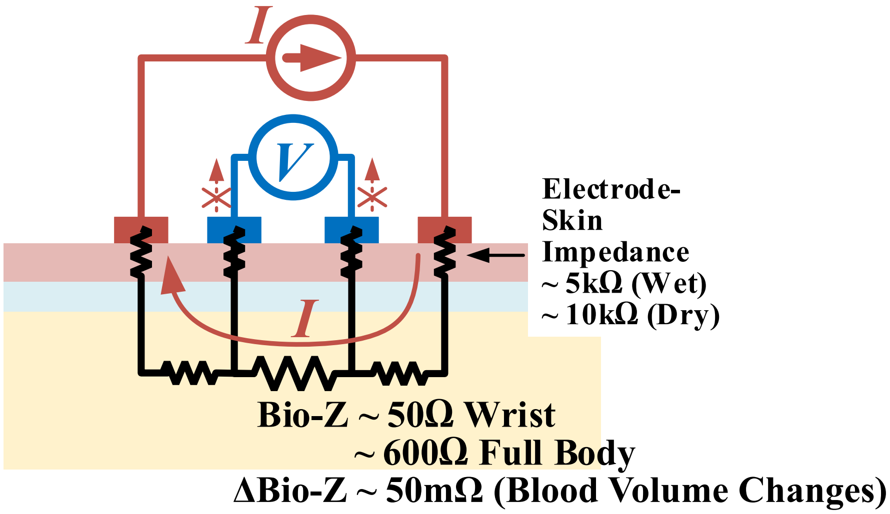

Figure 6. Simple Model for the tissue, skin-electrode impedance and the Bio-Z measurement method

The 4-point Kelvin sensing method is useful to minimize the effect of the large skin-electrode impedance at the interface between the electrode and skin which is in series to the target Bio-Z as illustrated in Figure 6. The skin-electrode impedance is typically 2 orders of magnitude higher than the Bio-Z which is in the order of 5 kΩ for wet electrode and 10 kΩ or higher for the dry electrodes. The separate pair of electrodes for the voltage sensing does not allow current to flow through this pair of electrodes which allows the voltage signal to be independent on the skin-electrode impedance and only measure the target Bio-Z. However, the skin-electrode impedance affects the current source circuit since current flows in the pair of current electrodes. As a result, the maximum current amplitude is limited by the voltage drop on the current electrodes to avoid saturation by the voltage supply of the current source. Therefore, we studied the effect of the skin-electrode impedance on Bio-Z sensing as we present in this chapter in the following sections.

In order to measure blood pulsatile activity for PTT and BP estimation, we implemented a multi-channel bio-impedance measurement hardware on a custom printed circuit board (PCB) in addition to the signal processing algorithms. The system was based on ARM Cortex M4 microcontroller and connect to PC using USB bridge. The system supports data collection for several minutes continuously with high configurability in the sensing parameters such as injection frequency and current amplitude. We developed and tested an array of dry electrodes on a wrist strap, which will be used in our final wearable device. The electrical characterization of the dry electrodes was done by showing the quality of electrode contact with the skin using the skin-electrode impedance.

2.4. Bio-Z Sensing Hardware

The Bio-Z sensing hardware consists of the circuitry to generate and inject alternating current signals to the wrist skin at programmable frequencies and amplitudes, and the analog signal conditioning circuit to sense, amplify, and filter the detected differential voltage on each pair of electrodes.

The high accuracy and low noise sensing of blood pulsation play a critical role in the estimation of BP which relies on precise amplitude and time features extracted from these signals. The main challenge of the sensing hardware and signal processing is the multi-channel detection of small Bio-Z variation (ΔBio-Z) ranges from 50 mΩ to 150 mΩ due to blood volume changes in the presence of large DC Bio-Z of around 50 Ω that represents the static tissue fluids. In addition, the signal measurement methods require high time resolution and continuous data acquisition for several minutes. The low-noise multichannel Bio-Z sensing hardware, the so-called Bio-Z XL, is explicitly designed to capture the slight variations in Bio-Z with high resolution. A custom-developed printed circuit board (PCB) is designed to provide simultaneous low-noise Bio-Z sensing for up to 8 channels for this study.

An ARM Cortex M4 microcontroller as the central processor, instructs and controls the essential functions of the system. The main functions consist of generating the programmable alternating current signal, sampling the sensed and amplified potential difference of voltage sensing electrodes and then, sending the digitized data to a stationary computer connected to the Bio-Z XL board through USB.

The hardware is built around the ARM Cortex M4 MCU, which generates the user-defined digital AC waveform that is converted to a voltage signal by a 16-bit DAC (DAC8811, Texas Instruments, USA) as shown in Figure 7. In its turn, the DAC utilizes a negative feedback loop on a low-noise operational amplifier (OPA211, Texas

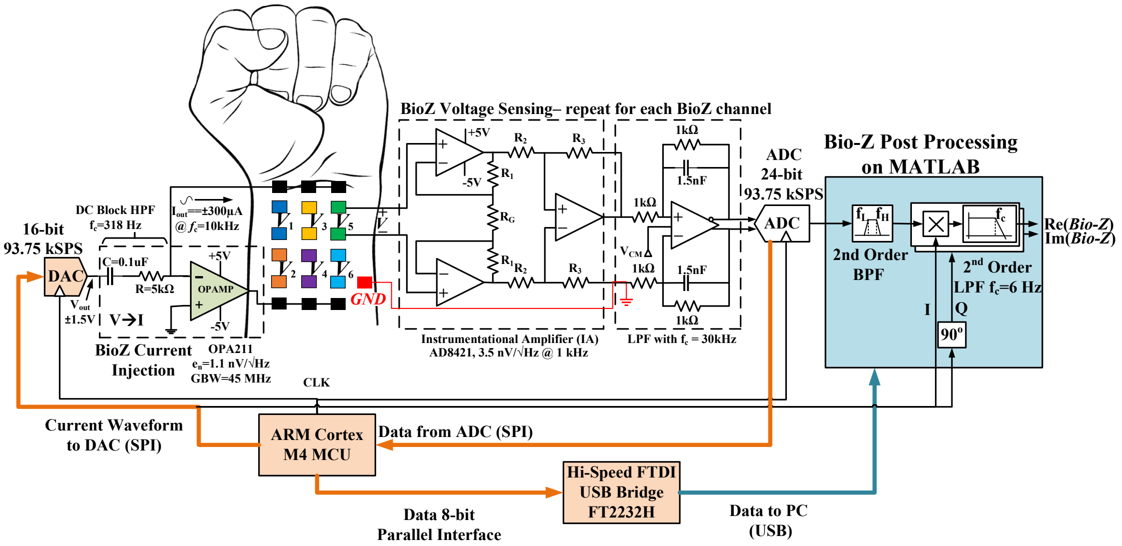

Figure 7. The block diagram of the Bio-Z sensing hardware and signal processing that is implemented in the Bio-Z XL PCB and the post-processing algorithms in MATLAB. The sensing hardware is responsible for the current injection and voltage sensing with parameters consisting of frequency and amplitude of the signal, and the time interval for bio-impedance data acquisition. The PC receives the digitized data and store on local hard drive. The data are then processed in MATLAB and de-mixed bio-impedance signals are extracted. Modified with permission from [1].

Instruments, USA) to generate an AC current signal with programmable amplitude and frequency. A series capacitor at the DAC output is used to block the DC current component's injection into the human body. To extract the Bio-Z signal, we measure the voltage signal induced from the modulation of body impedance to the amplitude and phase of the injected current signal. The voltage sensing path depends on the low noise instrumentation amplifier (IA) AD8421 from Analog Devices with low noise spectral density of 3.5 nV/√Hz at 1 kHz. The IA has a programmable gain set by an external resistor, which is adjusted to provide a gain of 40 dB to measure Bio-Z up to 150 Ω. In addition, the IA has a high common-mode rejection ratio (CMRR) of 126 dB to cancel out the DC offset voltage before ADC sampling in order to ensure full utilization of the ADC's dynamic range. A high-precision ADC samples the IA output through an analog anti-

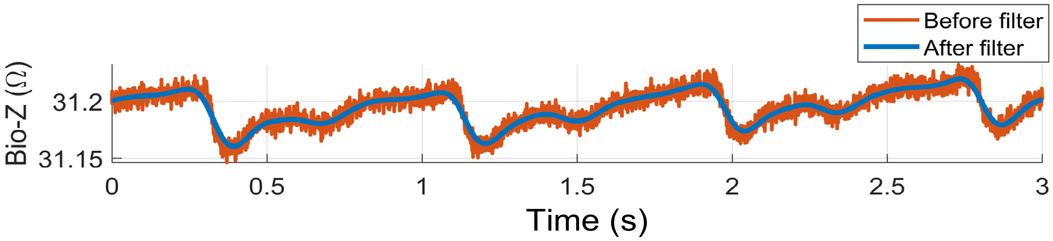

Figure 8. Example of Bio-Z signal before and after low pass filtering. Reprinted with permission from [1].

aliasing low-pass filter with a cut-off frequency of 30 kHz. The ADC (ADS1278, Texas Instruments, USA) samples the voltage at 93.75 kHz sampling frequency with a 24-bit (0.3 µV) resolution to provide enough precision. The analog front end and the MCU can handle to measure simultaneously 8 independent streams and various analog readings. In this research, the first 6 channels are selected for high-resolution Bio-Z sensing and the 7th channel is reserved for simultaneous PPG readings from finger clip to act as a reference for the blood pulse signal and for syncing with the BP reference device (Finapres NOVA BP system) based on matching the inter-beat-interval (IBI). In addition, the 8th channel is dedicated to simultaneous ECG measurements for validation purposes. The sampled data is forwarded to PC via the MCU and Hi-Speed USB Bridge for signal post-processing through MATLAB. The Bio-Z post-processing algorithms start with a bandpass filter centered at the current injection frequency to remove out-of-band noise. Then, the real and imaginary components of Bio-Z are extracted by synchronous demodulation through multiplying the measured signals by the sinewave generated from the MCU and its 90-degree phase shift. The final Bio-Z signals are filtered by a second-order digital IIR low pass filter (LPF) with a cut-off frequency of 6 Hz. The cut-off frequency was selected to

Table 2: Bio-Z Sensing Specifications.

Specification	**Value**
Resistance Range	Up to 150 Ω
Accuracy	1 mΩ
IA Gain	40 dB
IA CMRR	126 dB
Sampling Frequency	Up to 93.75 kSPS
Injection Frequency	1 – 22 kHz
Time Resolution	12.8 μs
Current Amplitude	Up to 1 mA
3-dB Bandwidth	6 Hz
Number of Channels	8

remove the carrier signal after demodulation and the out-of-band noise such as 60 Hz interference while keeping the main frequency components of the pulse signal which are below 6 Hz as shown in Figure 8. The hardware is calibrated by measuring the impedance of a known resistor in order to convert the measured voltage to an accurate resistance value. The measurement system was capable of measuring impedance with RMS error less than 1 mΩ, which is much lower than the target Bio-Z variations. The full specifications of the Bio-Z sensing hardware and signal processing algorithms are shown in Table 2.

An interface between the hardware and the stationary computer is developed in Visual Studio so that the user can directly program the frequency and amplitude parameters of the current injection signal, and the time length of bio-impedance data acquisition. Upon instructing the parameters, the interface receives the digitized bio-impedance data transmitted by the Bio-Z XL and stores them on a local hard drive for signal processing and features extraction. The frequency of the alternating current signal can be programmed in the range of 2-20 kHz. Cell membrane in tissue demonstrates capacitive properties and as a result, its impedance is inversely proportional to the current injection frequency, i.e. more current can flow inside the cells at higher frequencies. Moreover, the impedance of skin-electrode contact reduces at higher frequencies; hence, the current injected to tissue through the pair of electrodes will not suffer from saturation issue. Consequently, in trade-off with the maximum sampling rate of the Bio-Z XL, 10 kHz is chosen as the optimum frequency of the current signal. According to IEC 60601-1 standard for medical electrical equipment, in order to comply with the safety regulations, the amplitude of the current signal is designed to be limited to 0.3 mA [26]. In addition, using the current injection signal for Bio-Z at 10 kHz compared to the low-frequency flicker noise provides higher immunity to noise and 60 Hz interference compared to other baseband physiological signals such as ECG and EEG.

As the reference for BP data estimation, we employed BP monitoring by Finapres NOVA system. In fact, we collected the bio-impedance data through the wristband simultaneously with Finapres. The system continuously measures BP using a finger pressure cuff place on the middle finger that is calibrated by the brachial cuff. However, the data collected by our system and the BP measurements acquired by Finapres need to be synchronized. Therefore, since the Finapres system is equipped with continuous PPG monitoring and collects the PPG data using a finger clip along with BP, we added a PPG sensor to our Bio-Z XL device, as well. Based on a comparison between the unique pattern of inter-beat intervals of the two PPG signals, we can synchronize the BP estimated by our AdaBoost regression model and the BP measured by the Finapres system.

2.5. Bio-Z Noise Analysis

The quality of Bio-Z pulse signal (ΔBio-Z) plays an important role in the next stages of characteristic points detection and feature extraction for accurate blood pressure estimation. The electronic noise from the hardware was studied carefully to ensure that the noise is not significant compared to the pulse signal and to guarantee enough signal-to-noise ratio for accurate signal monitoring. The Bio-Z signal is not affected by flicker and low-frequency noises because the voltage signal of the Bio-Z sensor is the amplitude modulation of the high-frequency current signal at 10 kHz with a small bandwidth of few hertz for the pulse signal. The voltage signal is first filtered by a bandpass filter (BPF) centered around the current injection frequency of 10 kHz to remove the DC offset and flicker noise. Then, the signal is demodulated by synchronous demodulation to move the Bio-Z signal to the baseband frequency without any effect of the flicker noise.

Figure 9 shows the power spectrum of the sensed voltage signal at the IA output and ADC input. The plot shows the Bio-Z signal located at the current injection frequency of 10 kHz, while the flicker noise and 60 Hz are far away at the low-frequency band. After demodulation, a low pass filter with cut-off frequency of 6 Hz is applied in order to extract the heart pulse signal. Therefore, the Bio-Z signal has higher immunity to flicker noise and 60 Hz interference compared to other baseband physiological signals such as ECG and EEG that lack this current injection and demodulation effect.

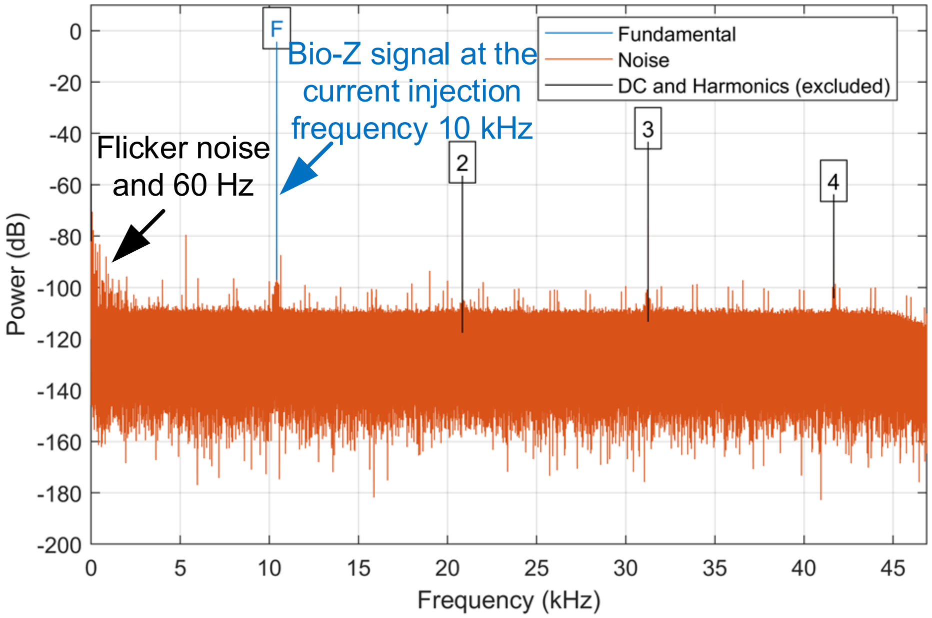

Figure 9. Power spectrum of the Bio-Z signal at the ADC input that shows the fundamental frequency at 10 kHz in addition to 3 harmonics. The flicker and low-frequency noise have no effect on the Bio-Z signal.

The noise around the current injection frequency (10 kHz) is more effective for the signal quality. The noise of the IA at 10 kHz is the most critical in the whole signal path because the voltage signal amplitude is the smallest at the input of the IA which is the interface with the body. The signal amplitude at IA input is 25 mV for the sensing distance of few centimeters at the wrist and with current amplitude of 300µA. The selected IA has low noise of 3.5 nV/√Hz which is negligible for a bandwidth of 6 Hz compared to the pulse signal (ΔBio-Z) amplitude of 25 µV. The ADC noise is also important, but in our design, it is negligible because the selected ADC has 24-bits with very low quantization noise. In order to achieve minimum hardware complexity and power consumption, we measured the maximum allowed noise for ADC and IA that can be allowed for the ADC and IA without significant degradation in the quality of the pulse signal. The measured

Bio-Z signal with our low-noise system is considered as the reference Bio-Z signal. The ADC noise effect is evaluated by quantizing the reference Bio-Z signal mathematically by the number of bits (N) that varies from 5 to 22. The RMSE of Bio-Z signal is calculated for every N over a segment of 120 seconds and plotted versus N as shown in Figure 10. The figure shows the Bio-Z RMSE increases as N decreases because the quantization noise increases as expected. For N is lower than 12, the RMSE increases at larger steps compared to N higher than 12 which shows the significant distortion in the Bio-Z pulse signal for N lower than 12. Figure 11 shows the significant degradation for the ΔBio-Z at N=10 bits and N=11 bits while for N=12 bits and higher, the pulse signal is the same as the reference signal at N=24 bits. These results show that the maximum acceptable root mean square error (RMSE) in the Bio-Z signal can be determined as 1/50 of the typical

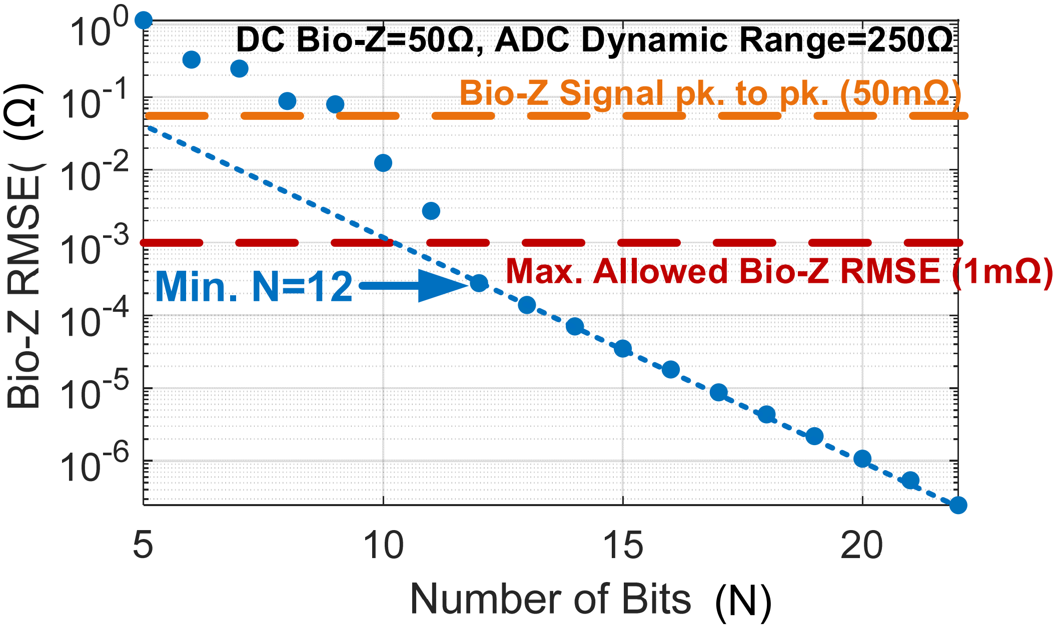

Figure 10. Bio-Z RMSE versus the number of bits (N) with highliting the maximum allowed RMSE of 1mΩ for pulse amplitude of 50mΩ which can be achieved with minimum N=12.

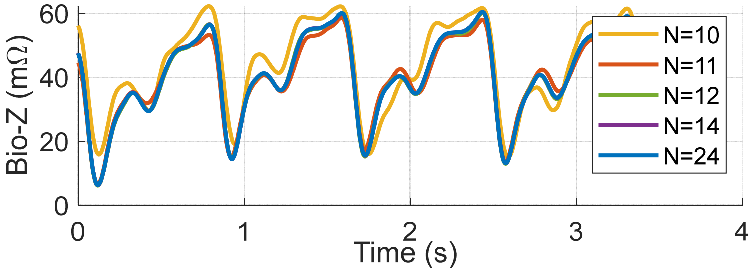

Figure 11. Bio-Z pulse signal verus time for N=10,11,12,14 and 24 to show the significant degradation in the pulse signal for N=10 and N=11 while N=12 and higher has nosiginifcant effect on Bio-Z pulse signal.

peak-to-peak amplitude which is 1 mΩ for pulse signal of 50 mΩ peak-to-peak amplitude that allows for reliable characteristic points detection algorithms. The maximum allowed RMSE of 1 mΩ is highlighted in the figure compared to Bio-Z signal of 50 mΩ amplitude while the ADC dynamic range is 250 Ω to capture DC Bio-Z of 50Ω with enough margin. We can conclude from these results that the minimum N for ADC should be 12 for RMSE of 0.28mΩ which is below the threshold of 1 mΩ.

For the same level of signal quality with Bio-Z error of 0.28mΩ, the analog front-end including the IA can contribute noise equivalent to N=12 which is 350μV RMSE as estimated from the ADC quantization of the ADC raw signal with ADC dynamic range of 5V. The noise of the analog front-end was analyzed by simulations and calculations to understand the contribution of each block and estimate the margin from the maximum noise based on the parameters in Table 3.

Table 4 shows the total noise spectral density of 100.5 nV/√Hz from the analog-front end at its output and the input of ADC. As expected the main noise contributor is the IA OpAmp with 83.8 nV/√Hz because its noise is amplified by the large IA gain G_{IA} of 50.5. The total analog front-end RMSE noise is calculated from $e_{ntot}\,\sqrt{BW * 1.57}$ which is 41μV for the BW of the anti-alias filter of around 100 kHz.

Therefore, there is room for relaxation in the analog-front end noise specification by a factor of 8.5 which is the ratio between the current noise 41µV and maximum noise of 350µV that is equivalent to ADC with 12 bits.

Table 3: Parameters used for noise simulations and calculations.

Parameter	Description	Value
$e_{ni_{IA}}$	IA input noise spectral density	3.5nV/√Hz
$e_{no_{IA}}$	IA output noise spectral density	60nV/√Hz
R_G	IA gain resistor	200Ω
R_{Bio-Z}	Tissue Bio-Z	100Ω
G_{Bio-Z}	Gain of Bio-Z	R_{Bio-Z}/R_{Skin}=100Ω /10e3Ω =0.01
G_{IA}	Gain of IA	1+9.9kΩ/R_G=50.5
G_{Filt}	Gain anti-alias filter	0.5
k	Boltzmann constant	1.380649×10–23 J·K^{-1}
T	Temperature	298 K

Table 4: Noise Spectral Density from SPICE Simulations.

Noise	Description	Noise (nV/√Hz)	Noise equations
e_{nV-I}	Noise of V-I	9	$e_{nV-I} = \sqrt{(e_{ni_{V-I}}.G_{Bio-Z}.G_{IA}.G_{Filt})^2 + (e_{no_{V-I}})^2}$
e_{nBio-Z}	Noise of Tissue Bio-Z	30	$e_{nBio-Z} = \sqrt{4\,k\,T\,R_{Bio-Z}}.G_{IA}.G_{Filt}$
e_{nR_G}	Noise of IA gain resistor R_G	45	$e_{nR_G} = \sqrt{4\,k\,T\,R_G}.G_{IA}.G_{Filt}$
e_{nIA}	Noise of IA OpAmp AD8421	83.8	$e_{nIA} = \sqrt{(e_{ni_{IA}}.G_{IA}.G_{Filt})^2 + (e_{no_{IA}})^2}$
e_{nFilt}	Noise of anti-alias filter	7.7	$e_{nFilt} = \sqrt{(e_{ni_{Filt}}.G_{Filt})^2 + (e_{no_{Filt}})^2}$
e_{ntot}	Total noise	100.5	$e_{ntot} = \sqrt{e_{nV-I}{}^2 + e_{nR_G}{}^2 + e_{nIA}{}^2 + e_{nBio-Z}{}^2 + e_{nFilt}{}^2}$

The estimated maximum allowed noise without degradation in Bio-Z pulse signal quality can allow using ADC with 12 bits and analog front-end with RMSE noise up to 350μV which helps in efficient implementation of IA and ADC in integrated circuits for low cost and small-size implementation of large Bio-Z array.

2.6. Bio-impedance Signal Pre-Processing

The Bio-Z signal processing is responsible for extracting the Bio-Z blood pulsation signal, defined as (ΔBio-Z), from the raw Bio-Z signal. The raw Bio-Z signal includes the ΔBio-Z pulse signal superimposed over a slowly-varying Bio-Z DC component that corresponds to the static tissue impedance. The most prominent feature in the raw Bio-Z signal is the sharp edge between the systolic and diastolic points repeated each heartbeat with the max. slope point in the middle of the edge. The DC component of Bio-Z is estimated from the interpolation between max. slope points detected beat-by-beat. The max. slope points are detected from the lower peaks of the first derivative of Bio-Z constrained by a minimum peak distance of $0.57\times(1/HR)$ and a minimum peak height of 35% of the lower peak envelope. The *HR* is the average heart rate of the processed time segment of 2.5 minutes calculated from the frequency of the most prominent peak of the signal power spectral density. The lower peak envelope of the raw Bio-Z signal is determined using spline interpolation over local maxima separated by at least 0.65 seconds. Then, the ΔBio-Z pulse signal is extracted by subtracting the estimated DC component of Bio-Z from the raw Bio-Z signal.

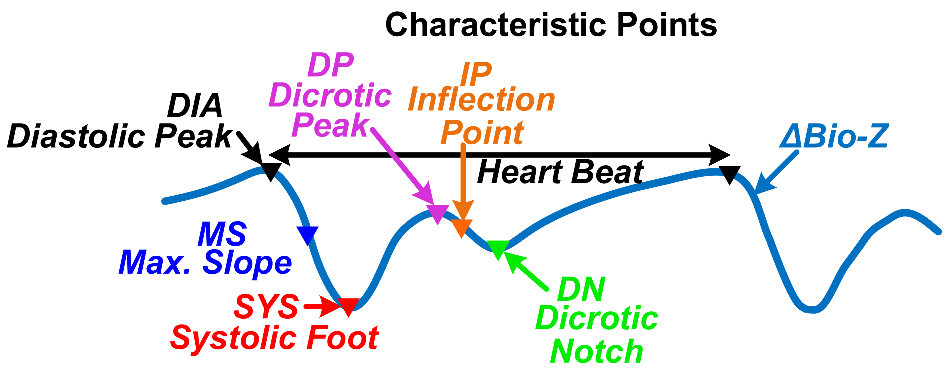

Figure 12. ΔBio-Z signal over one heart beat with illustration of its six characteristic points. The points are diastolic peak (DIA), maximum slope (MS), systolic foot (SYS), inflection point (IP), dicrotic peak (DP) and dicrotic notch (DN).

2.7. Characteristic Points Detection

The dynamic cardiac activity of ΔBio-Z pulse signal is characterized by six characteristic points each heartbeat, consist of diastolic peak (DIA), maximum slope (MS), systolic foot (SYS), inflection point (IP), dicrotic peak (DP) and dicrotic notch (DN) [27]. The selected points can completely abstract the blood pulse morphology and describe the main rising and falling edges of the heartbeat as shown in Figure 12. On every heartbeat, the ΔBio-Z signal descends from the first peak to the first foot, which indicates a sudden increase in the blood volume as the pressure pulse arrives at the sensing point on the wrist. The ΔBio-Z peak DIA and foot SYS points represent the diastolic and systolic phases of the BP pulse, respectively. Furthermore, due to higher vascular resistance, the back reflection of the BP pulse results in the second smaller dicrotic peak and notch in the middle of the heartbeat.

The MS point of ΔBio-Z corresponds to a foot point in the first derivative of the ΔBio-Z signal and a zero crossing in the second derivative of the ΔBio-Z signal. The DIA and SYS points are calculated from the first derivative of ΔBio-Z signal by the two zero-crossing points adjacent to the foot point. The IP point acts as the MS point at the second smaller falling edge in the same heartbeat. The IP point is calculated from the zero crossings in the second derivative of ΔBio-Z signal that follows the MS zero crossing in time in the same heartbeat. Also, the IP point corresponds to a secondary foot point in the first derivative that follows the main foot of the MS point. Similar to the DIA and SYS points, the DP and DN points are calculated from the two zero-crossing points adjacent to the IP second at the foot point of the first derivative of ΔBio-Z signal. The coordinates of the six characteristic points in terms of time and amplitude are the parameters employed to determine BP features. An example of the detection of the characteristic points of the ΔBio-Z based on the first and second derivatives is shown in Figure 13. The plot shows the point detection algorithm can accurately detect all the chrematistic points for six heart beats in the presence of variations in the pulse morphology from beat to beat.

2.8. Electrode Array Wristband

To robustly capture physiological signals, the sensors should be placed close to the skin or directly on the skin at specific locations. In many cases, they should have direct contact with the skin through the electrodes in order to sense voltage or apply current to the body. Robust sensing is affected primarily by the very specific on-body placement of the electrodes, their contact characteristics with the skin and the motion artifacts. Therefore, we propose a 2-D array of high-density miniature electrodes placed on a

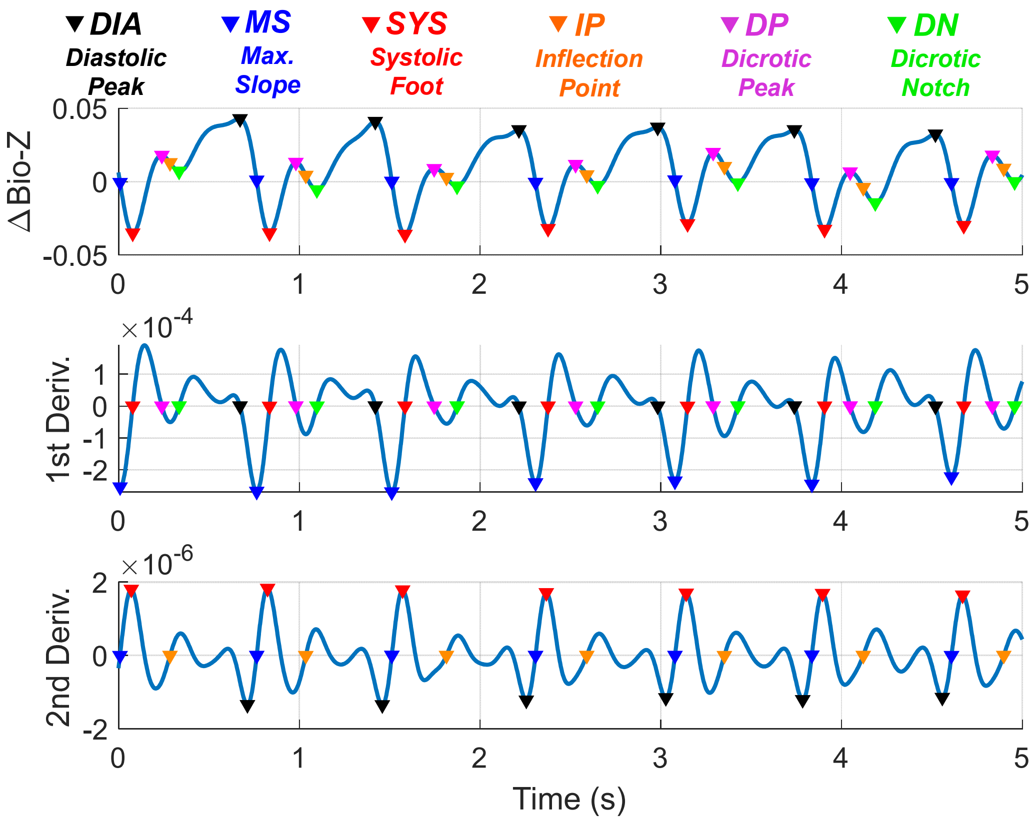

Figure 13. An example of the detection of the characteristic points of the ΔBio-Z based on the first and second derivatives from a measured Bio-Z signal. The plot shows the point detection algorithm can accurately detect all the chrematistic points for six heart beats in the presence of variations in the pulse morphology from beat to beat. Modified with permission from [1].

wristband to improve the electrode-skin contact and the robustness of wearable physiological sensing from the wrist.

Wrist-worn devices are the most common wearable medical devices because they are comfortable, can be worn as a watch, and allow integration of several physiological sensors. Several physiological signals can be measured from the wrist such as electrocardiography (ECG) [32], which can be used for heart rate detection, electro-dermal activity (EDA) for stress detection [33] and bio-impedance (Bio-Z) signals which can be used in plethysmography and pulse wave velocity estimation. In addition, electrical impedance tomography (EIT) can be applied on the wrist using a number of bio-impedance sensors that surround the wrist to reconstruct an image of the wrist, which can be used for applications such as gesture recognition [34].

There are several challenges in using wrist-worn devices for robust physiological sensing. One of these challenges is the proper placement of the electrodes each time the wrist device is worn [35]. For example, the features of the plethysmograph, which is a measure of the blood volume changes, become sharper as the sensor is placed very close to a major artery. There are significant physiological differences between different people, and in addition, there is no guarantee that the user will wear the device each time in exactly the same position; therefore placing a sensor at the optimal location becomes a challenge. The sensors can be placed correctly only by experts using advanced medical equipment, which presents a challenge when the device is expected to be operated outside clinics and by non-expert consumers. Motion artifacts are another challenge for wearable medical devices, referring to signal corruption that occurs when the subject moves during data acquisition [36]. One of the main reasons for the signal distortion is the temporary loss of contact between the electrode and the skin during the movement. Therefore, the ability to assure proper placement of the electrodes covering certain sensing sites and retaining good contact between the electrodes and the skin though incorporating redundancy and leveraging an array of electrodes appear to provide a suitable solution to the aforementioned challenges.

In this work, we propose a wristband with an array of high-density and miniature electrodes to obtain physiological signals across the 2-D area underneath the array with the ability to provide a local measurement across few millimeters at each electrode site on the wrist. This design enables capturing physiological signals with high spatial resolution both improving the robustness of sensing and enabling new sensing paradigms such as the ability to measure pulse transit time and pulse wave velocity using two pairs of electrodes for blood pressure monitoring [32, 37]. Our proposed design provides the ability to automatically select the right sensing location regardless of variations in the placement of the strap on the wrist. In addition, the 2-D array of sensors offers opportunities for spatial monitoring of physiological signals that has many applications [38]. In this chapter, we present a wristband that includes a 2-D array of 48 electrodes. Each electrode has dimensions of 5×5 mm with a spacing of 3.2 mm between each of them, covering an area of 6.25×4.60 cm on the bottom face of the wrist with good skin contact. The array of electrodes provides high (re)configurability by allowing current injection or voltage sensing between any two points on this array. Regardless of how the user wears this device on the underside of the wrist, there will be an electrode that is placed very close to the target location, which can be detected by a searching technique that involves sweeping the electrodes and comparing the signals together to select the best-sensed signal. This search method can be done regularly to update the chosen electrodes if there is a change in the placement of the device on the wrist during operation. This array also helps reduce the effect of motion artifacts because quite likely, not all the electrodes would lose contact with the skin at the same time in presence of movements. If corrupted signals are detected from one electrode, the signal from the next nearest or another electrode, which likely has a stable contact, can be used. In addition, this array of electrodes has wide applications, such that it can measure any bio-potential or bio-impedance signal from the wrist such as ECG, Bio-Z, EDA, etc.

In the following subsections, we describe the design and implementation of the wristband, including the array of electrodes, and the measurement system used for the electrode-skin impedance monitoring. We also characterize the electrode-skin impedance with respect to frequency and compare it to other types of dry and wet electrodes.

2.8.1. Wristband Design

We designed a wristband to ensure that the array of electrodes maintain good contact with the skin, offer minimized discomfort, and conform to all other technical requirements such as electrode size.

The size of the electrodes is an important parameter in the design of the array. The small size increases the number of electrodes within a specific area and enhances the spatial resolution of the measurements. However, electrode-skin impedance increases as the size of the electrode decrease because of the smaller contact area with the skin, which increases the impact of motion artifacts in presence of wrist movement. The size of the electrode was chosen to be 5 mm as a trade-off between the spatial resolution and the skin contact area. The electrode size required was not readily available off-the-shelf, and therefore, it was fabricated in our laboratory.

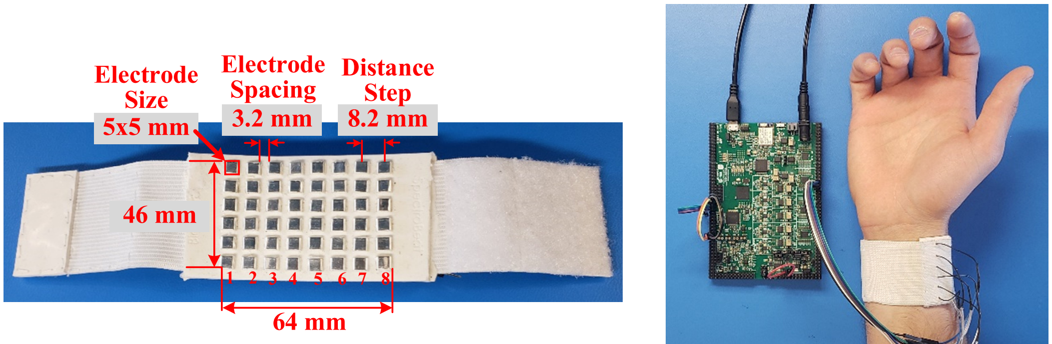

(a) (b)

Figure 14. (a) The implemented wrist-worn sensor array consisting of 6×8 silver electrodes. The size of each electrode is 5 mm × 5 mm and the spacing between each two adjacent electrodes is 3.2 mm, (b) Integration of the wristband to the Bio-Z sensing hardware through our designed Bio-Z XL PCB for detecting the bio-impedance signals.

The wrist-worn sensor array consists of 48 dry silver electrodes, each with an area of 5×5 mm and center-to-center spacing of 8.2 mm between each two adjacent sensing points as shown in Figure 14. Silver has an outstanding electrical conductivity of 62.1×10^{6} Siemens/m and a very low electrical resistivity of 15.9×10^{-9} Ω.m, which makes it an ideal choice for sensing bio-impedance signals. In addition, the 6×8 array of electrodes are embedded in a flexible wristband, appropriate for conforming with the wrist shape. The flexible wristband is made from Ecoflex rubber which is a durable and flexible silicone that conforms with the shape of the wrist to provide good contact with the skin for all silver electrodes. The height of the electrodes and the spacing between them are precisely controlled by placing the electrodes in a mold designed for the wristband with a fixed location and depth for the electrodes with wire connections that are covered by the Ecoflex silicone.

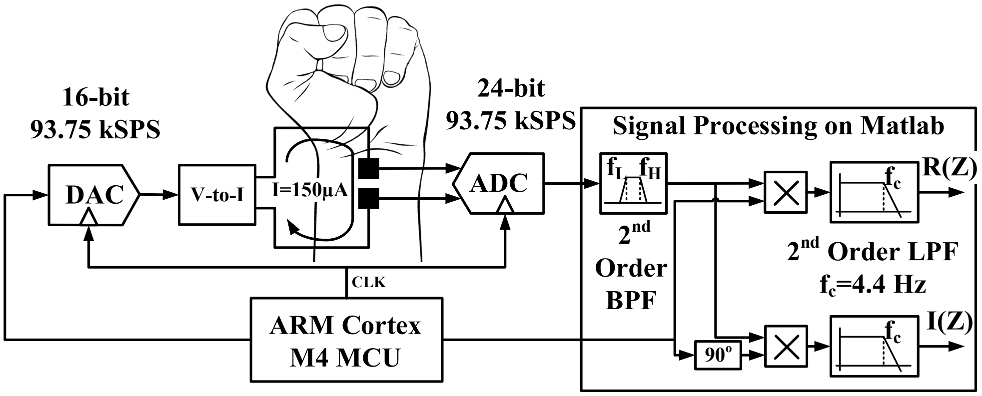

Figure 15. The block diagram of the electrode-skin contact impedance measurement system.

2.8.2. Electrode-Skin Impedance Measurement System

The performance of the electrodes was characterized by the electrode-skin impedance, which was determined by applying AC current between an electrode pair placed on the wrist and measuring the voltage between them. The measured impedance is the result of electrode-skin impedance, which neglects the wrist tissue impedance since it is very small compared to the typical electrode-skin impedance [37].

In order to test the performance of the electrodes across a range of frequencies, we used our programmable hardware which capable of accurate continuous-time monitoring of the real and imaginary components of the electrode-skin impedance at various frequencies for several seconds was used. Current with an amplitude of 150 uA was applied by a programmable current source built from a 16-bit digital to analog converter (DAC) followed by voltage to current converter as shown in Figure 15. The voltage was measured by the ADC with a range of +/- 2.5V.

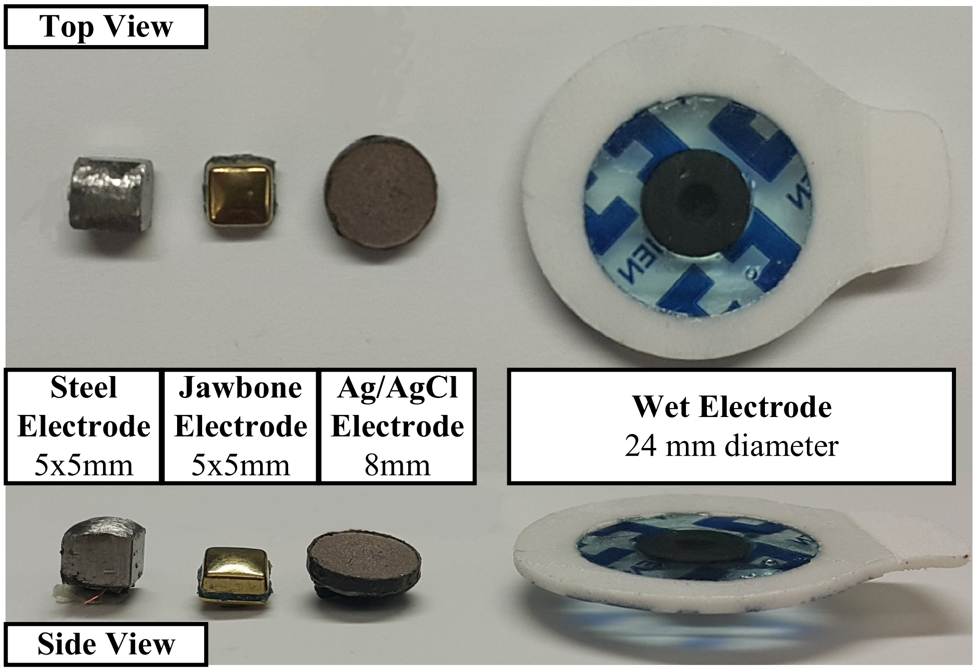

Figure 16. The top and side views of our electrode compared to the other types of electrodes.

2.8.3. Electrode-Skin Impedance Characterization

In the first set of experiments, we compared the electrode-skin impedance of stainless-steel electrode array against two types of commercial dry electrodes and the conventional wet electrode, which are shown in Figure 16. The first type of dry electrode was from a UP3 Jawbone® wearable device, which is a commercial wrist-worn heart rate tracker that uses wrist bio-impedance monitoring. The shape and size of this electrode are similar to the stainless-steel electrode and both are comfortable for the user. However, the Jawbone® electrode should have lower impedance because it is externally coated with a

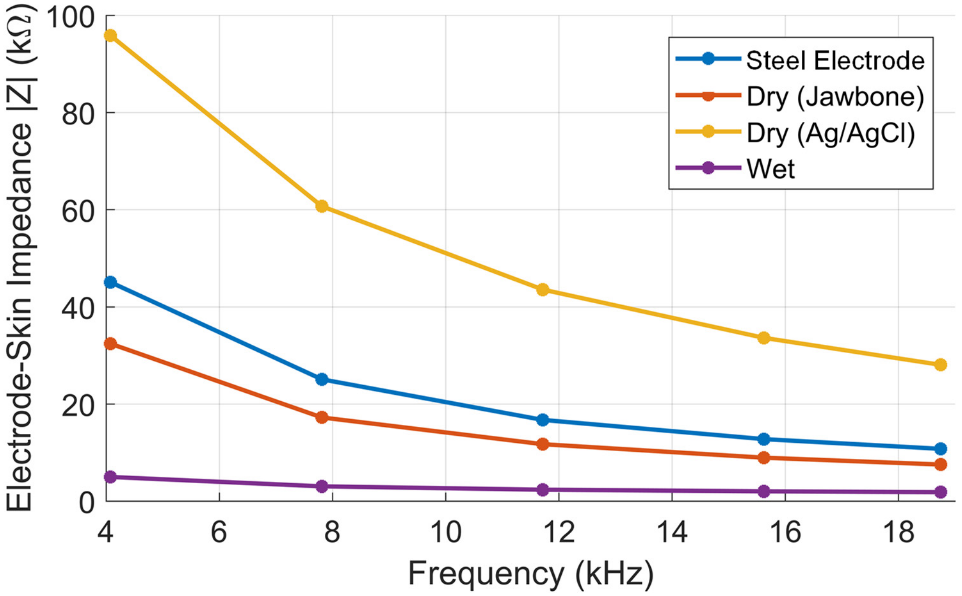

Figure 17. The electrode-skin impedance versus frequency for the four types of electrode used in the experiment.

highly conductive material to reduce the electrode-skin impedance. The second type of commercial dry electrode was an 8 mm diameter disc of sintered Ag/AgCl, which is a good conductive material. The wet electrode used was a Covidien Ag/AgCI pre-gelled adhesive electrode with 24 mm diameter. The Ag/AgCI and adhesive gel with its large area provides the best conductivity among all types of electrodes, but it is not suitable for continuous wear because it prevents skin from breathing. The electrode-skin impedance was measured between the four electrode pair types by injecting a current of 150 uA in the range of 4 kHz to 20 kHz, in steps of 4 kHz. Each pair was placed at approximately a distance of 4.5 cm at the same location on the human subject’s wrist. The electrode-skin impedance versus frequency for the four types of electrodes can be seen in Figure 17.

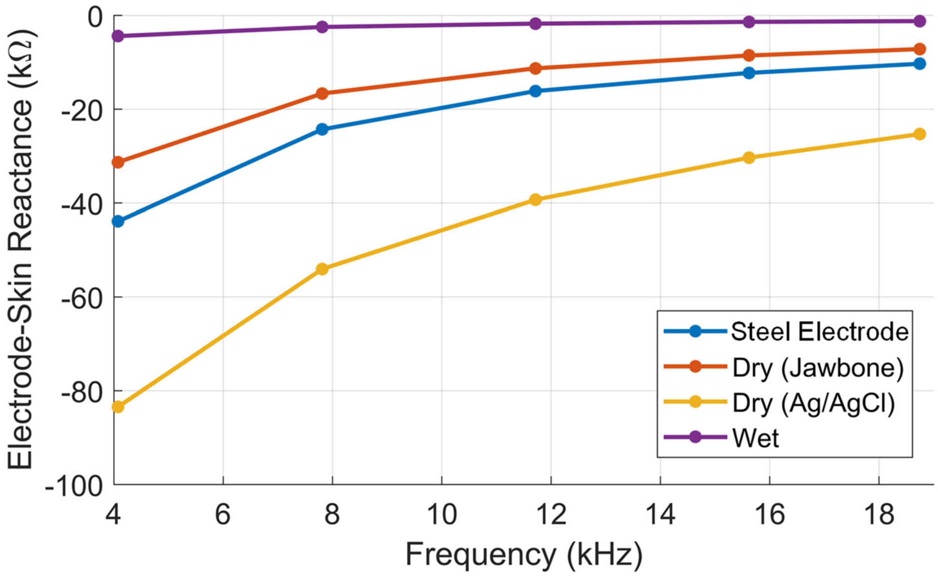

Figure 18. The electrode-skin reactance versus frequency for the four types of electrode used in the experiment.

As the frequency increases, the impedance decreases, likely due to the reactance. Reactance is believed to be caused by the skin's response to an alternating current due to its capacitive nature. Skin is usually modeled as an equivalent circuit containing a capacitor and resistor in parallel [39]. The graph shows that the steel electrode has about a 40kΩ greater impedance at low frequency and a 10 kΩ greater impedance at a higher frequency than the wet electrode pair, which was expected. It was also noted that the Jawbone electrode has a slightly lower impedance than the steel electrode because of its external coating. However, the dry Ag/AgCl electrode has the highest impedance among all types despite of its high conductivity. This can be explained by the concave shape of the surface of this dry Ag/AgCl electrode which decreased the skin contact area. This indicates the importance of the protrusion of the electrode surface to decrease the electrode-skin impedance as implemented in our electrode. Figure 18 displays the electrode-skin reactance, which correlates directly with Figure 17.

2.9. Conclusions

In this chapter, we presented the design of our custom Bio-Z sensing board (Bio-Z XL) including the circuits and the signal processing algorithms that provide multi-channel measurements of Bio-Z pulse signals with a resolution of 1 mΩ. The sensing hardware can provide current amplitude up to 1 mA and frequency up to 22 kHz. The Bio-Z signal pre-processing is shown including filtering, demodulation, DC removal, and the characteristic points detection algorithms. The design of a custom electrode array wristband is presented that includes 6×8 small size silver electrodes that provide flexible Bio-Z sensing configuration by connecting to the XL board.

3. PULSE WAVE MODELING USING BIO-IMPEDANCE SIMULATION PLATFORM BASED ON A 3D TIME-VARYING CIRCUIT MODEL[2]

3.1. Overview

Bio-Impedance (Bio-Z) is an effective non-invasive sensor for arterial pulse wave monitoring based on blood volume changes in the artery due to the deep penetration of its current signal inside the tissue. However, the measured data are significantly affected by the placement of electrodes relative to the artery and the electrode configuration. In this work, we created a Bio-Z simulation platform that models the tissue, arterial pulse wave, and Bio-Z sensing configuration using a 3D circuit model based on a time-varying impedance grid. A new method is proposed to accurately simulate the different tissue types such as blood, fat, muscles, and bones in a 3D circuit model in addition to the pulsatile activity of the arteries through a variable impedance model. This circuit model is simulated in SPICE and can be used to guide design decisions (*i.e.* electrode placement relative to the artery and electrode configuration) to optimize the monitoring of pulse wave prior to experimentation. We present extensive simulations of the arterial pulse waveform for different sensor locations, electrode sizes, current injection frequencies, and artery depths. The simulations are validated by experimental Bio-Z measurements. This model will enable researchers and designers to create time-varying blood flow models and rapidly

---

[2] Part of this chapter is reprinted with permission from "Pulse Wave Modeling Using Bio-Impedance Simulation Platform Based on a 3D Time-Varying Circuit Model," by B. Ibrahim, D. A. Hall and R. Jafari, 2021. *IEEE Transactions on Biomedical Circuits and Systems*, vol. 15, no. 1, pp. 143-158, Feb. 2021, Copyright 2021 by IEEE.

test the effectiveness of the sensing methods and algorithms without the need for extensive experimentation.

3.2. Introduction

Continuous hemodynamic monitoring can improve the diagnosis and management of cardiovascular diseases (CVD). Arterial pulse wave has been used extensively for continuous measurement of hemodynamic parameters through monitoring the pulsation of blood inside the arteries [38, 40]. Pulse transit time (PTT), which is the time delay of the pulse wave traveling between two points along an artery, can be used for BP estimation through a cuffless method with non-invasive and comfortable sensors [7, 32].

Bio-Impedance (Bio-Z) can measure effectively pulse wave in the arteries through the deep penetration of electrical signals in the tissue. When the Bio-Z sensor is placed close to the artery, it can measure arterial pulse wave from the blood volume changes. PTT can be measured by a small form-factor Bio-Z sensor from the delay between two voltage signals measured from two pairs of electrodes over a short distance along the artery, as shown in Figure 19Figure 19(a) [24, 41]. In addition, Bio-Z signals were validated to estimate BP from wrist-worn sensors based on PTT and other features extracted from the morphology of the arterial pulse wave measured from the wrist arteries [1, 6]. One of the main challenges of arterial pulse sensing using Bio-Z is the lack of efficient simulation tools that help one to understand the electrical response of the tissue and blood flow for the applied current signal stimulus versus the different sensing parameters, such as the sensing location relative to the artery, electrode configuration, current injection frequency, and artery's depth.

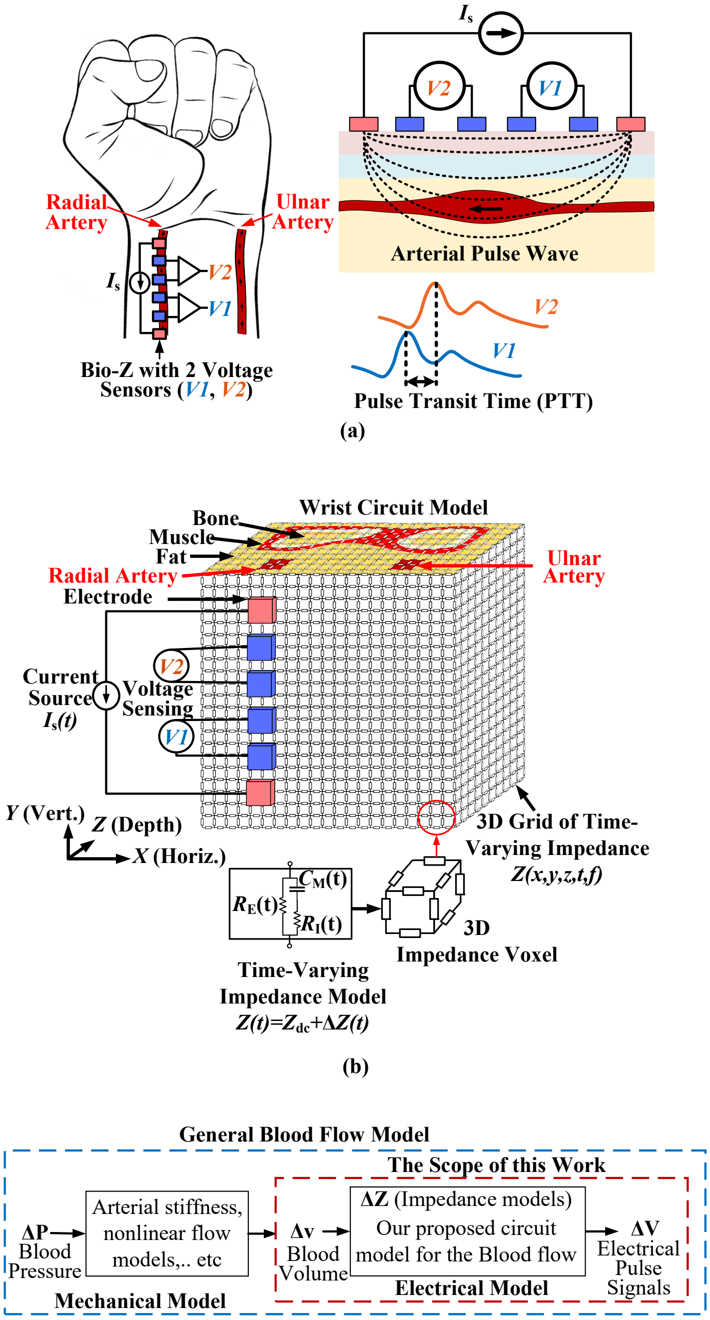

(c)

Figure 19. (a) Bio-Z sensing for PTT from the wrist, (b) Overview of the proposed wrist circuit model for Bio-Z simulation platform based on a 3D time-varying impedance grid that models arterial pulse wave and PTT, (c) the scope of this work focuses on the proposed electrical model of blood flow which can be augmented by any mechanical model to provide complex blood flow model. Reprinted with permission from [3].

In this chapter, we propose a 3D circuit model for the tissue and blood pulsation based on a time-varying 3D impedance grid to model dynamic activities inside the body such as arterial pulse wave, as shown in Figure 19(b). The tissue is modeled using a 3D grid of small, interconnected, time-varying impedance elements (voxels). Each voxel consists of the equivalent circuit of cells that represent different tissue types. The blood flow inside arteries is modeled by a time-varying voxel impedance that represents the artery to simulate blood volume changes and pulse wave propagation. A parameterized SPICE model is used to describe the geometry and conductivity of the modeled tissue, diameter, depth, and location of the arteries, and the location and spacing of the electrodes on the skin. The 3D aspect of the proposed model provides more accurate modeling of the tissue and the sensing signals compared to 2D models. The injected current signal flows in 3D space inside the tissue, therefore the 3D model provides an accurate distribution of current and potential in space compared to 2D models that neglect fringe currents that flow in the third dimension. In addition, the proposed 3D model provides complex sensing configurations for the pulse wave that are not possible with 2D models such as modeling the effect of moving the Bio-Z electrodes orthogonal to the artery's direction on the sensed pulse signal.

The general blood flow model can be divided into two parts as shown in Figure 19(c): the first part is the mechanical model that generates the blood volume changes due to blood pressure changes taking into account the arterial stiffness and blood flow dynamics, while the second part is the electrical model that converts the blood volume changes into electrical signals by the Bio-Z sensor. In this wok, we focus on the second part of the electrical model by considering the electrical properties of the tissue and blood volume changes as circuit models. We used a simple linear mechanical model for the blood flow and blood volume changes to show the performance of our electrical model, however, our modeling approach is flexible and can be augmented by any mechanical model for the blood volume changes for a more complex blood flow model.

To demonstrate the utility and validity of the model, we present the simulation of the arterial pulse wave and PTT monitoring from the wrist arteries for different sensing locations and parameters validated by extensive experimental characterization. The source code of the proposed model with examples are available online to help designers and researchers to simulate different parts of the body with different blood flow properties and sensing configuration to understand design tradeoffs [42]. This simulation framework helps in understanding the electrical response of the tissue and blood flow, and the optimization of circuits and algorithms of arterial pulse sensing without the need for extensive experimentation. Our previous work [23] is extended in this manuscript by improving the tissue circuit model through presenting a complete 3D circuit model of the wrist similar to the anatomy of the wrist by modeling the impedance and electrical properties of the different tissue types of the wrist such as fat, muscle, and bone in addition to the skin-electrode impedance. Furthermore, the blood flow model is extended to model the arterial pulse wave in both radial and ulnar arteries of the wrist. We include a new simulation for the whole wrist model validated by experimental data to show the effect of changing the sensing location and the current injection frequency on the pulse signal.

The rest of the chapter is organized as follows. Background material is discussed in Section 2.5, followed by the description of the methods in Section Methods3.4. Then, we present simulation and experimental results in Section 3.5. Concluding remarks are presented in Section 3.6.

3.3. Background

Simple cardiac parameters like heart rate can be measured from the pulsation of surface blood vessels such as capillaries and veins; however, complex cardiac parameters such as BP and PTT require accurate measurement of the arterial pulse wave generated from the pulsation of arteries – the deep, main blood vessels that carry the oxygenated blood from the heart to the rest of the body. Bio-Z is superior at detecting arterial pulse wave compared to other modalities such as optical sensors like photoplethysmograph (PPG) for the following reasons: 1) Optical sensors only capture blood volume changes near the skin surface (*i.e.* from capillaries) because light has limited penetration into the tissue (up to 3 mm) [43, 44]. On the other hand, since Bio-Z relies on a current signal, it can reach deeper tissue [45]. Thus, the Bio-Z signal can reach deep arterial sites to provide more accurate monitoring of arterial blood volume changes. 2) Bio-Z is not affected by ambient light and skin tone, unlike PPG. 3) Bio-Z has a wider application space such as respiration and hydration measurements, further increasing its utility [45, 46].

One of the challenges in arterial pulse sensing with Bio-Z is the variation of the pulse morphology and features with the sensing parameters. As shown in previous work [47], when the distance between the artery and sensor changes, the pulse signal amplitude and morphology varies, confounding the estimation of dynamic parameters. Therefore, it is critical to study the effect of the electrode location relative to the artery and the distance between electrodes on the measured pulse signal. The pulse signal is affected by the propagation of the current signal injected from the current electrodes through the tissue and the pulsating blood vessels, which generates a voltage distribution in the tissue modulated by the pulse signal. The impedance of the tissue, as well as the artery's diameter and depth, are important factors that affect the measured pulse signal with complex interaction between them. In addition, parameters such as the distance between the electrodes, electrode size, and injection frequency are often selected empirically through experimentation, a long and tedious process. Therefore, there is a need for a better understanding of the current propagation in the tissue and arteries, and their response to the electrical stimulus through accurate modeling of the electrical properties of the tissue and blood flow.

Previous work on Bio-Z modeling and simulation suffered from several limitations. Finite element models (FEM) were used extensively in modeling bio-impedance of the tissue mainly for tomography and imaging applications. For example, the static impedance of breast and head tissue were modeled for electrical impedance tomography (EIT) using 2D FEM models [48, 49]. In [50], the sensitivity of the voltage measurements due to change in conductivity images was studied using a 2D impedance FEM model for EIT applications. In [51], a 2D static FEM model was developed for Bio-Z using COMSOL to model the artery pulsation for a cross-section of the tissue and the artery. This method considered the pulsation of the artery at a fixed time and did not show time propagation for the arterial wave that can model pulse transit time. On the other hand, circuit models were also used previously to model the electrical properties of the tissue by an impedance network relying on simple circuit analysis and simulation methods such as SPICE. which are fast and easy to use compared to FEM methods [52, 53]. In addition, the tissue circuit model can be augmented with the SPICE models of the sensing circuits to model complex current injections and sensing methods [53, 54]. SPICE simulation was also used to study 2D tissue for EIT applications and breast cancer detection [55, 56]. Previous work based on circuit SPICE models relied on constant impedance values to model the static behavior of the tissue and used simple models for the pulsatile activity inside the arteries which cannot provide a sufficient understanding of the signal distribution inside the tissue and blood flow [57].

The objective of this work is to introduce a fast and reliable method to model the electrical properties of the tissue, blood vessels, and electrical stimulation with realistic parameters to simulate Bio-Z sensing on different parts of the body where the results match measurements.

3.4. Methods

3.4.1. 3D Circuit Model of Tissue

The electrical properties of cells inside tissue and blood vessels are modeled as an equivalent electrical circuit by resistors R_I and R_E and a capacitor C_M, which represent the intra- and extra-cellular fluid resistance and cell membrane capacitance, respectively, as shown in Figure 3(a) [28]. The behavior of the resistive and reactive components of tissue impedance across frequency is plotted in Figure 3(b), which is called Cole-Cole plot. At low frequencies, the body impedance looks resistive (= R_E) and decreases to the parallel

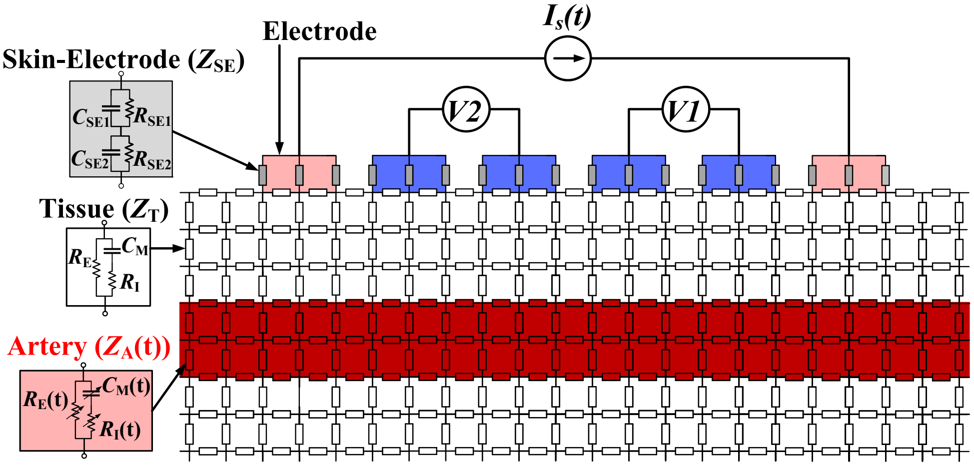

Figure 20. Cross-section of the proposed circuit grid model illustrating the impedance model for tissue (Z_T), artery (Z_A(t)) and skin-electrode impedance (Z_{SE}). Reprinted with permission from [3].

equivalent of R_E and R_I at high frequencies when the cell membrane capacitor shorts. The reactive part is zero at the extreme frequencies and is maximum at f_p.

The tissue impedance varies with location based on the spatial distribution of the different tissue types such as blood, fat, muscle, and bone. To accurately model this complex tissue impedance and blood flow, we divide the tissue into small 3D elements called voxels for high spatial resolution and assigned a time-varying Bio-Z equivalent circuit $Z(t)$. Then, the full tissue model consists of a large 3D network of connected voxels mimicking the physiology of the body and vasculature. This impedance model is a function of space, time, and frequency, denoted as $Z(x,y,z,t,f)$, as shown in Figure 19.

The electrical properties of the tissue such as fat, muscle, and bone are static and do not change with time, therefore the tissue voxel consists of static impedance (Z_T) with fixed resistors and capacitor (R_E, R_I, and C_M) of the cell equivalent circuit, as shown in Figure 20. However, the pulsation of blood inside arteries is a dynamic activity that changes blood volume with time, thus it is modeled as a time-varying impedance (Z_A(t)), as explained later.

The skin-electrode impedance (Z_{SE}) consists of multiple layers including the stratum corneum layer inside the skin and the conductive layer of the electrode [58]. Each layer can be modeled as a parallel resistor and capacitor (R_{SE} and C_{SE}). In our model, we

Table 5: Model parameters and their typical values. Reprinted with permission from [3].

Param.	Description	Typical Value
L	Length of the impedance voxel	2 mm
L_X	Body dimension in X-direction	85 mm
L_Y	Body dimension in Y-direction	70 mm
L_Z	Body dimension in Z-direction	38 mm
A_X	Artery's location in X-direction (Radial)	23 mm
	Artery's location in X-direction (Ulnar)	67 mm
A_Z	Artery's depth in Z-direction	2-4 mm
A_D	Artery's diameter	2 mm
PI_X	Position of lower current electrode in X-direction	23 mm
PI_Y	Position of lower current electrode in Y-direction	8 mm
PV_X	Position of lower voltage electrode in X-direction	23 mm
PV_Y	Position of lower voltage electrode in Y-direction	16 mm
S_V	Spacing between voltage electrodes	10 mm
S_I	Spacing between current electrodes	24 mm
E_X	Electrode size in X-direction	8 mm
E_Y	Electrode size in Y-direction	16 mm
ΔZ_A	Radial artery's impedance change	10%
	Ulnar artery's impedance change	5%
I_S	Current injection amplitude	0.5 mA
f_c	Current injection frequency	10 kHz
f_{HR}	Heart rate frequency (=1/IBI)	1 Hz
PTT_A	Pulse transient time between first and last voxel of artery's model	15 ms

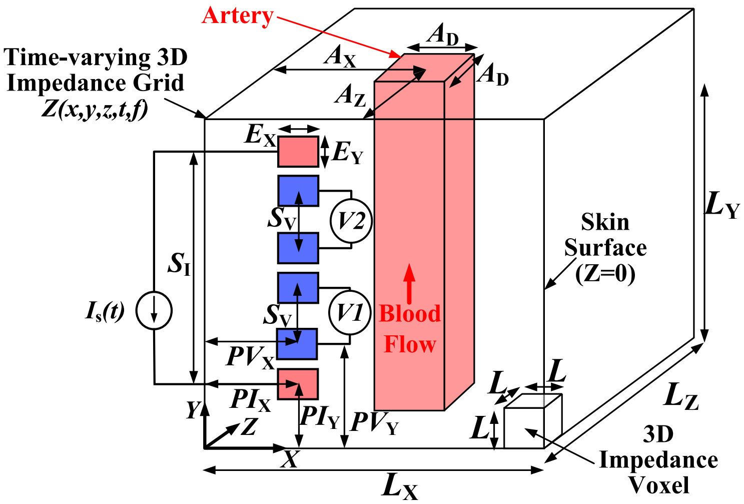

Figure 21. Geometrical parameters of the circuit model of the wrist and Bio-Z current injection and voltage sensing electrodes with dual voltage channels (*V1* and *V2*) for PTT monitoring. Reprinted with permission from [3].

used two layers of *RC* circuits to represent the skin-electrode impedance, as shown in Figure 20, as the best fit with our measurement data. Z_{SE} impedance is connected at the model top layer at each node that is covered by the electrode surface area and then connected together to represent the electrode terminal.

The proposed wrist 3D model simulates the electrical properties of the wrist with its constituent tissues of skin, fat, muscle, and bone according to the anatomy of the wrist. The model includes the blood pulsation and PTT of the radial and ulnar arteries at the wrist. The wrist and blood flow are modeled along the vertical direction (*Y*-axis) and the cross-section of the wrist along the *X* and *Z* axes assuming the skin surface is the $Z = 0$ plane. The Bio-Z electrodes for current injection and voltage sensing are placed vertically parallel to the arteries with two voltage channels (*V1* and *V2*) for continuous monitoring of the blood pulsation and PTT, as shown in Figure 21. This model is highly parameterized including the geometry of the 3D shape, arteries, voltage and current electrodes, and the

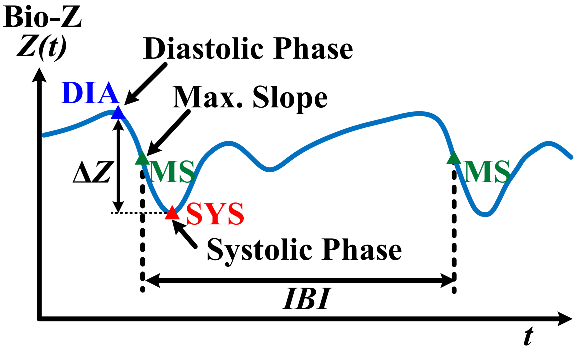

Figure 22. Typical Bio-Z signal showing the arterial pulse wave with the characteristic points: diastolic peak (DIA), max. slope (MS), and systolic foot (SYS) in addition to inter-beat-interval (IBI). Reprinted with permission from [3].

spatial resolution of the grid. The complete list of parameters in this model is shown in Table 5. This model is generalizable allowing it to be used to model any part of the body, for example, the chest, where time-varying impedance $Z(t)$ can model the heart and lung movements to simulate the impedance cardiogram and respiration rate, respectively.

3.4.2. 3D Circuit Model of the Artery

Each cardiac cycle, the heart pumps blood to the body causing a pressure pulse wave to travel through the arteries. Arterial stiffness controls PTT, which is the time taken by the pressure pulse to travel between two points along the artery. When the heart contracts, the artery's pressure increases from diastolic to systolic pressure which causes expansion of the artery's diameter from D_A to $D_A+\Delta D_A$ with an increase of blood volume from v to $v+\Delta v$. The increased blood volume leads to higher conductivity and causes the Bio-Z to decrease by ΔZ, as illustrated in Figure 22 by the sudden drop from the diastolic peak (DIA) to the systolic foot (SYS) passing through the maximum slope point (MS), which are the characteristic points of the Bio-Z cardiac cycle. After the Bio-Z reaches the foot, it increases gradually to the next diastolic peak, which repeats every cardiac cycle with the inter-beat-interval (IBI). A smaller foot exists after some time from the main foot indicating blood reflections that occur due to branching in the arteries. The ΔZ reduction in Bio-Z is equivalent to a decrease in the extra- and intra-cellular fluid resistances, ΔR_E and ΔR_I, and an increase in the cellular membrane capacitance, ΔC_M. The increase in blood vessel diameter during the pulsation results in an increase in the cross-sectional area of the blood vessel that is associated with a decrease in the equivalent resistance of the blood vessel according to $R = \rho L/A$, where ρ, A, and L are the blood resistivity, area, and length of the blood vessel, respectively. In addition, the increase in blood volume can be interpreted as an increase in total surface area of the cells which leads to an increase in the equivalent cell membrane capacitance according to $C = \varepsilon A/d$ where ε, A, and d are the blood permittivity, area of the cell membrane, and its thickness.

$$Z_A(t) = Z_A - \Delta Z_A \sin\big(2\pi f_{HR}(T - td_i)\big) \tag{3.1}$$

$$Z_A(t) = \begin{Bmatrix} R_I - \Delta R_I \sin\big(2\pi f_{HR}(T - td_i)\big) \\ R_E - \Delta R_E \sin\big(2\pi f_{HR}(T - td_i)\big) \\ C_M + \Delta C_M \sin\big(2\pi f_{HR}(T - td_i)\big) \end{Bmatrix} \tag{3.2}$$

$$td_i = \frac{i}{N} PTT_A \ \text{ for } \ i = 0 \ \text{ to } \ N - 1 \tag{3.3}$$

In the proposed model, the artery's time-varying impedance $Z_A(t)$ includes a static component Z_A modeled by the blood impedance model (R_I, R_E, and C_M) in addition to a variable component that changes with time to model blood volume changes due to the arterial pulse wave as shown in (3.1). The variable impedance of the blood pulse is approximated by a sinusoidal waveform that models the change in pulse impedance

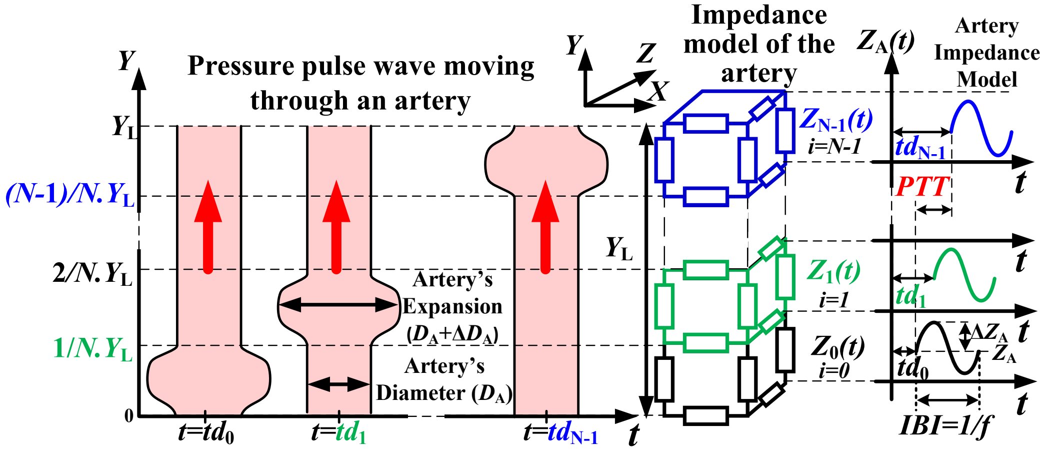

Figure 23. The proposed 3D model of the artery showing the impedance waveform $Z_A(t)$ at each voxel of the artery due blood volume changes with PTT. Reprinted with permission from [3].

amplitude of ΔZ_A (equivalent to ΔR_E, ΔR_I, and ΔC_M) at heart rate frequency f_{HR}, which is the inverse of IBI. We used the approximate sinusoidal waveform for impedance and voltage pulses because we focus on the peak-to-peak changes in voltage due to impedance change rather than the morphology of the pulse signal and to simplify the estimation of the delay of the voltage pulse signal. The artery's model equations are shown in (3.2) for each resistive and capacitive component of the artery's circuit model. The model is unique in considering both the spatial and temporal properties of blood flow, which allows modeling of the PTT that is related to arterial stiffness and essential for the estimation of hemodynamic parameters such as BP. To model PTT, each 3D voxel along the artery's location is assigned a delayed sinusoidal impedance waveform of delay td_i that increases linearly along the direction of blood flow as in (3.3) from $i = 0$ to $N - 1$, where i is the voxel index, N is the total number of artery's voxels in the Y-direction, and PTT_A is the total delay of the pulse from the first to the last voxel along the artery, as shown in Figure

23. Despite using a linear blood flow model as an example, our modeling approach is flexible and can use any input model for the blood volume changes with non-linear function for each voxel in our 3D model. This approach allows applying any non-linear blood flow model by integrating a non-linear mechanical model with our electrical model for a more complicated and realistic artery model.

3.4.3. Model Parameter Selection

The model parameters were selected to represent the wrist tissue and arteries with Bio-Z sensor for measuring PTT from wrist arteries through two voltage sensors *V1* towards the elbow and *V2* towards the hand, as shown in Figure 24. The geometrical parameters of the model were chosen to reflect a simplified 3D model of the wrist anatomy. In literature, the anatomy of the wrist shows the distribution of the different tissue types and the location of the radial and ulnar arteries in the wrist, as shown in Figure 24(a). The anatomy of the wrist was approximated by the proposed allocation of the tissue such as muscle, fat, and bone, as shown in the impedance map of the wrist as illustrated in the 2D cross-section and 3D plots in Figure 24(b, c, and d). We chose the impedance grid resolution (voxel size) to be $L = 2$ mm to balance between the spatial resolution and simulation complexity. The size and the depth of the radial and ulnar arteries were selected to be $D_A = 2$ mm and $Z_A = 4$ mm, respectively, according to previous work that studied the average parameters of the radial artery of the wrist from 44 human subjects [59]. This study shows that the artery's depth increases towards the elbow. This depth variation was included in the model by increasing the depth of the arteries in the model from 2 to 4 mm

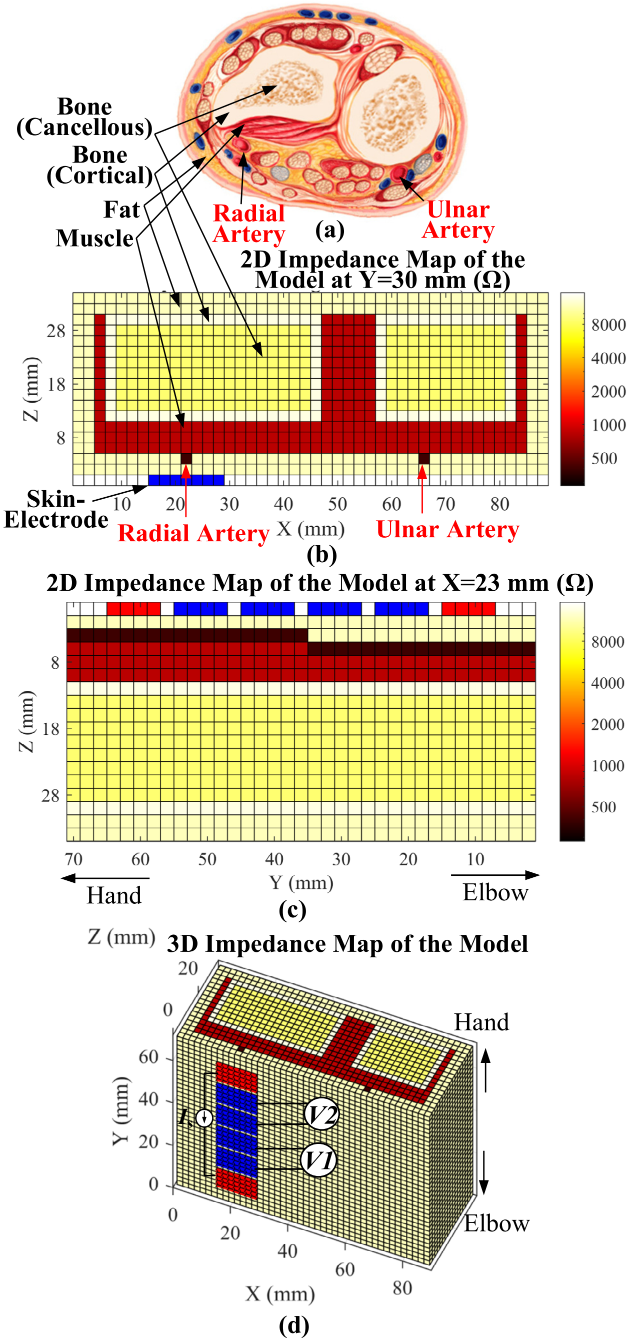

Figure 24. Proposed wrist circuit model: (a) cross-section of the wrist anatomy, (b) 2D impedance map of the model at Y = 30 mm, (c) 2D impedance map at X = 23 mm, and (d) 3D impedance map. Reprinted with permission from [3].

in

the lower half of the Y-direction of the model when the artery is closer to the elbow as shown in Figure 24(c). The dimensions and location of electrodes were selected to match the experimental results where electrodes for current injection and dual voltage sensing are typically placed over the radial artery as shown in Figure 24(d).

The DC impedances of tissue and blood were selected based on the electrical properties of conductivity and permittivity for each tissue type that changes with the biological structure of the tissue and frequency ranges. Each frequency range exhibits its characteristic response which is represented by distributions of relative permittivities in complex function in frequency called the Cole-Cole equation as follows

$$\hat{\varepsilon}(\omega) = \varepsilon_\infty + \sum_n \frac{\Delta\varepsilon_n}{1+(j\omega\tau_n)^{1-\alpha_n}} + \frac{\sigma}{j\omega\varepsilon_0} \qquad (3.4)$$

where ε_∞ is the high-frequency permittivity, σ is the tissue conductivity, ε_0 is the permittivity of free space, ω is the angular frequency, and each frequency range is defined by its $\Delta\varepsilon_n$ as the low-frequency permittivity, τ_n is the characteristic relaxation time, α_n is the distribution parameter. The Cole-Cole parameters that simulate the electrical properties of the tissue based on experimental measurements are published in [27] for each tissue type and an example for the blood is shown in Table 6. The conductivity and permittivity of blood are plotted in Figure 25(a) versus frequency from 1 Hz to 100 GHz showing their variations with frequency and its Cole-Cole plot is illustrated in Figure

Table 6: Cole-Cole model parameters for Blood. Reprinted with permission from [3].

$\boldsymbol{\varepsilon_\infty}$	$\boldsymbol{\Delta\varepsilon_1}$	$\boldsymbol{\tau_1(ps)}$	$\boldsymbol{\alpha_1}$	$\boldsymbol{\Delta\varepsilon_2}$	$\boldsymbol{\tau_2(ps)}$	$\boldsymbol{\alpha_2}$	$\boldsymbol{\sigma}$
4.0	56.0	8.38	0.10	5200	132.63	0.1	0.7

Table 7: Impedance parameters of circuit models for frequency range 1-100 kHz and voxel length L=2 mm. Reprinted with permission from [3].

Tissue Type	**R (kΩ)**		**C (nF)**		**Z (kΩ) @ 10 kHz**	**Avg. Error (%)**
	R_E	**R_I**	**C_M**	**-**		
Blood	0.4	1.0	0.164	-	0.4	0.0
Muscle	0.8	4.3	0.468	-	0.8	3.2
Bone Cancellous	8.7	85.3	0.034	-	8.7	1.7
Fat	13.4	93.2	2.090	-	11.7	1.9
Bone Cortical	13.8	95.6	0.009	-	13.8	0.7
Skin-Electrode	**R_{SE1}**	**R_{SE2}**	**C_{SE1}**	**C_{SE2}**	61.3	4.9
	1045.0	24.2	0.293	0.025		

25(b), which is real versus the imaginary impedance as calculated from the complex permittivity in (3.4).

We estimated the DC impedance parameters of our circuit model (R_I, R_E, and C_M) for each tissue type by fitting to the Cole-Cole model in (3.4) for a certain frequency range using non-linear least-square curve fitting. The Levenberg-Marquardt method was used for curve fitting by minimizing error for the real, imaginary and magnitude components of the impedance. The estimated DC impedance parameters of our circuit model (R_I, R_E, and C_M) for each tissue type for the frequency range 1-100 kHz are listed in Table 7.

The impedance error between the circuit model and the Cole-Cole model varies for tissue type and the selected frequency range based on how the tissue Cole-Cole plot is like the theoretical model. To illustrate this variation, we estimated three circuit models for blood for different frequency ranges, as shown in Figure 25(b). The first and third circuit models showed smaller errors compared to the second model, as shown in Table 8, since the Cole-Cole plot is like the theoretical shape for these frequency ranges. This explains the variation in error for the different models and the mismatch in the Cole-Cole plots for the different tissue types used in the model, as shown in Figure 25(c). The model accuracy is evaluated by the average error in impedance between our circuit model and the reference which varies with tissue type and is less than 5% as shown in Table 7. The error is acceptable because it has a small effect on Bio-Z voltage that is linearly proportional to the equivalent impedance and the voltage error will be upper-bounded by this small error value. For future improvements, multiple circuit models can be used for each tissue type for different frequency ranges to minimize the error and extend the frequency range of the simulations.

The skin-electrode impedance parameters (R_{SE1}, R_{SE2}, C_{SE1}, and C_{SE2}) were estimated by fitting the model to experimental data that were collected from wet electrodes in our lab for discrete frequency points in the range from 3 to 25 kHz. The resistor and capacitor values shown in Table 7 are scaled for voxel length L=2 mm that is used in the proposed model by multiplying the resistance and dividing the capacitance by a scaling

Table 8: Impedance parameters for blood circuit models for voxel length L=2 mm. Reprinted with permission from [3].

Blood Circuit Model	**Frequency Range**	***R* (kΩ)**		***C* (pF)**	**Avg. Error (%)**
		R_E	**R_I**	**C_M**	
Circuit Model 1	0.001 – 1 MHz	0.4	0.82	15.3	0.18
Circuit Model 2	5 – 50 MHz	0.26	0.5	5.2	5.1
Circuit Model 3	0.2 – 1GHz	0.22	0.007	2.0	1.97

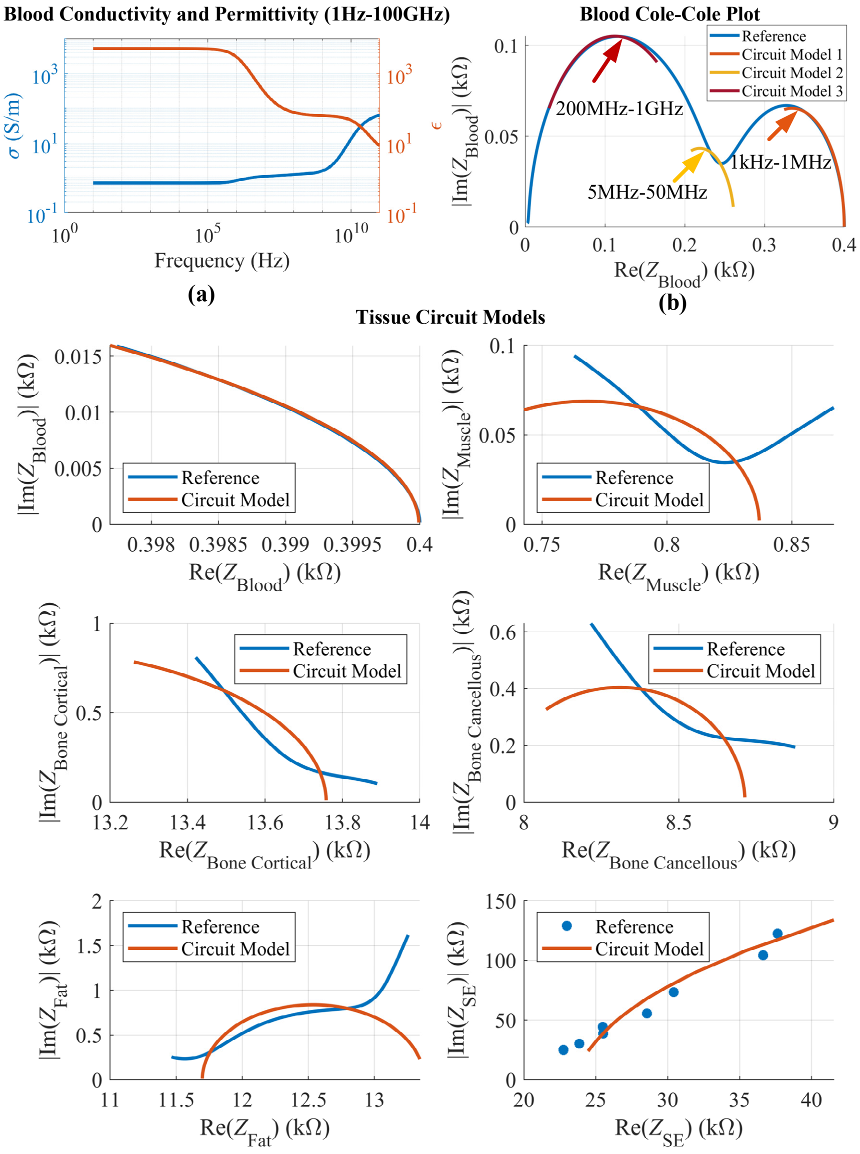

Figure 25. (a) Blood conductivity and permittivity (1Hz – 100GHz), (b) blood Cole-Cole plot and three different circuit models, and (c) Cole-Cole plot of the real and imaginary components of the tissues (1 – 100 kHz) and skin-electrode impedance (3 – 25 kHz), as estimated by the circuit model versus the reference Cole-Cole model. Reprinted with permission from [3].

factor estimated from fitting the electrode voltage simulation results with the actual measurements. In Table 7, the values of the estimated circuit model are presented with the impedance value at 10 kHz for each tissue type. The impedance of blood is the smallest, followed by muscle, cancellous bone (inner bone), fat, cortical bone (outer bone), and finally the skin-electrode is the highest impedance as expected.

The amplitude of the artery's variable impedance component, ΔZ_A, represents the mechanical properties of arterial blood flow such as arterial stiffness and wall thickness, *etc.,* which are not represented by the other geometrical and electrical parameters in our model and varies between radial and ulnar arteries and from one subject to another. The parameter ΔZ_A affects the pulsatile activity of the artery and affects the voltage pulse amplitude ΔV_{pp}. We estimated an average ΔZ_A as a ratio of blood impedance Z_{Blood} based on experimental measurements for each subject by iteratively minimizing the error of the average ΔV_{pp} between the simulation results and measurements while changing the sensing location across the wrist. From literature, the pulsatile activity of the radial artery is larger than the ulnar artery which is supported by our choice of larger ΔZ_A for the radial artery of 10% compared to 5% for the ulnar artery [60]. We selected PTT_A = 15 ms for the artery's model to match the experimental measurements of PTT across the same distance on the wrist.

3.4.4. Simulation Flow

The proposed 3D circuit model is based on a SPICE netlist with a large network of resistors and capacitors. The Bio-Z simulation platform uses MATLAB to generate the SPICE netlist with a 3D grid of time-varying impedances $Z(x,y,z,t,f)$ and current source $I_s(t)$ according to the model parameters, as shown in Figure 26(a). In the SPICE netlist, the current source is connected to the assigned nodes of the current electrodes through the skin-electrode impedance. The effect of electrode size is modeled by connecting all the

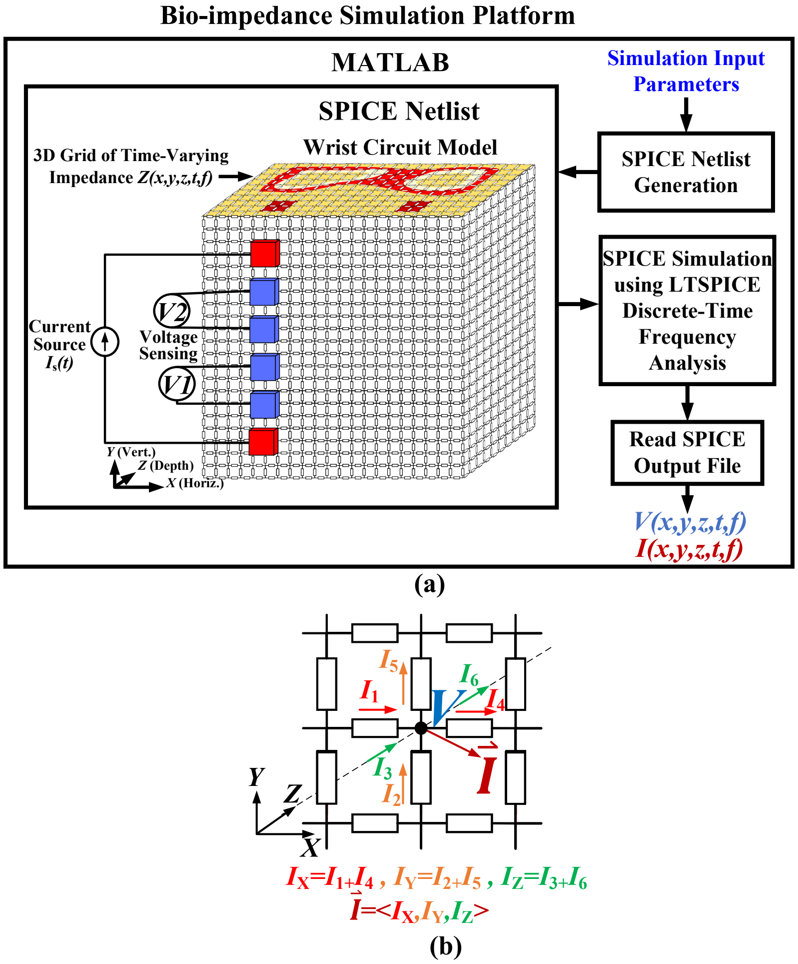

Figure 26. (a) The simulation flow for the circuit model using SPICE simulation and MATLAB for the generation of voltage and current distributions, (b) current vector ($\vec{I}$) calculation at each node of the circuit model. Reprinted with permission from [3].

nodes within the area of the electrodes at the specified electrode location on the surface plane of the 3D model, $Z = 0$. Then, MATLAB invokes LTSPICE to run the simulation with the specified simulation options (*e.g.*, simulation time, time step, and start and stop frequencies for frequency analysis). Post simulation, MATLAB reads the LTSPICE results that contain the voltage at each node and the current through each element and arranges the data in a multi-dimensional array, $V(x,y,z,t,f)$ and $I(x,y,z,t,f)$ that maps to the

3D grid for post-processing, as shown in Figure 26(a). The resulting sensor voltages, $V1$ and $V2$, are calculated by the difference of the voltage between the electrodes. A current vector $\vec{I} =< I_X, I_Y, I_Z >$ is calculated at each node from the equivalent current in each dimension, as shown in Figure 26(b).

The simulation time needs to be at least one period of a heartbeat (~1 s) to simulate the low-frequency variation of blood flow at f_{HR} =1 Hz simultaneously with the high-frequency current injection signal at f_{c} from 1 to 100 kHz. This transient simulation will take a long time because of the small simulation time step required by the high-frequency current signal Furthermore, synchronous IQ demodulation must be performed to extract the complex impedance signal from the amplitude and phase of the AC voltage signal. Therefore, we used a series of fast AC analysis (.ac) SPICE simulations at different time steps to mimic the AC response of the circuit at a specific frequency for the full pulse period to get the complex impedance values. This is repeated for 8-time steps in the pulse period using a different netlist for each time step that reflects the change in the values of resistors and capacitors with time steps according to the model of the blood volume changes due to the arterial pulse. Afterward, the results are concatenated in time to form the voltage signal, $V_{\mathrm{sim}}(t)$. The proposed stepwise AC analysis provides more control over the time steps and is more than 200x faster in simulation time compared to the transient analysis that uses variable time steps. This approach assumes independence between the AC responses at the different time steps because the changes in impedance because of the pulse signal is very slow compared to the time constant of the resistors and capacitors of the tissue which is validated by a transient simulation that matches our AC simulation as shown later.

The simulated Bio-Z voltage signal, $V_{\mathrm{sim}}(t)$, consists of a DC component, V_{dc}, and an AC component, ΔV generated from impedance changes ΔZ from the pulse wave, as shown in Figure 27(a). $V_{\mathrm{sim}}(t)$ is a sinewave with different amplitudes and delays that is affected by the transfer function of the model and the sensing configuration. The amplitude ΔV_{pp}, DC offset V_{dc}, and delay T_{d} of the voltage signal were estimated using a regression model that fits the measured data to the expected sinewave with variable parameters as in

$$V_{\mathrm{sim}}(t) = V_{\mathrm{dc}} + \left(\frac{\Delta V_{\mathrm{pp}}}{2}\,\mathrm{SIN}\big(2\pi f_{\mathrm{HR}}(T - T_{\mathrm{d}})\big)\right) \qquad (3.5)$$

The parameters are estimated by minimizing the RMSE error between the readings and (3.5). The PTT is calculated from the difference of time delay T_{d} between *V1* and *V2.*

We carried out a comparison between the proposed stepwise AC analysis and the alternative transient analysis by the simulation of a simple model with small dimensions of 8×28×6 mm, single-node electrodes, $f_{\mathrm{HR}} = 1$ Hz, and $f_{\mathrm{c}} = 30$ Hz to validate the stepwise AC analysis approach and to show the relation between the output signals. The SPICE netlist for the transient analysis included the resistors and capacitors expressed as time functions as in (3.2), which results in a high-frequency signal at f_{c} modulated with the Bio-Z in its amplitude and phase at the low heart rate frequency f_{HR}. However, the proposed stepwise AC analysis method results in the modulated Bio-Z signal directly that matches the envelope of the transient analysis for both *V1* and *V2* which validate our AC simulation approach as shown in Figure 27(c). The simulation time for our proposed AC analysis and transient analysis are plotted in Figure 27(d) versus the number of nodes of the model for

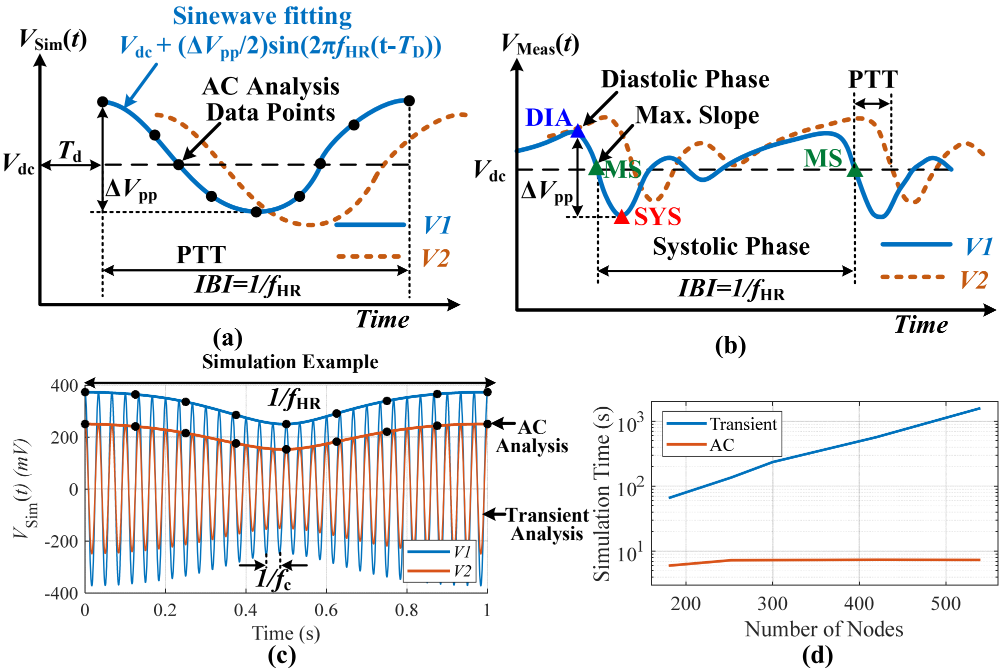

Figure 27. (a) Voltage signals from AC analysis, $V_{\text{sim}}(t)$, (b) actual Bio-Z voltage signals, $V_{\text{Meas}}(t)$, showing the DC and AC components, V_{dc} and ΔV_{pp}, respectively in addition to pulse time delay (T_{d}) and pulse transit time (PTT) between *V1* and *V2*, (c) SPICE simulation example for the voltage signals with transient versus AC analysis with $f_{\text{HR}} = 1$ Hz and $f_{\text{c}} = 30$ Hz, (d) simulation time of transient and AC analysis versus number of nodes. Reprinted with permission from [3].

the simulation of one heart pulse period for one second with carrier frequency $f_{\text{c}} = 10$ kHz. The simulation of AC analysis is 200x faster compared with transient analysis with 7.36 seconds for AC analysis and 1,588 seconds for transient analysis for a model with 540 nodes because the transient analysis requires 240k time steps compared to only 8-time steps for our proposed AC analysis. The simulation time of the transient analysis increases at a higher order versus the number of nodes and requires 116x more storage compared to the AC analysis which makes transient analysis prohibitively expensive for models with a larger size. Therefore, the proposed model allows efficient Bio-Z simulation both in time and frequency.

3.4.5. Bio-Z Measurement System

For validation between the simulation and measurement results, we carried out an extensive characterization of the Bio-Z signal for different configurations. The characterization was done by measuring Bio-Z from the wrist using custom hardware and signal processing algorithms that are capable of measuring multi-channel, high-resolution impedance signal that captures the pulse signal due to blood volume changes in the wrist arteries, as shown in Figure 28 [1]. The Bio-Z measurement system has a high sampling rate of 93.75 kSps to measure small PTT values. We extract Bio-Z voltage based on synchronous IQ demodulation to get both the real and imaginary components with programmable frequency from 3 to 25 kHz. Using the current injection signal for Bio-Z at 10 kHz compared to the low-frequency flicker noise provides higher immunity to noise and 60 Hz interference compared to other baseband physiological signals such as ECG and EEG. Our measurement system includes a PPG signal from the finger using an optical finger clip that is measured simultaneously with the Bio-Z channels to provide a reference for the pulse signal.

Values for V_{dc} and ΔV_{pp} based on the average beat-to-beat values over a period were calculated from the measured data based on the 3 characteristic points detected in each cardiac cycle (DIA, MS, and SYS). These points were detected based on the peak, foot, and zero-crossing points of the first derivative of the signal [1]. V_{dc} is the voltage of MS point, while ΔV_{pp} is the difference between the voltage of DIA and SYS points, as

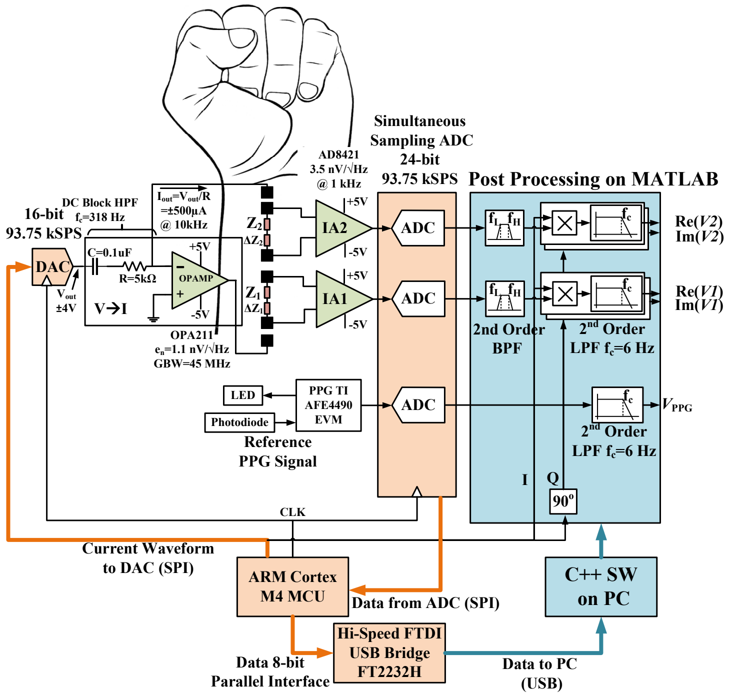

Figure 28. Block diagram of custom Bio-Z measurement hardware and algorithms that depends on IQ demodulation for extracting the real and imaginary parts of Bio-Z with dual voltage channels of *V1* and *V2* for PTT measurements. Reprinted with permission from [3].

shown in Figure 27(b). PTT is measured by the time difference between MS points of *V1* and *V2* signals. All values are calculated by the average over all valid heart beats within the data collection time. To evaluate the accuracy of the measured pulse signal, the inter-beat-interval RMSE relative to a reference signal measured from a clip-on PPG sensor was calculated. PPG from the finger was chosen as a reliable reference for the arterial pulse signal at the wrist because the measured light signal is focused on a single artery in the finger and measures the blood volume changes of the finger's artery from the transmission of the light through the artery. Furthermore, the pulse signal at the finger is measured at a very short distance after passing through the wrist arteries, which is a good approximation for the arterial signal at the wrist. The IBI for Bio-Z and PPG signals were

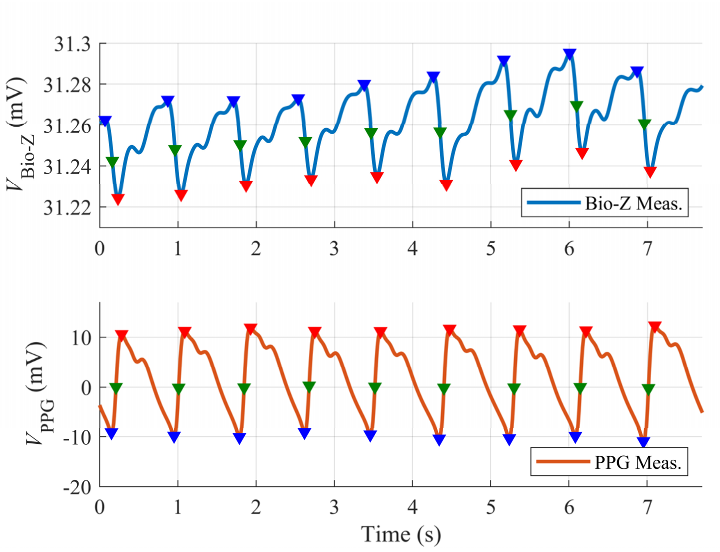

Figure 29. Measured Bio-Z signal ($V_{\text{Bio-Z}}$) and PPG signal (V_{PPG}) showing the DIA (blue), MS (green), and SYS (red) points. Reprinted with permission from [3].

measured by the difference between each successive MS point. When the IBI RMSE increases, this indicates a less accurate and noisy Bio-Z pulse signal. An example of the measured Bio-Z and PPG signals are shown in Figure 29, highlighting the DIA, MS, and SYS points for each signal that were used to calculate V_{dc}, ΔV_{pp}, and the IBI RMSE. The PPG pulse signal is the opposite of the Bio-Z because higher PPG voltage means larger blood volume.

3.5. Results

In this section, we show the simulation results of V_{dc}, ΔV_{pp} and PTT for the proposed wrist circuit model versus changing the voltage electrodes location, the current injection location relative to the artery, electrode size, and the current injection frequency, validated by Bio-Z measurements from the wrist. We collected Bio-Z data from multiple human subjects under Texas A&M University IRB (IRB2017-0086D). The actual location of the wrist arteries was detected using a Huntleigh Dopplex MD2 Bi-Directional Doppler, which measures arterial blood flow using a probe with high spatial sensitivity. For the Bio-Z measurement settings, we used current injection with typical values as used in simulation with an amplitude of 0.5 mA at a frequency of 10 kHz, which are compliant with safety standards [30]. There are expected variations from one subject to another because of anatomical differences in the tissue and arteries. Therefore, we developed our conclusions based on the average data from multiple subjects. In addition, there is a normal variation across the different parameter steps due to physiological changes that occurs over time or due to motion artifacts. Despite careful considerations to minimize these effects, these variations may occur and therefore we use a polynomial curve fitting to extract the trend of our measurements versus the target parameter that is compared with our model.

3.5.1. Simulation Example

Figure 30 illustrates the voltage and current distribution using the typical simulation value as resulted from the proposed model shown in Figure 24. The 3D voltage distribution at each node in the tissue model shows a maximum voltage of 200 mV at the location of the input current electrode (closer to elbow at $Y = 12$ mm) relative to the other

Table 9: Simulation Results of voltage sensors. Reprinted with permission from [3].

Voltage Sensor	V_{dc} **(mV)**	ΔV_{pp} **(μV)**	T_d **(ms)**
V1	49.02	17.84	3.53
V2	39.72	26.63	10.94

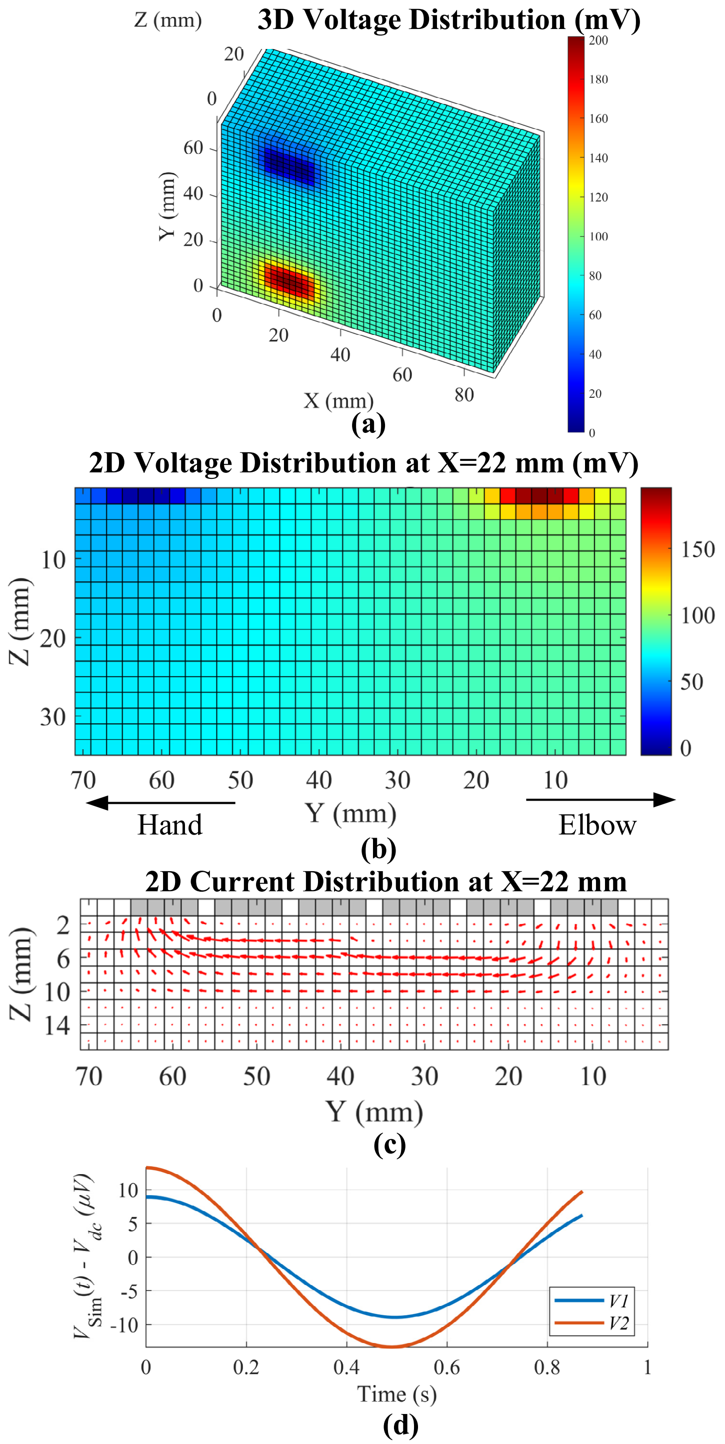

Figure 30. Voltage and current simulation results: (a) 3D voltage distribution of the tissue, (b) 2D voltage distribution at $X = 22$ mm, (c) 2D current distribution at $X = 22$ mm, and (d) the sensor voltage signals (*V1* and *V2*) with variation over time due to blood flow. Reprinted with permission from [3].

current electrode (closer to hand at $Y = 62$ mm) with the minimum voltage, as shown in Figure 30(a). The voltage changes gradually in the tissue going away from the current electrodes in the three dimensions approaching the middle voltage range of around 100 mV as shown in the 2D voltage distribution at $X = 22$ mm in Figure 30(b). The current vector distribution inside the tissue is plotted by red arrows with arrow's length proportional to the current amplitude, as shown in Figure 30(c). The current flows inside the tissue between the current electrodes with maximum current amplitude at the artery's location because of the lower impedance of blood compared to the other tissues of the wrist. The V_{dc} simulation result of voltage sensor *V2* is 39.72 mV, which is lower than V1 with V_{dc} of 49.02 mV because of the closer artery at *V1* compare to *V2,* which reduces the impedance and V_{dc} as shown in Table 9. The variable component of *V1* and *V2* due to blood flow are plotted versus time in Figure 30(d) with a sinusoidal waveform as a response to the artery's variable impedance model with large ΔV_{pp} of 26.63 µV for *V2* compared to 17.84 µV for *V1* due to closer artery at *V2*. The pulse arrival time at *V1* and *V2* is estimated from the time delay T_d as 3.53 and 10.94 ms for *V1* and *V2* respectively that shows the direction of blood pulse along the artery in the *Y*-direction from *V1* to *V2*. The results of this simulation illustrate the operation of the model as expected that can capture the electrical properties of the tissue and the blood flow.

3.5.2. Effect of Voltage Electrode Location

We studied the effect of electrode position on V_{dc} and ΔV_{pp} by changing the horizontal and vertical location of the voltage electrodes as well as the spacing between them while fixing the current electrode's location. Simulations were validated against

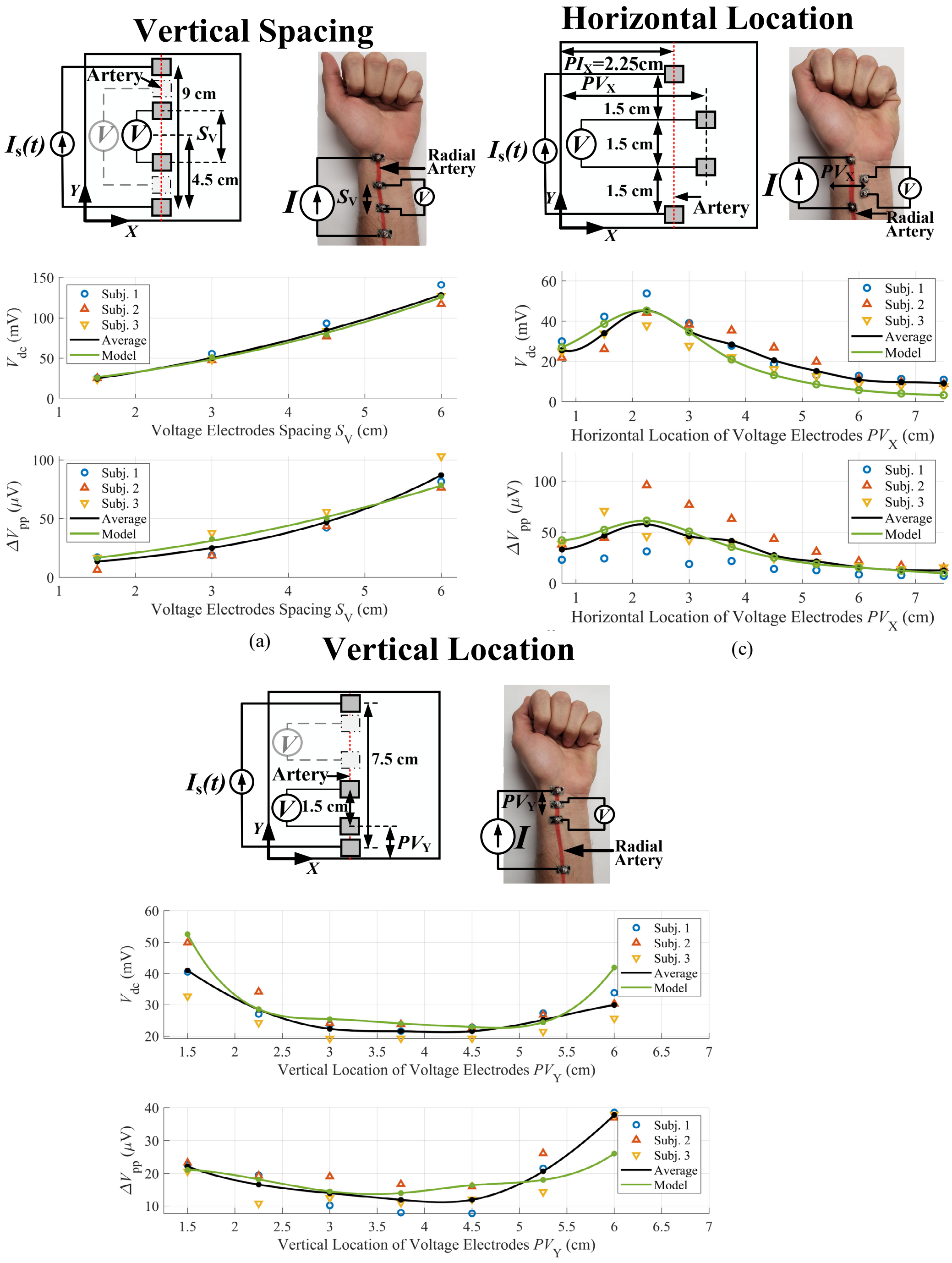

(a)

(c)

(b)

Figure 31. Comparison between the simulated and measured V_{dc} and ΔV_{pp} for different (a) voltage electrode spacing S_V, (b) vertical location of voltage electrodes PV_Y, and (c) horizontal location of voltage electrodes PV_X. Reprinted with permission from [3].

human subject ($n = 3$) Bio-Z measurements by taking the average of data collected over 3 minutes at each position. To study the effect of voltage electrode spacing, we placed two pairs of wet electrodes (1.6×0.85 cm^2) aligned on the radial artery of the wrist. The spacing (S_V) between the voltage electrodes was varied from 1.5 to 6 cm, centered around the midpoint between the current electrodes, which were 9 cm apart. Both simulations and measurements showed an increase in V_{dc} and ΔV_{pp} with increasing S_V, as shown in Figure 31(a).

The effect of the vertical location of the voltage electrodes relative to current electrodes was also studied. Current electrodes were placed with 7.5 cm spacing while changing the vertical location of the voltage electrodes (PV_Y) from 1.5 to 6 cm relative to the upper current electrode, as shown in Figure 31(b), with a spacing of 1.5 cm between them. Both simulations and measurements showed a minimum in V_{dc} and ΔV_{pp} when the voltage electrodes were in the middle and a peak when the voltage electrodes were closer to the current electrodes (minimum and maximum PV_Y) because of higher current amplitude near the current electrodes compared to the middle. Measurements and simulations showed a lower V_{dc} peak towards the hand (larger PV_Y) because of the smaller artery's depth with a lower impedance of blood closer to the skin that decreases voltage compared to the other side towards the elbow. However, ΔV_{pp} showed a higher peak towards the hand because of the small depth of the radial artery towards the hand which results in more pulsation compared to the other side of the wrist towards the elbow.

To study the effect of the horizontal location of voltage electrodes PV_X, we placed wet electrodes (0.85×0.85 cm^2) on the radial artery ($PI_X = 2.25$ cm) of the wrist with 4.5

cm spacing between the current electrodes while changing the horizontal distance of the voltage electrodes PV_X from 1.5 cm at the left of the radial artery ($PV_X = 0.75$ cm) to 5.25 cm at the right of the artery ($PV_X = 7.5$ cm) with 1.5 cm spacing between the voltage electrodes. Both measurements and simulations showed a peak in V_{dc} and ΔV_{pp} when the voltage electrodes are aligned with the current electrodes ($PV_X = 2.25$ cm) and they decrease as PV_X increases, as shown in Figure 31(c). It can be concluded from these results that V_{dc} and ΔV_{pp} can be maximized if the voltage electrodes are placed as close as possible to the current electrodes at the artery's location.

3.5.3. Effect of Sensing Location Relative to the Artery

For accurate estimation of hemodynamic parameters using wearable devices, it is important to understand the effect of sensing location relative to the artery on the quality of the sensed pulse signal. In this experiment, we show the simulation and measurement results of ΔV_{pp} of the pulse signal and IBI RMSE for changing the Bio-Z sensing location including the current and voltage electrodes horizontally with a fine step on the wrist from the radial to the ulnar artery.

We used a custom wrist band that includes an array of 8 columns and 6 rows of silver electrodes with size 5×5 mm and spacing of 3 mm. Each column consists of 6 electrodes for current injection and simultaneous monitoring of two voltage channels (*V1* & *V2*). Measurements repeated for 8 different sensing locations at each column with horizontal sensing location PI_X varies from 8 to 62 mm on the wrist with a small step of 8 mm. Data was collected from 3 participants for 5 minutes at each sensing location. The average location of the radial artery for participants was between columns 2 and 3 ($PI_X =$

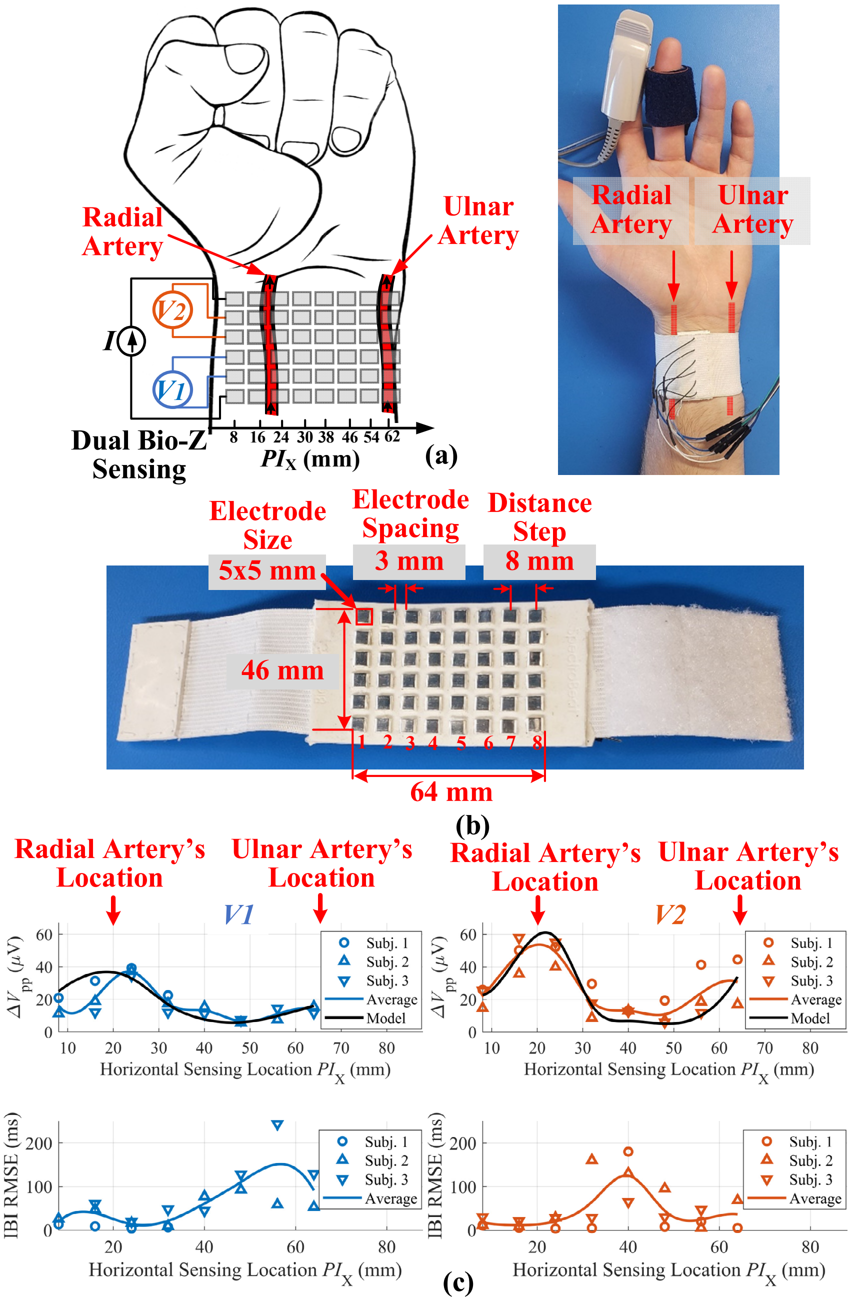

Figure 32. The effect of sensing location on pulse signal: (a) the location of the electrode array on the wrist, (b) picture of the custom electrode array wrist band, (c) the measurements and model results of ΔV_{pp} and IBI RMSE versus horizontal sensing location PI_X. Reprinted with permission from [3].

16 to 24 mm), while the ulnar artery was located around column 8 ($PI_X = 62$ mm) as shown in Figure 32(a, b). The 3D simulation model used the same dimensions for the sensing

locations and electrode size quantized by $L = 2$ mm.

The measurement results in Figure 32(c) shows the variation of ΔV_{pp} amplitude versus the horizontal sensing location PI_{X} for each subject in addition to the calculated average of all subjects. For the upper voltage channel closer to the hand (*V2*), there is a significant peak of $\Delta V_{\mathrm{pp}} = 60$ µV around the location of the radial artery at $PI_{\mathrm{X}} = 20$ mm and a smaller peak of 30 µV at the location of the ulnar artery at $PI_{\mathrm{X}} = 62$ mm, because of the weaker pulsation of the ulnar artery compared to the radial artery. The voltage channel *V1* towards the elbow shows a similar trend for ΔV_{pp}, but with smaller amplitude because of the larger depth of arteries under the skin towards the elbow.

It is important to maximize the amplitude of ΔV_{pp} to achieve the best quality of pulse signal that leads to accurate detection of fiducial points and IBI for reliable hemodynamic parameter estimation. The IBI RMSE of this measured data was minimum with 10 ms at the peak of ΔV_{pp} at $PI_{\mathrm{X}} = 20$ as shown in Figure 32(c). When the amplitude of ΔV_{pp} decreases at the location between the arteries, the signal becomes noisy which degrades the quality of characteristic point detection and results in high IBI RMSE of around 150 ms. This shows the significant effect of the sensing location relative to the artery on the quality of the pulse signal and the importance of selecting the right sensing location close to the artery for the best physiological monitoring of cardiac signals.

The model simulation results of ΔV_{pp} versus PI_{X} matches exactly the measurement results for both *V1* and *V2* which shows the capability of the proposed model to accurately simulate the effect of sensing location relative to both radial and ulnar arteries taking into consideration the different behavior for both arteries and both voltage channels *V1* and *V2*.

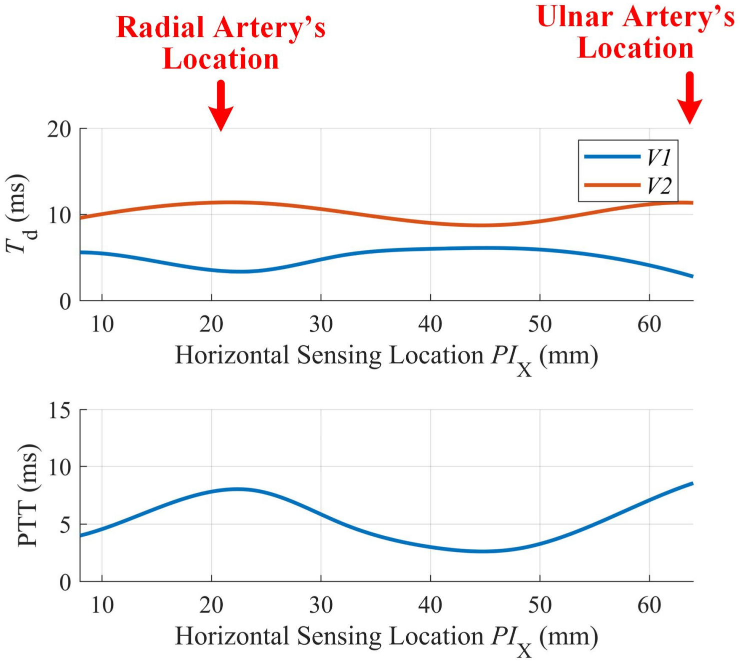

Figure 33. Simulation results of the voltage signal delay T_D for *V1* and *V2* (top), and PTT between *V1* and *V2* versus horizontal sensing location PI_X. Reprinted with permission from [3].

3.5.4. PTT Variation with Sensing Location

One of the important outcomes of the proposed model is understanding how the measured PTT changes with the sensing location since the PTT measured from the delay between the voltage sensors is affected by the tissue between the artery and the sensors. Based on the previous simulation, we extracted the time delay information T_d representing the arrival time of the pulse wave at each voltage channel (*V1* and *V2*) versus the horizontal sensing location PI_X, shown in Figure 33, with artery's model PTT_A equal to 15 ms. The simulation results show that the pulse arrival time changes with PI_X by reaching the T_d of 3.4 ms for *V1* and 11.4 ms for *V2* at the arteries' location according to the direction of pulse wave flow. While at the middle distance between the arteries, T_d approaches half of PTT_A of 7.5 ms because of the averaging effect of the tissue that leads to similar timing

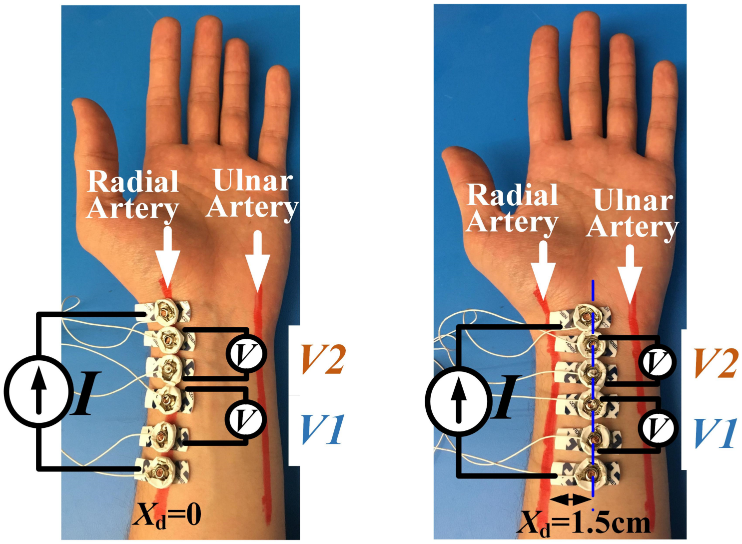

Figure 34. Pictures of electrode placement for validating the effect of sensing location on the PTT by dual channel Bio-Z measurements with sensing location X_d = 0 and 1.5 cm relative to the radial artery. Reprinted with permission from [3].

information for *V1* and *V2* as they go further from the arteries. Therefore, the maximum PTT is 8 ms at the arteries location and the minimum is 2.6 ms in the middle of the arteries.

Table 10: PTT and amplitude measurements with X_d = 0 and 1.5 cm. Reprinted with permission from [3].

	X_d	**Subj.**	**1**	**2**	**3**	**4**	**5**	**Mean**
PTT (ms)	**0**	**Mean**	8.0	3.0	6.8	8.2	7.9	6.8
		STD	3.8	2.7	1.8	3.0	4.3	3.1
	1.5	**Mean**	3.4	-2.6	11.1	5.6	-2.5	3.0
		STD	7.0	4.9	2.9	5.2	7.9	5.6
ΔV_{pp} (μV)	**0**	**Mean**	33.1	33.9	56	52.4	27.4	40.6
		STD	10.1	5.8	6.2	10.2	5.5	7.5
	1.5	**Mean**	26.3	19.9	32.6	26.1	22.3	25.4
		STD	7.5	2.9	3.0	5.7	4.5	4.7

This shows the importance of sensing location to be close to the artery to achieve the maximum sensitivity of PTT.

We compared the PTT results from the simulation model with the experimental measurements of PTT measured from a larger Bio-Z sensor to provide large signal amplitude away from the artery that allows the detection of the characteristic points to estimate PTT accurately. We used six wet electrodes with size 0.8×1.6 cm^2 with a spacing of 10 mm between every two electrodes for measuring *V1* and *V2* and estimate PTT from the time delay between the MS points. The electrodes were placed on the radial artery and between the radial and ulnar artery with the sensing distance from the artery is $X_d = 0$ and 1.5 cm, as shown in Figure 34. The data was collected from 5 subjects with 5 minutes per subject and ΔV_{pp} and PTT were calculated for the average across all heart beats, as shown in Table 10 which has the mean and standard deviation (STD) of the Bio-Z measurements for each subject. The measured subjects' mean PTT decreased from 6.8 to 3.0 ms and the mean ΔV_{PP} decreased from 40.6 to 25.4 μV when X_d increased from 0 to 1.5 cm, in line with the simulation results. The proposed model showed the detailed behavior and explanation of PTT variation with sensing location, which helps in improving the estimation algorithms of hemodynamic parameters.

3.5.5. Effect of the Current Frequency

We performed a Bio-Z frequency analysis by changing the frequency of the current injection from 3 to 25 kHz and monitoring the effect on V_{dc} and ΔV_{pp} in simulation and measurements with electrode configuration like the PTT experiment in Fig. 18 with electrodes placed over the radial artery. Figure 35 shows V_{dc} of the real and imaginary

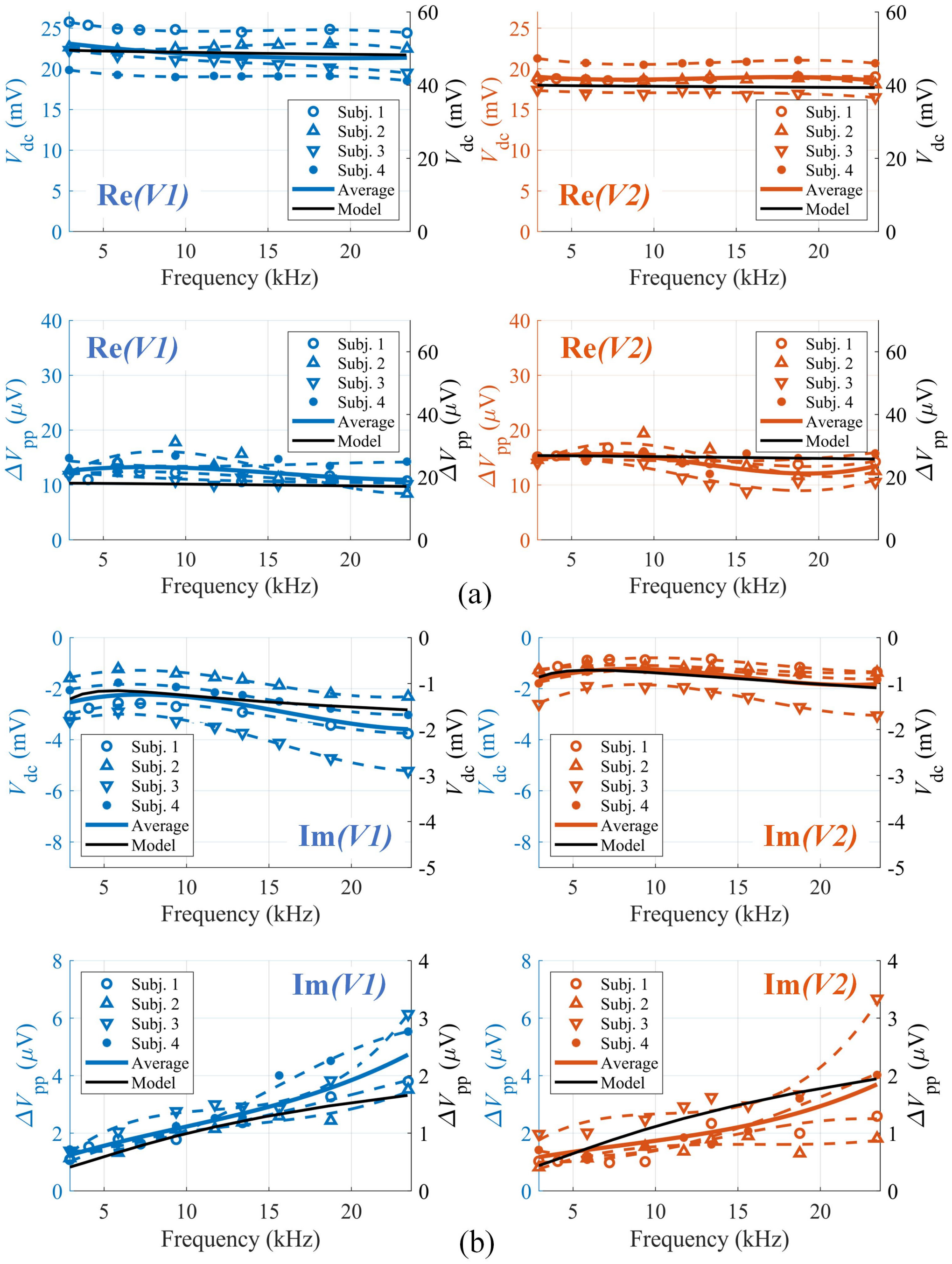

Figure 35. The measurement and model results of V_{dc} and ΔV_{pp} versus current injection frequency from 3 to 25 kHz for *V1* and *V2* (a) real part, (b) imaginary part. Reprinted with permission from [3].

components of *V1*(*i.e.* Re(*V1*)| and Im(*V1*)) and *V2* (*i.e.* Re(*V2*) and Im(*V2*)) versus frequency from 3 to 25 kHz. The measurements were done on 4 subjects by taking the average over 3 minutes of data collected at each frequency point at the radial artery. The measurements show that the V_{dc} and ΔV_{pp} of the real component are around 20 mV and 15 μV, respectively, which are much higher than the imaginary component with an average of 3 mV and 3 μV. There is a small change in the V_{dc} and ΔV_{pp} of the real component versus frequency. However, V_{dc} and ΔV_{pp} showed an increase with frequency for the imaginary component. As shown before, the V_{dc} is higher for *V1* while ΔV_{pp} is higher for *V2* which is closer to the hand because of the smaller depth of the artery. These trends of the measurement results were successfully captured by the model results showing the dominance of the real part compared to the imaginary part for both V_{dc} and ΔV_{pp}, which matches the components of the tissue impedance of fat, muscle, and blood.

3.5.6. Effect of the Electrode Size

One of the most important design parameters in Bio-Z sensing is the size of the current and voltage electrodes. For wearable applications, it is preferable to minimize the electrode size to achieve a small-form factor. However, a smaller electrode results in a higher skin-electrode impedance, thus decreasing the injected current and signal-to-noise ratio for a fixed voltage supply of the current source. To our knowledge, the effect of the electrode size on the pulse amplitude and accuracy has not been studied before. In this subsection, we present the effect of changing the electrode size (E_{X}) of the voltage and current electrodes from 0.85 to 4.25 cm on V_{dc} and ΔV_{pp} while using a fixed current amplitude to understand the effect of changing only the electrode size. The results of the proposed simulation platform are compared with the measurements from 3 subjects.

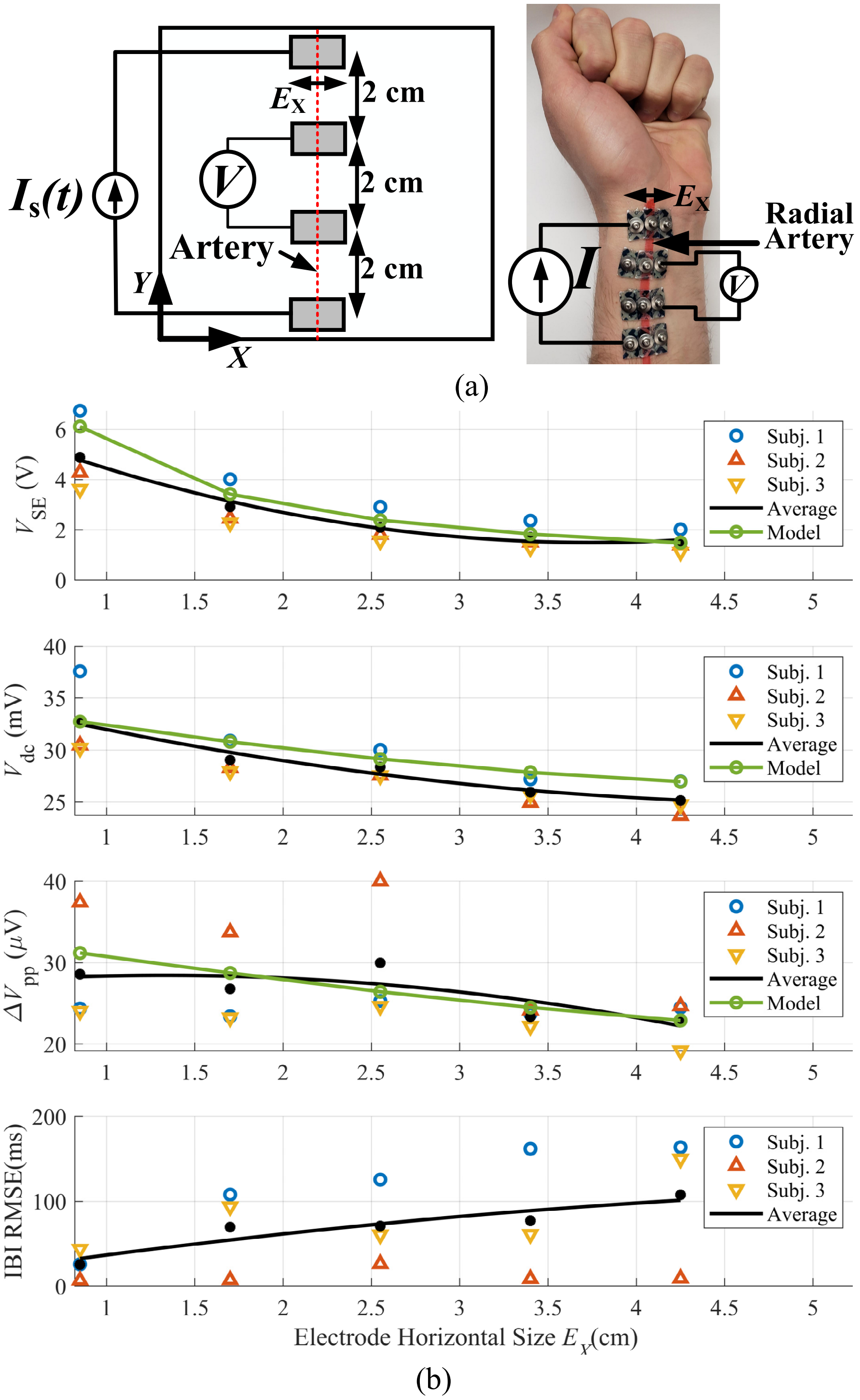

Figure 36. Comparison between the simulated and measured V_{dc} and ΔV_{pp} versus electrode horizontal size (E_X). Reprinted with permission from [3].

To change the electrode horizontal size (E_X), we used several small wet electrodes ($E_X = 0.85$ cm, $E_Y = 1.5$ cm) connected and stacked beside each other horizontally to provide variable E_X while keeping E_Y fixed, as shown in Figure 36(a). The vertical spacing between electrodes was 2 cm. We used up to 5 electrodes stacked beside each other to change E_X from 0.85 to 4.25 cm in 5 steps centered at the radial artery. We started by adding one central electrode on the radial artery followed by data collection for 3 minutes while the hand was resting on the bench. Then the data collection was repeated by adding one electrode at a time on each side of the central electrode. The magnitude of the skin-electrode impedance was monitored after attaching each new electrode. The skin-electrode impedance decreased consistently with increasing E_X, as shown in Figure 36(b). This was a verification step for the concept of stacking multiple electrodes beside each other to change E_X. Both simulations and measurements showed the decrease of average V_{dc} and ΔV_{pp} with increasing E_X, as shown in Figure 36(b). This is explained by the fact that Bio-Z is the measure of the impedance of a volume where its area is determined by the size of electrodes and its length is determined by the spacing between electrodes. Therefore, it is expected that V_{dc} will decrease as the electrode size increases due to a larger area of the measured volume. While ΔV_{pp} decreased with E_X because the measured Bio-Z can be considered as the parallel equivalent of variable impedance due to blood flow and fixed impedance from the tissue. As the E_X increases, the fixed impedance increases while the variable impedance remains the same because it is a function of the size of the artery. Therefore, the weight of the variable part and ΔV_{pp} decrease as the size of the electrode increases. In addition, the measured IBI RMSE relative to the reference PPG signal

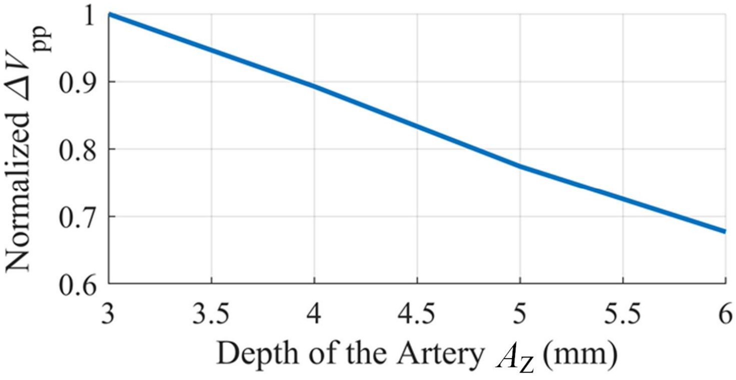

Figure 37. Simulation results of ΔV_{pp} versus artery's depth A_Z. Reprinted with permission from [3].

increases with E_X because of decreasing ΔV_{pp}. We can conclude from these results that it is better to decrease the size of the electrode to be focused on the artery and get a larger and more accurate amplitude of pulse signal with a lower IBI error.

3.5.7. Effect of the Artery's Depth

The artery's depth, A_Z, increases for individuals with high body mass index (BMI) because of a thicker fat layer under the skin. Increased A_Z results in lower pulse amplitude signal and lower quality of the estimations of the hemodynamic parameters. It is important to understand the effect of A_Z on the measured pulse signal to ensure reliable and robust sensing methods for all people with different BMI. However, it is difficult to characterize the effect of the artery's depth in the lab and having simulations tools such as the proposed simulation platform that can provide accurate and quick results is very useful. We used the proposed model to quantify the depth of penetration of the Bio-Z signal into the tissue to reach the artery. ΔV_{pp} at the surface was measured while changing the artery's depth A_Z from the average depth of 3 to 6 mm. The simulation results showed that the normalized ΔV_{pp} decreased by only 32% when the artery's depth was doubled, as shown in Figure 37.

This demonstrates that Bio-Z is also suitable to detect pressure pulse waveform and hemodynamic parameters for individuals with high BMI.

3.6. Conclusions

In this chapter, we proposed a Bio-Z simulation platform using a 3D grid of the time-varying impedance voxels to model the tissue and pulse wave in the arteries by simulations in the SPICE environment in parallel with the sensing circuits. The proposed methods modeled the propagation of current through the small elements in the grid and the distribution of voltage at each node including the DC voltage of tissue and pulse signal from blood flow. The model was validated against Bio-Z measurements for the effect of different electrode locations relative to the artery, current frequency injection, and electrode size on the sensed pulse signal. The proposed method was used to quantify the penetration of the bio-impedance signals inside the tissue for different arterial depths. The proposed simulation platform can serve as an important tool to understand the propagation of pulse wave in the tissue and to improve Bio-Z sensing methods for measuring hemodynamic parameters and guide circuit designers and algorithm developers.

4. CUFFLESS BLOOD PRESSURE MONITORING FROM AN ARRAY OF WRIST BIO-IMPEDANCE SENSORS USING SUBJECT-SPECIFIC REGRESSION MODELS: PROOF OF CONCEPT[3]

4.1. Overview

Continuous and beat-to-beat monitoring of blood pressure (BP), compared to office-based BP measurement, provides significant advantages in predicting future cardiovascular disease. Traditional BP measurement methods are based on a cuff, which is bulky, obtrusive and not applicable to continuous monitoring. Measurement of pulse transit time (PTT) is one of the prominent cuffless methods for continuous BP monitoring. PTT is the time taken by the pressure pulse to travel between two points in an arterial vessel, which is correlated with the BP. In this chapter, we present a new cuffless BP method using an array of wrist-worn bio-impedance sensors placed on the radial and the ulnar arteries of the wrist to monitor the arterial pressure pulse from the blood volume changes at each sensor site. BP is accurately estimated by using AdaBoost regression model based on selected arterial pressure pulse features such as transit time, amplitude and slope of the pressure pulse, which are dependent on the cardiac activity and the vascular properties of the wrist arteries. A separate model is developed for each subject based on calibration data to capture the individual variations of BP parameters. In this

---

[3] Part of this chapter is reprinted with permission from "Cuffless Blood Pressure Monitoring from an Array of Wrist Bio-impedance Sensors using Subject-Specific Regression Models: Proof of Concept," by B. Ibrahim and R. Jafari, 2019. *IEEE transactions on biomedical circuits and systems,* vol. 13, no. 6, pp. 1723-1735, 2019, Copyright 2019 by IEEE.

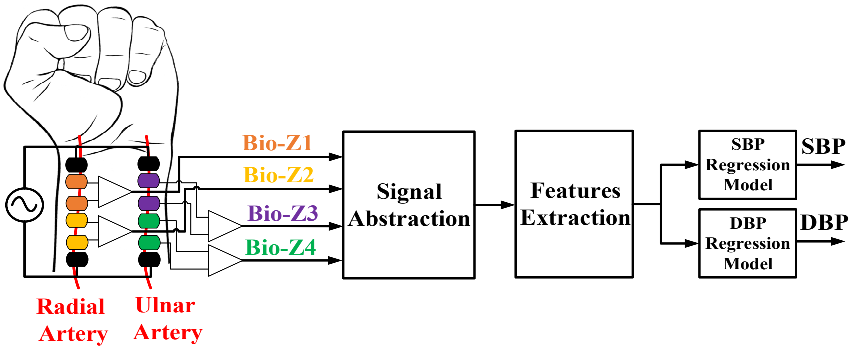

Figure 38. The block diagram of the BP estimation hardware and signal processing from wrist-worn bio-impedance sensors array. Reprinted with permission from [1].

pilot study, data was collected from 10 healthy participants with age ranges from 18 to 30 years after exercising using our custom low-noise bio-impedance sensing hardware. Post-exercise BP was accurately estimated with an average correlation coefficient and root mean square error (RMSE) of 0.77 and 2.6 mmHg for the diastolic BP and 0.86 and 3.4 mmHg for the systolic BP.

4.2. Introduction

Our approach is based on placing an array of sensors on the wrist arteries, which provide local measurements of the cardiac activity of both the radial and ulnar arteries for accurate estimation of the PTT and consequently the BP [21]. In this chapter, we use a model for the vascular properties of the radial and ulnar arteries of the wrist to estimate the systolic and diastolic BP by a regression model based on PTT and other features extracted from an array of 2×2 of bio-impedance sensors placed on the wrist arteries as shown in Figure 38. A pair of bio-impedance sensors are placed on each of the radial and ulnar arteries to measure the local blood volume changes of the arteries to estimate the local PTT of each artery for accurate BP measurements. A model is generated for each user to characterize the unique vascular properties of the wrist arteries, which vary from person to person. We use bio-impedance sensing because it is a non-invasive electrical signal that can measure local blood volume changes in the arteries using small metal electrodes placed on the skin. Bio-impedance sensors are low cost and low power, which can be easily used for a large array of sensors in a wearable device. In addition, configurable sensing areas can be realized by controlling the location of the current injection and voltage sensing electrodes.

The contributions of this chapter can be summarized as follows:

- A new cuffless BP method using an array of bio-impedance sensors placed on the radial and ulnar arteries of the wrist, which can be integrated into a wrist-worn device..
- High-resolution bio-impedance sensing circuits and signal processing with root mean square error (RMSE) less than 1 mΩ for accurate measurements of the local arterial pressure pulse in the wrist arteries.
- Accurate systolic and diastolic BP estimation by abstracting the pressure pulse with six characteristic points which are used for feature extraction based on the amplitude and slope of the pulse of each sensor and the transit time between each pair of sensors.
- In this pilot study, we evaluate the performance of our methods on 10 human subjects for post-exercise blood pressure changes.

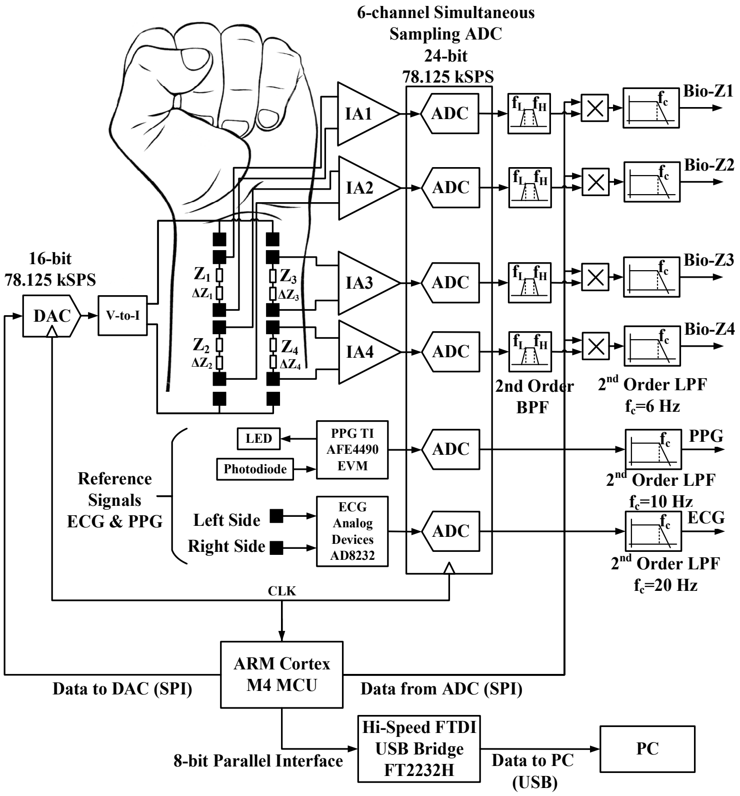

Figure 39. The block diagram of the bio-impedance sensing hardware. Reprinted with permission from [1].

This chapter is organized into five sections. After the introduction, our methods are discussed in section 4.3, and the data collection procedures are shown in section4.4. The results are presented in section 4.44.5, and the limitations of this work are discussed in section 4.6. Finally, conclusions are presented in section 4.7.

4.3. Methods

4.3.1. Bio-impedance Sensing Hardware

In order to measure PTT over wrist arteries, a pair of Bio-Z sensors are placed on the wrist along the radial artery (Bio-Z1 & Bio-Z2) and another pair were placed along the ulnar artery (Bio-Z3 & Bio-Z4). Each pair of sensors shares the current injection electrodes to place all the electrodes in a small area suitable for a small form factor wrist watch. Small size pre-gelled Ag/AgCl electrodes with dimensions 0.8cm×1.5cm are used to provide contact with the skin for current injection and voltage sensing. The spacing between the sensing electrodes is 0.8cm and all other electrodes are placed as close as possible. The electrodes are connected to the Bio-Z sensing hardware as shown in Figure 39.

4.3.2. Blood Pressure Estimation Algorithms

The BP estimation algorithms consist of signal abstraction of each Bio-Z signal with its characteristic points followed by feature extraction, and finally systolic BP (SBP) and diastolic BP (DBP) estimation using AdaBoost regression models.

4.3.2.1. Signal Abstraction

The wrist Bio-Z signal variations due to blood volume changes in the arteries are abstracted by four characteristic points for every heart beat after removing the Bio-Z DC offset. At every heart beat, the Bio-Z signal descends from the first main peak to the first notch, which indicates a sudden increase in the blood volume due to the arrival of the pressure pulse to the sensing location. The Bio-Z peak point represents the diastolic phase while the notch point represents the systolic phase of the pressure pulse. In addition, the back reflection of the pressure pulse due to higher vascular resistance causes the second smaller peak and notch in the middle of the cardiac cycle. In order to detect both DBP and SBP, we use four characteristic points from all phases of the cardiac pulse of Bio-Z signal, which are the diastolic peak, maximum slope, systolic foot and the inflection point as shown in Figure 40. The diastolic peak (DIA) and the systolic foot (SYS) are detected by

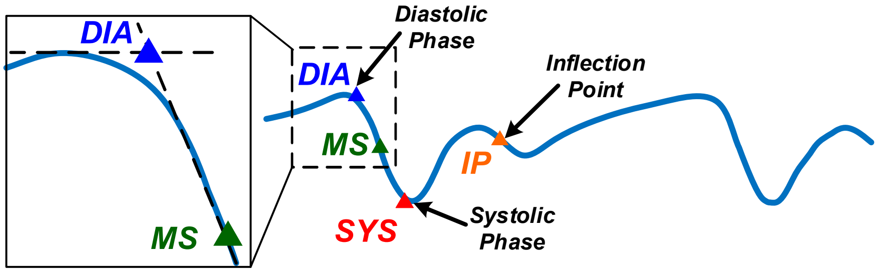

Figure 40. The Bio-Z signal marked with four different points selected for Bio-Z signal abstraction, which are diastolic peak (DIA), maximum slope (MS), systolic foot (SYS) and inflection point (IP). Reprinted with permission from [1].

the intersection of the tangent to the slope with the horizontal line from the maximum and the minimum of the signal, respectively. This method provides accurate measurement of the diastolic and systolic points because it is immune to noise that may occur at the peak or the foot of the signal [61]. The maximum slope (MS) point is also an important point in the middle of the descending slope section. The fourth point is the inflection point (IP), which is the maximum slope point between the second peak and notch. All these points are identified from the first and the second derivative of the Bio-Z signal using the zero crossing, peak and foot points. The amplitude and time values of these points are used for extracting the BP features.

4.3.2.2. Features Extraction

The features extracted from the measured pulse waveforms are highly correlated with BP. When the heart pumps blood to the rest of the body, the velocity of the pressure pulse, which propagates through the arteries, is highly correlated with the elastic properties of arteries, similar to a pipe with elastic walls according to Moens–Korteweg (M–K) equation [8]:

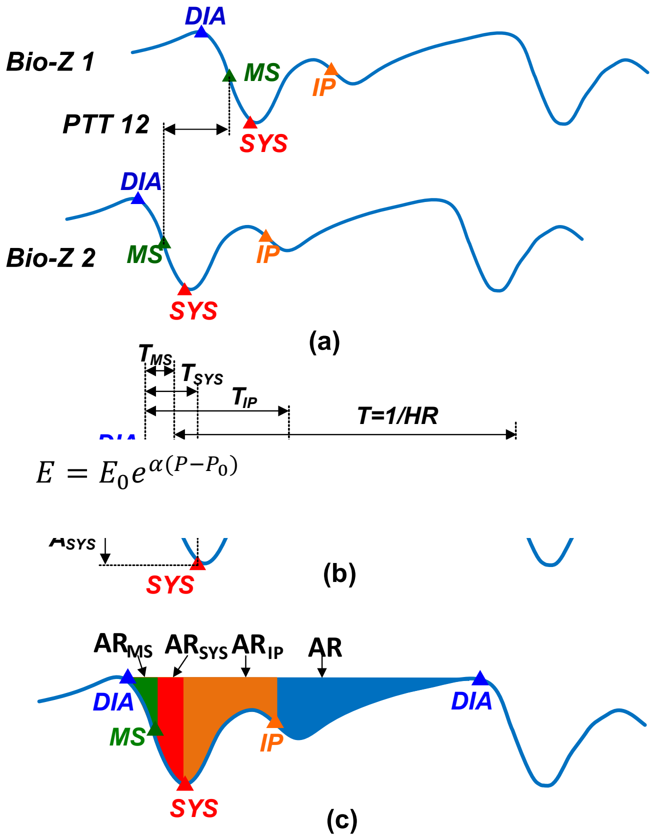

Figure 41. (a) The PTT features measured between a pair of Bio-Z signals at all the characteristic points, (b) The time and amplitude features measured for a single Bio-Z signal from PK to the rest of points., (c) The time and amplitude features measured for a single Bio-Z signal from PK to the rest of points. Reprinted with permission from [1].

$$E = E_0 e^{\alpha(P-P_0)} \tag{4.2}$$

$$PWV = \sqrt{\frac{E.h}{2R\rho}} \tag{4.1}$$

where PWV is the pulse wave velocity, E is Young's modulus, which is related to the vessels elasticity, h is the vessel thickness, R is the inner radius of vessels and ρ represents the blood density. For an elastic vessel, the relation between the blood pressure and E is given by [62] as follows:

where E_0 and P_0 are constants, P represents the blood pressure in arteries and α is a correction factor. PWV can be measured by dividing PTT by the distance between two sensing sites on an artery. Therefore, PTT was selected as one of our main features of BP, which is proportional to $1/\mathrm{PTT}^2$. Additional features were also selected to improve correlation with BP such as the ratio between the amplitudes of systolic foot and inflection point relative to the diastolic peak, which is a measure of the intensity of the reflection wave. In addition, the time interval between the systolic foot and the inflection point measures the arterial stiffness, while the area under the curve represents the total peripheral resistance [63]. All these features are useful in modeling the vascular properties of arteries and we use them in building the regression model for BP.

The four characteristic points of the four Bio-Z signals are used to generate 50 features for each heart beat that can accurately model the vascular properties of the two arteries of the wrist. The features can be categorized into four sets, which are PTT, time, amplitude and area as shown in Table 11. The PTT features are calculated from each pair of signals, while the rest of the features are calculated from each signal individually. These features are related to the cardiac output and arterial stiffness of each wrist artery which can be used for accurate estimation of BP. Window-based features are proposed in this work in order to reduce the effect of feature variations from beat to beat due to noise or other physiological activities that are uncorrelated to BP such as respiration rate. The window-based features are calculated by taking the average of the beat-by-beat features

Table 11: Wrist Bio-Z features. Reprinted with permission from [1].

Feature Set	Feature Description	Number of Features
PTT	The time delay between each pair of Bio-Z signals measured at MS point as shown in Figure 41(a).	6
Time	The inter-beat interval (T) and the time interval from the DIA point to the rest of points, which are T_{MS}, T_{SYS} and T_{IP} as shown in Figure 41(b).	16
Amplitude	These are the difference in amplitude from DIA point to the rest of points, which are A_{MS}, A_{SYS} and A_{IP} as shown in Figure 41(b).	12
Area	The areas under the Bio-Z curve starting from the DIA point to the rest of points, which are AR_{MS}, AR_{SYS}, AR_{IP} and AR as shown in Figure 41(c).	16

over 10 beats with 50% overlap. We assume BP to be constant during each window which is equivalent to an average of 8 seconds of time, which is a realistic expectation.

4.3.2.3. BP Regression Model

Finally, DBP and SBP are estimated using advanced regression models trained by the Bio-Z features extracted from the wrist and BP data measured simultaneously by a reference continuous BP monitoring device. Although BP varies from one location to another over an artery, they are correlated with each other. Our method provides brachial BP measurements from features extracted from the wrist pulse signals by training the regression models using brachial BP data. Separate models are used for DBP and SBP estimation because DBP and SBP rely on different features. The models are trained for each user in order to capture the individual variations of their vascular properties for more accurate BP estimation.

Our subject-specific models are trained using a limited number of training window samples for each subject, which require careful selection of model hyper-parameters to avoid overfitting. We use the Adaptive Boosting (AdaBoost) regression model, which establishes a prediction by combining the outputs of a number of weak learners through a weighted sum of different subsets of the training data set. AdaBoost is an ensemble learner that reduces overfitting by decreasing the variance between the different training data subsets. The dataset of each subject is shuffled and divided into 10 folds to get 80% of the data for training the models, 10% for selecting the hyper-parameters, and 10% for testing. The AdaBoost models consist of 50 decision trees with tree depth is selected from the range of 4 to 14. For each model, the tree depth with the minimum testing error is selected to provide the best model complexity that avoids overfitting and underfitting. The performance of the models is evaluated using the average across all the 10 folds of the root mean square error (RMSE), mean absolute error (MAE) and correlation coefficient (R).

4.4. Data Collection

The performance of our method was evaluated using Bio-Z and BP data collected simultaneously from human subjects during exercising to produce a change in BP. Four Bio-Z signals were measured from the wrist using our hardware. The electrodes were placed on the radial and the ulnar arteries, as shown in Figure 42, after detecting the

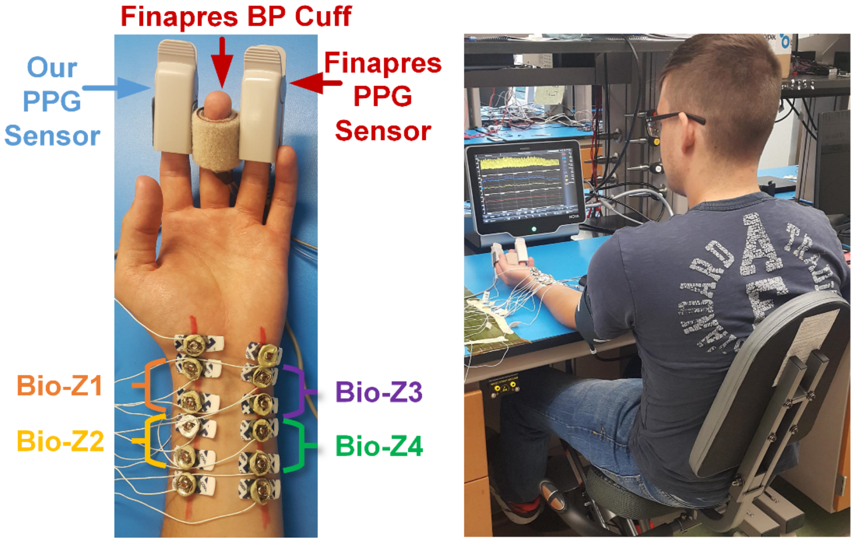

Figure 42. Pictures showing the placement of electrodes and sensors on the wrist and fingers (left) and the experimental setup for BP monitoring (right). Reprinted with permission from [1].

location of the arteries using the Huntleigh Dopplex MD2 Bi-Directional Doppler, which can measure arterial blood flow with a high sensitivity probe with a diameter of 20 mm. For the Bio-Z current injection frequency, we used the highest possible frequency supported by our measurement system, which is 9.75 kHz. At higher current injection frequency, the cell membrane impedance gets smaller, more current can flow inside the cells and the electrode exhibits a lower impedance with the skin, which results in better sensing of blood volume changes from the Bio-Z signal. The current amplitude was adjusted to 800μA in order to be compliant with the safety standards [30]. For the validation of Bio-Z measurements, ECG signals from the chest and PPG signals from the finger were measured simultaneously with the Bio-Z signals. The ECG was measured by the SparkFun single lead Heart Rate Monitor board, which is based on the AD8232 analog front end developed by Analog Devices. The leads were attached to Covidien pre-gelled ECG patches and placed on the chest to provide a single channel of ECG. The PPG was measured using the AFE4490 EVM by Texas Instruments. The sensor itself is a finger-clip based transmitting type PPG device. The ECG analog output and the PPG photodiode output were directly routed to two channels of our own ADC just like the Bio-Z channels to maintain accurate time synchronization between all of them.

In order to monitor SBP and DBP at every heart beat simultaneously with Bio-Z, continuous BP was measured using the non-invasive reference device Finapres NOVA system. This system measures BP continuously using a finger pressure cuff placed on the middle finger, which was calibrated by the standard brachial pressure cuff. Finapres system was cleared from the U.S. Food and Drug Administration (FDA) for measuring BP in 2017 [64] and is also widely used in literature as a reference device for continuous BP measurements [5, 17, 65-67]. In order to synchronize the heart beats of the Bio-Z signal acquired by our setup with the continuous BP signal measured from Finapres device, an additional PPG signal was monitored by the Finapres device using a PPG finger clip. Both PPG signals measured by our setup and Finapres were synchronized together using a matched filter dependent on matching the unique pattern of inter-beat-intervals.

Data was collected from ten healthy human subjects (seven males and three females) with age ranges from 18 to 30 years in this pilot study under the IRB approval IRB2017-0086D by Texas A&M University, and each participant was seated on a bike with his arm rested on the bench. Initially, 3 minutes of data were collected at rest. Then, the participant exercised for 5 minutes through cycling on the bike to raise the BP followed by 4 minutes of data collection to capture the recovery of BP to its normal value. This was

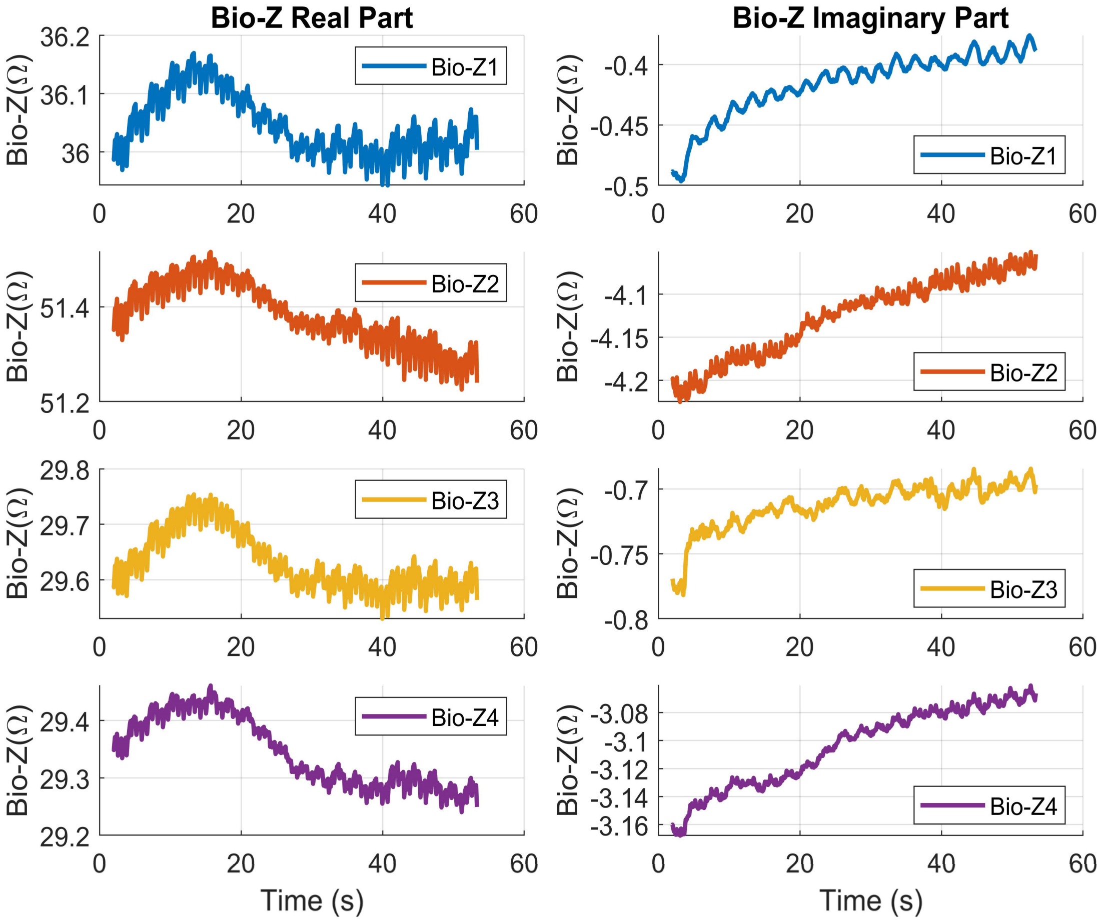

Figure 43. An example of the real and imaginary parts of the Bio-Z signals for the four sensors. Reprinted with permission from [1].

repeated 5 times to increase the number of samples collected per subject to be able to train a model for each subject. Finally, another 3 minutes of data were collected at rest.

4.5. Results

4.5.1. BP and Wrist Bio-impedance Data

The proposed Bio-Z measurement method relies on synchronous demodulation, in order to monitor both the real and imaginary parts (or magnitude and phase) of the Bio-Z signal which provides complementary information about the tissue and blood flow. Figure

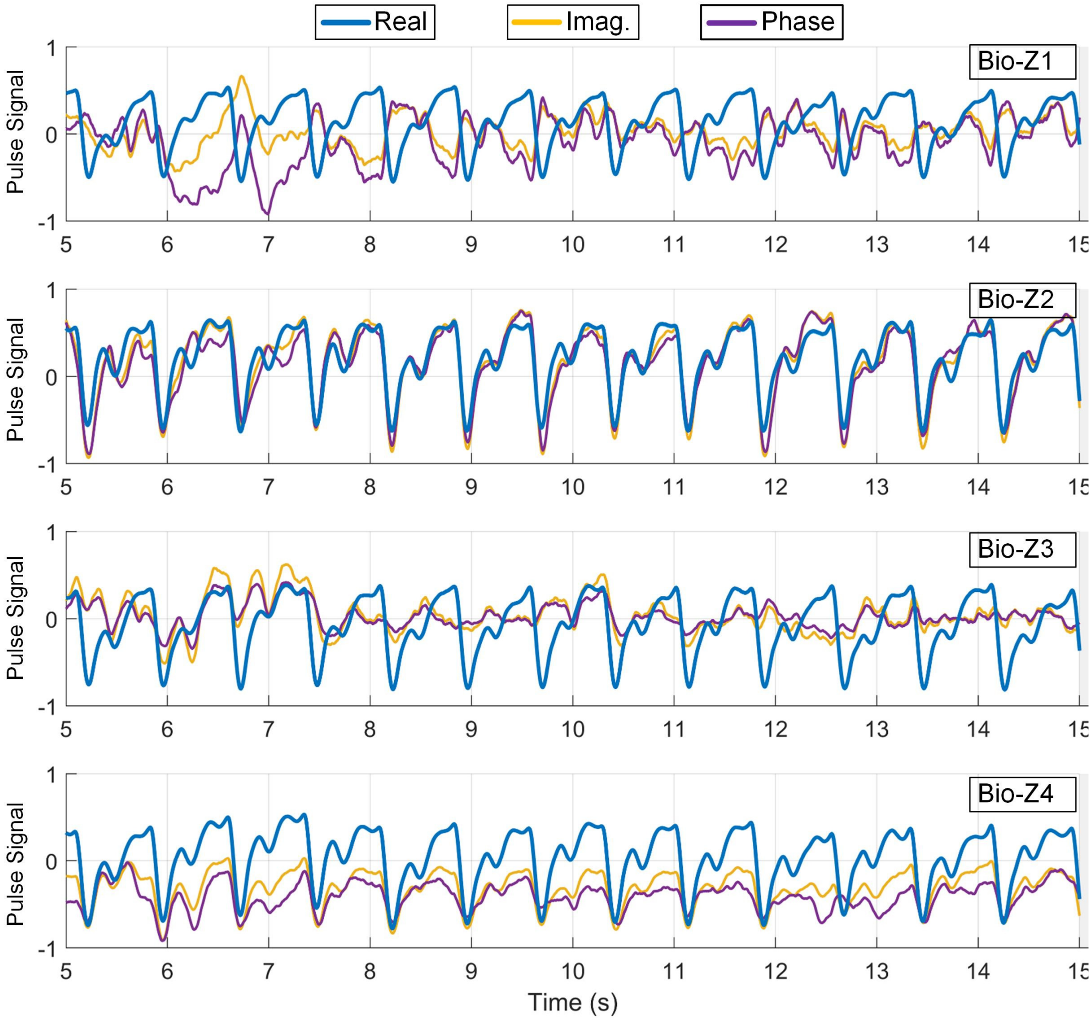

Figure 44. An example of the heart pulse signals extracted from the real, imaginary and phase parts of ΔBio-Z for the four Bio-Z sensors. The real part has the most consistent pulse signal. Reprinted with permission from [1].

43 shows an example of the real and imaginary parts of the four Bio-Z channels. Each Bio-Z signal consists of a DC offset which represents the tissue impedance in addition to variations due to heart signal rate. The DC component of the real part of wrist Bio-Z at 9.75 kHz varies from 29 to 51 Ω, which is significantly higher than the imaginary component that varies from 0.4 to 4 Ω depending on the Bio-Z sensor location. The DC

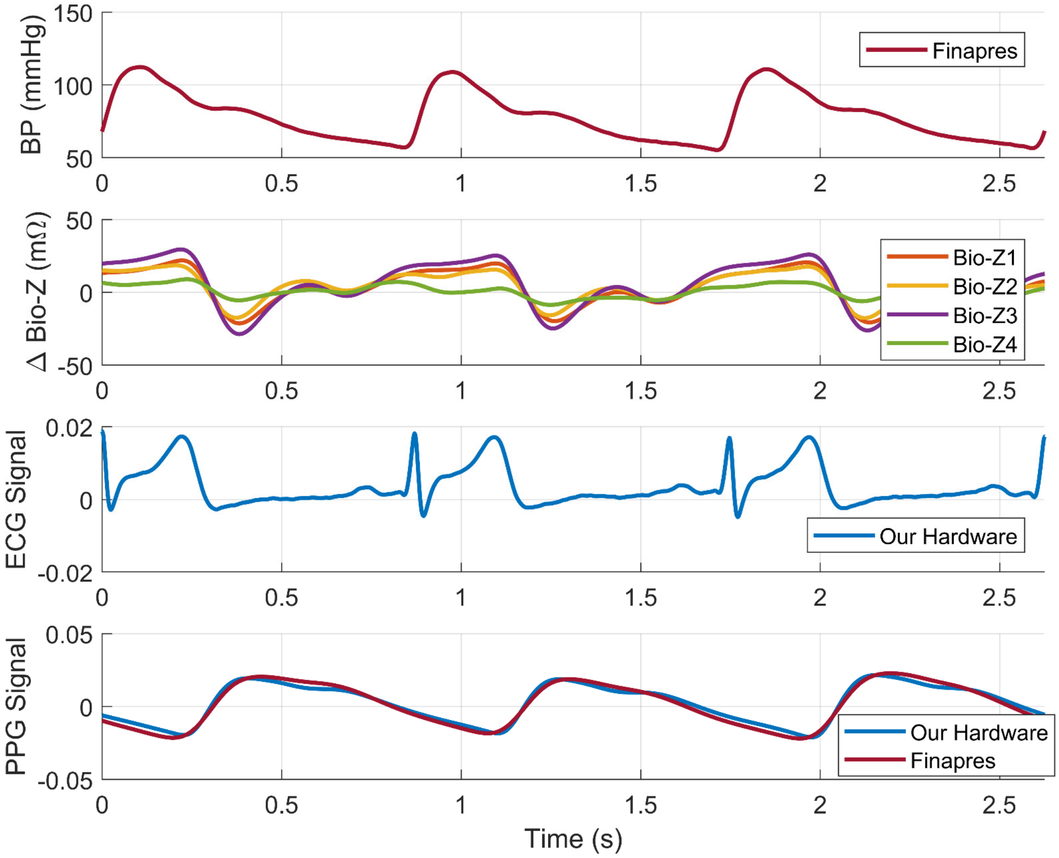

Figure 45. An example of continuous BP signal measured from the Finapres device and bio-impedance variations measured from our four sensors placed on the radial and ulnar arteries of the wrist. Simultaneous ECG signal measured from the chest and PPG signal measured from the finger were shown for validation. Reprinted with permission from [1].

offset varies slowly due to slight movements of the wrist. This slow variation of the DC offset is consistent across all sensors because they are placed within a small area on the wrist and affected by the same pattern of wrist movements. There are different trends in the real part compared to the imaginary part, because the real part measures the resistance of the intra- and extra- cellular fluids, while the imaginary part measures the capacitance of the cell membrane.

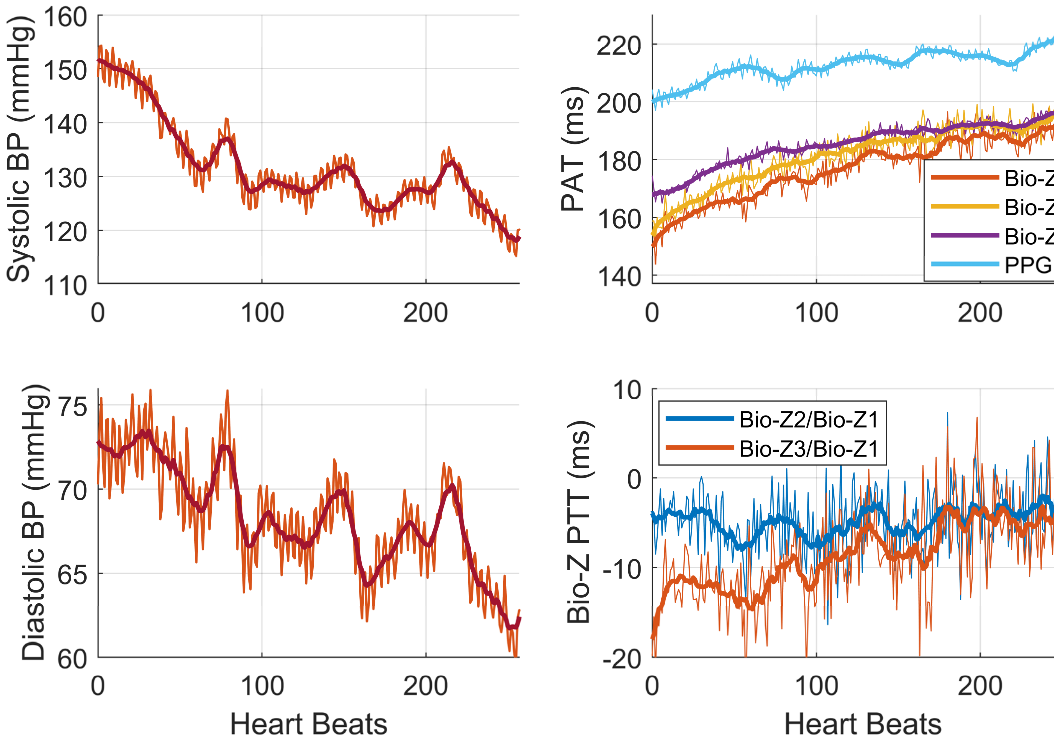

Figure 46. The heartbeat-based and window-based BP and Bio-Z features after exercise for subject 1. Reprinted with permission from [1].

We compared the heart pulse signal of the different parts of the Bio-Z signal (real, imaginary, magnitude and phase) for the four Bio-Z sensors after removing the DC offset and respiration rate by a high pass filter as shown in Figure 44. The real and magnitude of Bio-Z are almost equivalent because the real part is much larger than the imaginary part. Also, the pulse signal exhibits higher consistency in the real part compared to the imaginary and phase representations. Therefore, we used the pulse signal from the real part of Bio-Z for the proposed BP models.

An example of the physiological signals as measured by our circuits and Finapres after filtering and pre-processing are shown in Figure 45. The figure plots the Bio-Z variations (ΔBio-Z) versus time for the 4 sensors placed on the wrist arteries with an amplitude varying from ±10 mΩ to ±25mΩ after removing the DC offset. ΔBio-Z clearly shows the arrival time of the pressure pulse at the wrist arteries every heart beat which is the time when ΔBio-Z drops suddenly from the peak to the foot. Our measured ΔBio-Z signals in time domain show a significant difference in amplitude and timing between the four sensors placed on the wrist, which implies that vascular properties vary with location and from an artery to another. In addition, Figure 45 shows the cardiac cycle that starts with the R-peak of the ECG signal followed by the rise in the BP from the DBP to SBP, and then the Bio-Z and PPG signals show the arrival of the pressure pulse at the wrist and the finger respectively. The reflections inside the arteries are shown by the smaller peaks that occur before the next heart beat.

Figure 46 shows an example of the beat-to-beat SBP and DBP of subject 1 for short period of 1.3 minutes (260 heart beats) after exercising simultaneously with the measured PTT in addition to the pressure pulse arrival time (PAT) which is the time from the R-peak of the ECG to the maximum slope point of the Bio-Z or PPG signals. The SBP and DBP decrease with heart beats from the elevated SBP and DBP of 150 and 75 mmHg respectively to the normal BP of 120 and 60 mmHg. In addition, the figure illustrates PAT at wrist and finger as they increase continuously when BP decreases with high correlation as expected. The PAT measured at the finger from the PPG sensor is higher than the PAT measured at the wrist from the Bio-Z sensors with around 30 ms. This shows that Bio-Z sensors at the wrist capture the arterial pulse signal that arrives at the wrist first then move to the finger following the blood flow direction in the arteries from the heart to the finger.

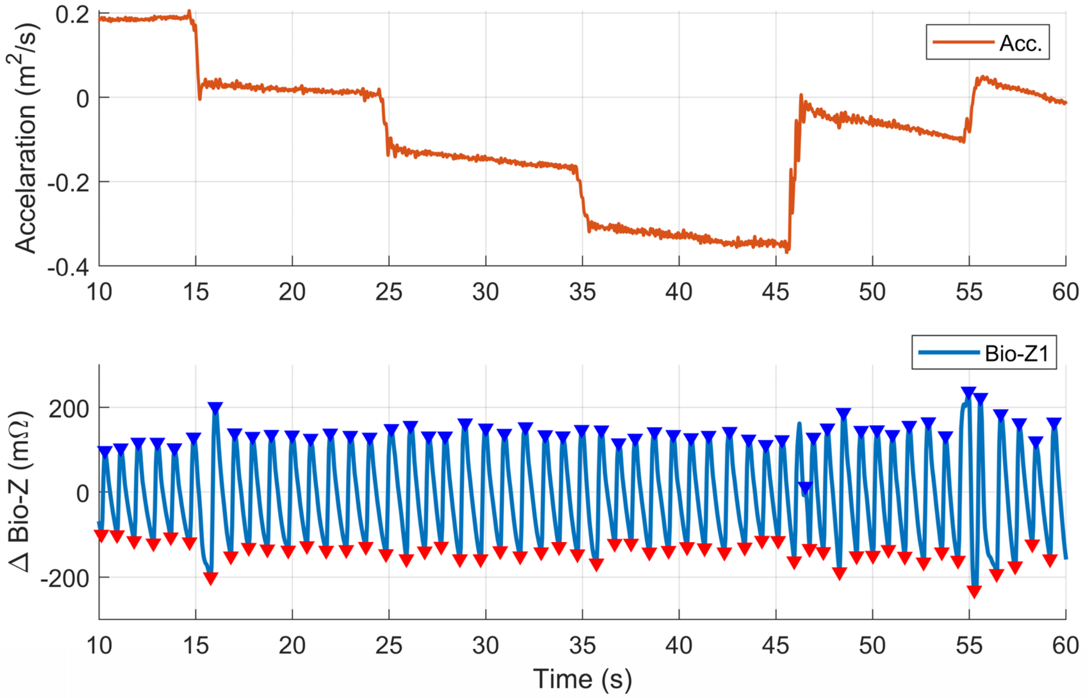

Figure 47. An example of the clean pulse signal as measured from the ΔBio-Z signal in presence of small wrist movements that was captured by the acceleration change from a motion sensor placed on the wrist. Reprinted with permission from [1].

Furthermore, the variation of beat-to-beat PTT due to BP change is shown in this figure. The PTT between different Bio-Z channels exhibit different behavior, therefore it is useful to account for PTT between all Bio-Z channels for more accurate BP estimation. The BP, PAT, and PTT show large variations from beat to beat due to physiological effects such as respiration rate. Therefore, the proposed window-based features act as a filter to remove these variations as shown by the solid lines in this figure, which leads to more accurate BP estimation compared to the beat-to-beat features. The measured PTT from the wrist is less than 30 ms and negative for some trials as shown in this figure because blood may move in the opposite direction for small distances near the wrist as a result of the reflection of the pressure pulse from the termination of the wrist arteries in the hand in addition to the slope variations between the measured Bio-Z signals due to different vascular properties [24].

Motion artifacts especially due to wrist movements can cause signal corruption to the Bio-Z signals measured from the wrist sensors. Although the participants placed their wrist in resting position on the bench during the data collection, small wrist movements can cause Bio-Z signal corruption for few heart beats. We conducted a number of experiments for the characterization of the effect of small wrist movements on the measured Bio-Z signals. A motion sensor was placed on the wrist to measure the wrist movements simultaneously with the measured Bio-Z signals. The participants were asked to place their wrist on the bench in resting position then moved it by 5 cm horizontally every 10 seconds. Figure 47 shows an example for the acceleration measured by the motion sensor and the Bio-Z signal measured from the sensor Bio-Z1 for 50 seconds during the wrist movements. The Bio-Z signal shows clear pulse waveform during the applied wrist movements with some noise in the waveform in few heart beats. This results show that Bio-Z signal can be reliably acquired during small movements of the wrist in our experiment.

We collected a total of 13,050 samples of beat-to-beat BP and Bio-Z features which are equivalent to of 2,848 sample windows from all subjects after removing noisy samples which are the samples corrupted by motion artifacts. We removed the corrupted heart beats with large PTT variance higher than a certain threshold based on the small distance between the sensors. These noisy samples were removed to ensure proper training

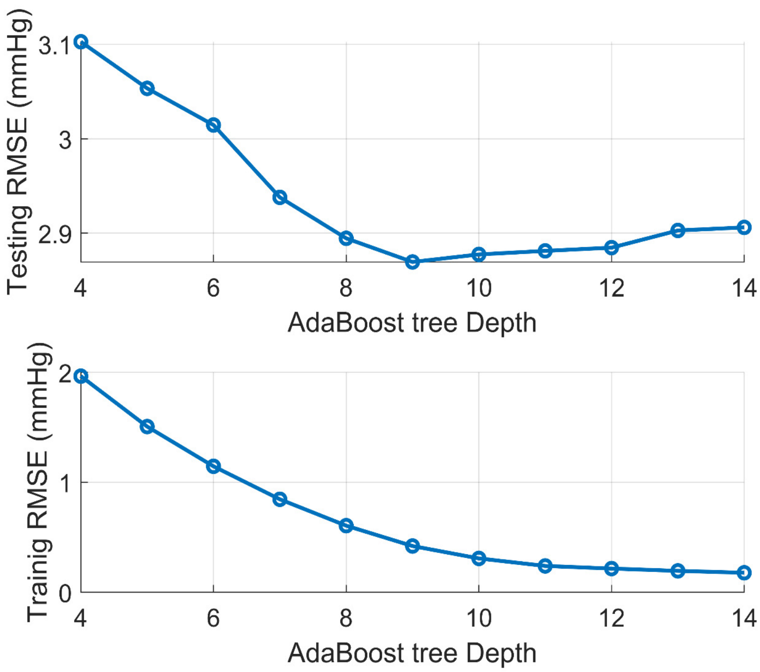

Figure 49. Example of the variation of testing and training error with changing the AdaBoost tree depth. The best model fitting occurs at the minimum testing error wat tree depth=9. Reprinted with permission from [1].

of our models and accurate BP predictions. The measured DBP ranges from 50 to 100 mmHg and SBP ranges from 90 to 160 mmHg according to the histogram in Figure 48.

4.5.2. BP Estimation Error

The collected BP and Bio-Z features were used for training and testing the AdaBoost regression models for DBP and SBP for each subject. The best tree depth was selected for each model at the minimum testing error to avoid over or under fitting. Figure 49 shows an example of the behavior of the testing and training RMSE with the variation of the AdaBoost tree depth from 4 to 14. The training error decreases monotonically with increasing the tree depth, while the testing error had a minimum at tree depth of 9, which is the best choice for the model complexity for best fitting.

Table 12: DBP and SBP estimation performance for each subject using AdaBoost Model. Reprinted with permission from [1].

Subject	DBP		SBP	
	R	**RMSE (mmHg)**	**R**	**RMSE (mmHg)**
1	0.86	2.25	0.86	2.86
2	0.83	3.29	0.92	3.84
3	0.78	2.01	0.91	2.54
4	0.83	2.46	0.92	2.5
5	0.79	3.69	0.89	4.78
6	0.59	3.25	0.81	4.64
7	0.77	2.67	0.83	3.93
8	0.76	2.38	0.82	3.37
9	0.7	2.16	0.77	2.69
10	0.83	2.18	0.85	3.22
Average	0.77±0.08	2.63±0.58	0.86±0.05	3.44±0.84

The performance of the DBP and SBP regression models is evaluated by taking the average of the correlation coefficient and RMSE of all the subjects as shown in Table 12. Our regression models show excellent performance for BP estimation with average correlation coefficient and RMSE of 0.77 and 2.63 mmHg for the DBP and 0.86 and 3.44 mmHg for the SBP, respectively. The achieved performance from the AdaBoost regression model is much better than the maximum correlation coefficients of the individual features with BP, which is 0.16 and 0.22 for the area under the curve from DIA to IP points of Bio-Z2 with DBP and SBP respectively.

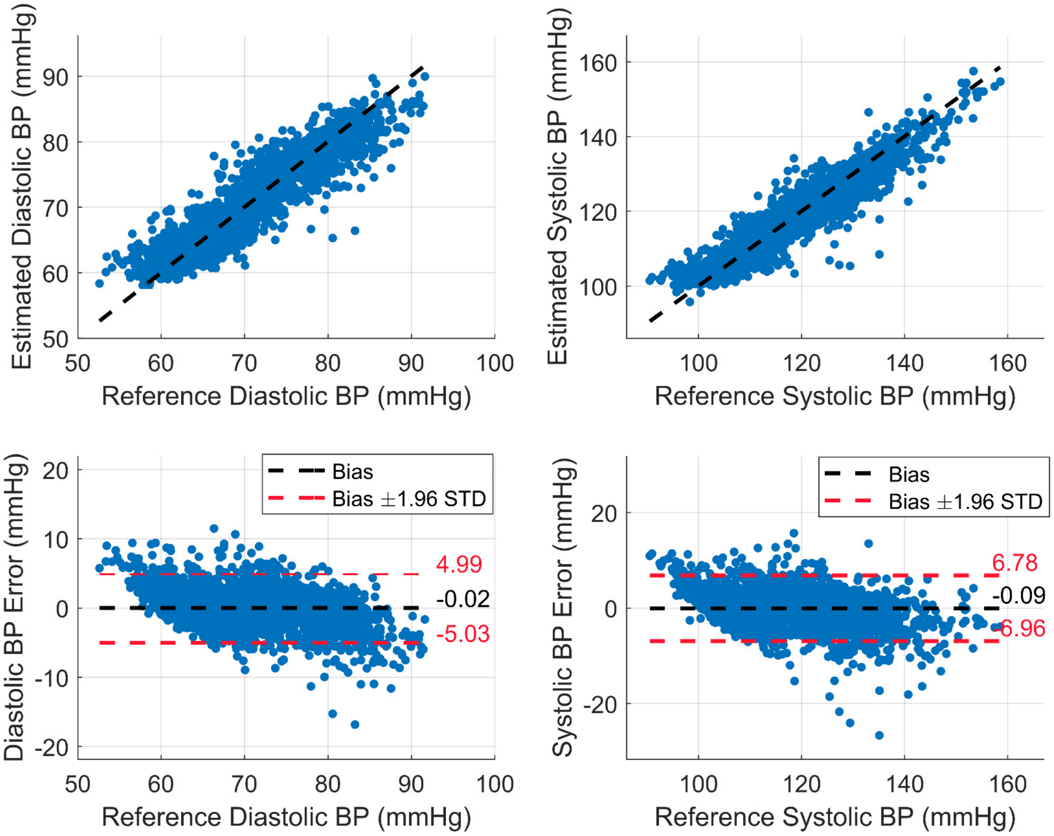

Figure 50. The estimated DBP and SBP and the error for all the subjects using AdaBoost model using the window-based features. Reprinted with permission from [1].

The AdaBoost models are able to capture more complicated functions between these features to model BP effectively. In Figure 50, we present the estimated SBP and DBP and the BP error for all BP samples from all subjects. Figure 51. shows the long-term variation of SBP and DBP due to multiple exercising sessions by showing 15 minutes of data from subject 3 collected over 50 minutes by the concatenation of initial rest data, three post-exercise data trials (1,2 and 4) and final rest data after removing noisy data. The estimated SBP and DBP track the reference changes over wide BP range (from 110 to 150

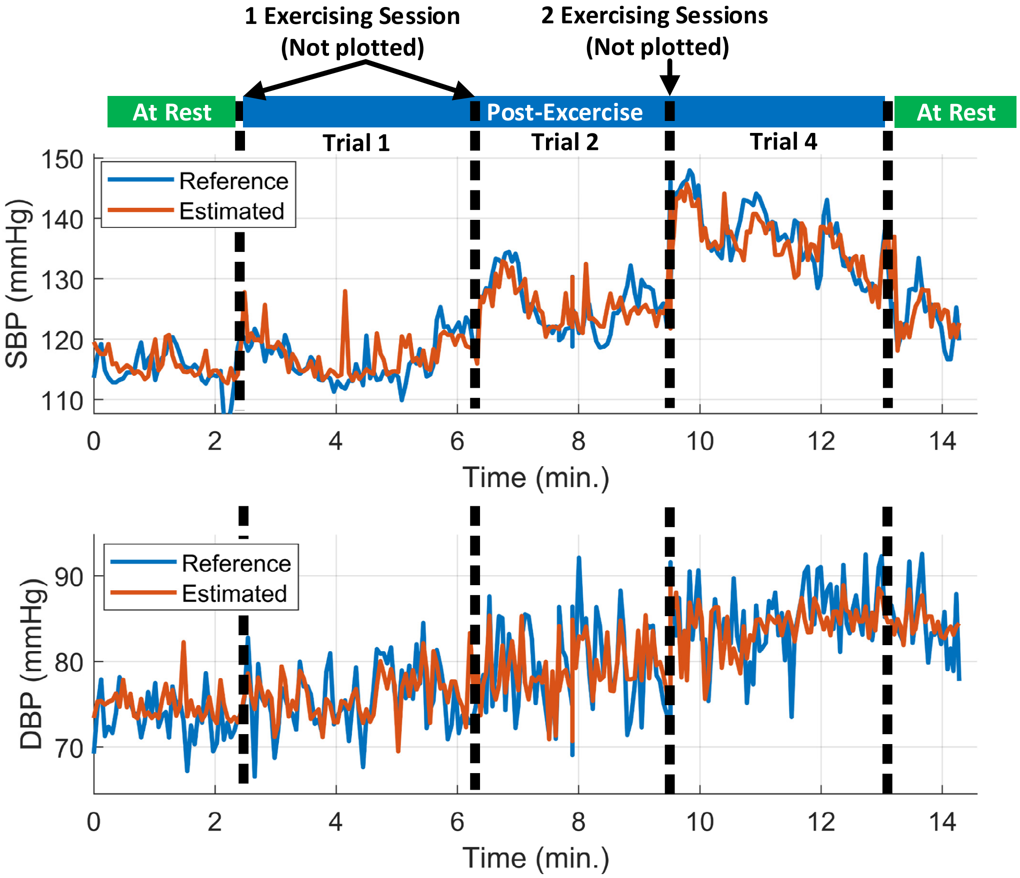

Figure 51. The estimated and reference SBP and DBP of all valid data concatenated together for subject 3 (Initial rest, three post-exercise trial and final rest). The estimated SBP and DBP track the reference over wide range (from 110 to 150 mmHg for SBP and from 70 to 90 mmHg for DBP). BP was increased after each exercising session followed by short-term recovery. Trials 3 and 5 were removed because the data included some noisy heart beats from wrist movements. Reprinted with permission from [1].

mmHg for SBP and from 70 to 90 mmHg for DBP). The figure shows a sudden increase in BP after each 5-minute exercising session followed short-term recovery. This figure shows that BP increases in the long-term for 50 minutes due to successive exercising sessions.

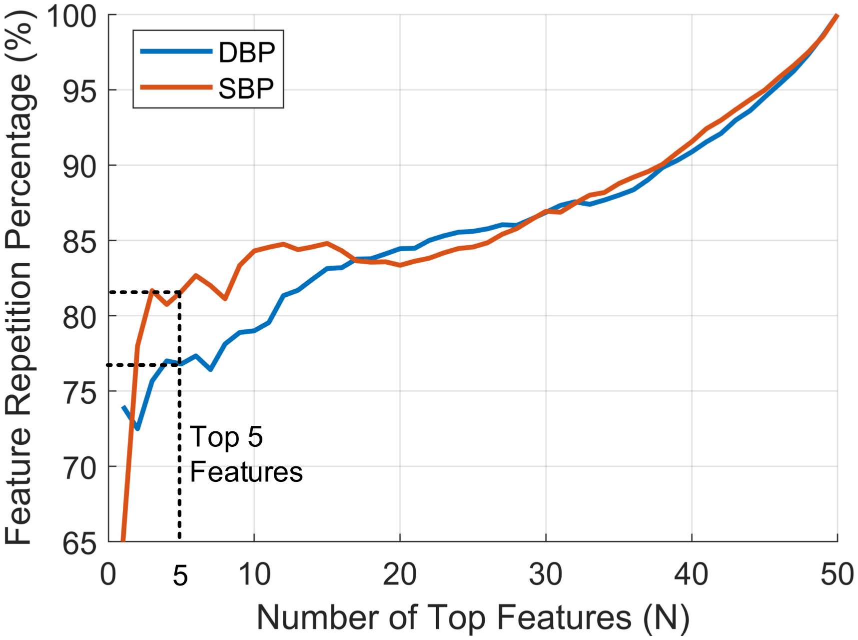

Figure 52. Average repetition percentage of top N important features among the 10 training folds. Reprinted with permission from [1].

4.5.3. Feature Importance Analysis

The feature importance score was calculated for each AdaBoost model for DBP and SBP for each subject by counting the times a feature was used to split a node, weighted by the number of samples it splits. We checked the detection of the right BP parameters for each AdaBoost model by measuring the consistency of feature ranking for the different training folds for each BP model. We calculated the percentage of the repetition of the top N important features in the top N rankings of the 10 folds used in model training. In Figure 52, the average repetition percentage is plotted for all features with top 5 features are repeated on average of 77% for DBP and 82% for SBP.

The top 20 important individual features for DBP and SBP are shown in Figure 53, which were calculated from the average of their feature importance scores across all

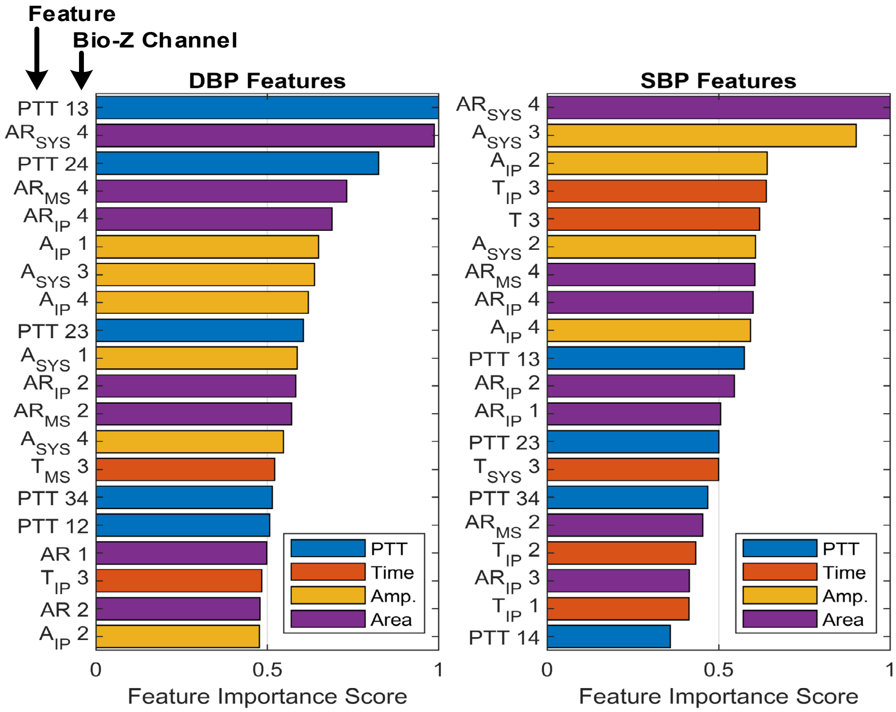

Figure 53. The top 20 most important individual features of DBP and SBP for all subjects. Reprinted with permission from [1].

the subjects, while the most important features categorized by type and point for DBP and SBP are presented in Figure 54. These figures show that the PTT features are the most important for DBP as previously shown in [40], while PTT, amplitude and area features are equally important features for SBP. In addition, PTT between the radial and ulnar arteries (PTT 13, 14, 23 and 24) are more important compared with PTT from a single artery (PTT 12 and PTT 34). This shows the importance of sensing the Bio-Z signals from both arteries to measure the time difference between the arrival of the pressure pulse to both arteries for more accurate BP estimation. We can also conclude from the feature importance categorized by points that the IP point is effective for BP estimation because

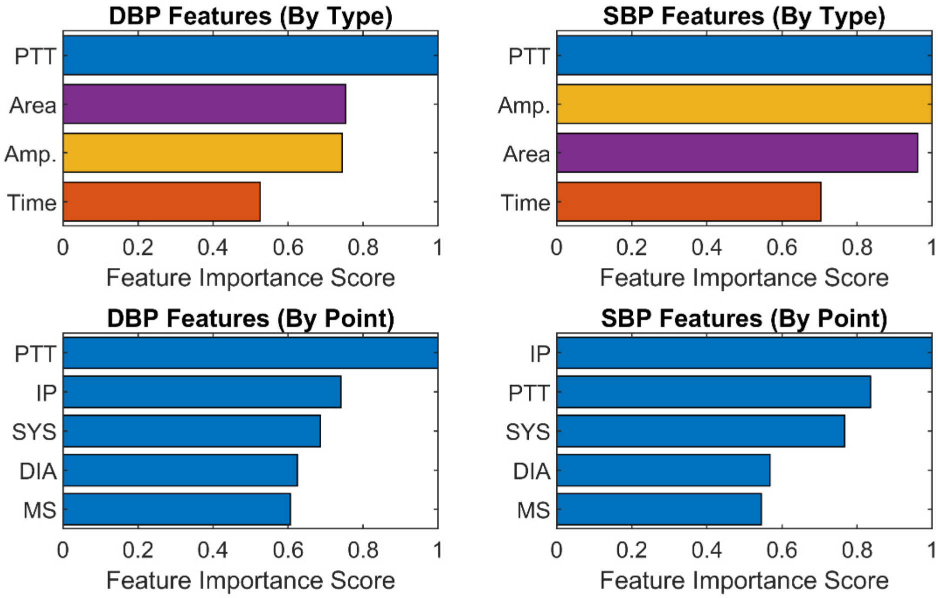

Figure 54. Feature importance for SBP and SBP categorized by feature type (top). Feature importance for SBP and SBP categorized by feature point (bottom). Reprinted with permission from [1].

it is the most important point for SBP and the second most important point for DBP. The features extracted from the IP point measure the amplitude and timing of the reflected pressure pulse through the arteries, which is highly correlated to BP [68].

4.5.4. Inter-subject Variability

The feature importance variation from one subject to another is shown in the histogram of the top 3 features of all subjects as illustrated in Figure 55. The most frequent feature is repeated for only 4 subjects for DBP and for 3 subjects for SBP out of 10 subjects. This shows the large variations in the important wrist BP features among subjects, which is the motivation for using subject-specific models to capture these

Figure 55. Histogram of top 3 individual features from all subjects. Reprinted with permission from [1].

individual variations instead of one global model for all subjects to achieve accurate estimated BP values.

4.5.5. Comparison with Different Regression Models and Previous Work

The BP estimation performance of the AdaBoost model is compared to other regression models such as Support Vector, Random Forest, Linear, Gradient Boosting and Decision Tree regression models as shown in Table 13. The AdaBoost model has the best performance compared to the other models. The linear model shows larger BP errors,

Table 13: Regression models comparison for DBP and SBP. Reprinted with permission from [1].

Regression Model	DBP		SBP	
	R	RMSE (mmHg)	R	RMSE (mmHg)
AdaBoost	0.77	2.6	0.86	3.5
Support Vector	0.76	2.7	0.83	3.8
Random Forest	0.73	2.7	0.72	4.2
Linear	0.66	3.3	0.76	4.5
Gradient Boosting	0.64	3.5	0.75	5.3
Decision Tree	0.62	3.5	0.68	5.1

which indicate that BP estimation from the used features is a non-linear problem that requires a non-linear model such as AdaBoost for more accurate results.

The window-based features show significant improvement compared to the beat-to-beat features as shown in Table 14 which has a worse correlation coefficient and RMSE for both DBP and SBP compared to the window-based features. Since we have a limited number of around 280 window samples per subject, we shuffled the data before splitting it into training and testing to include BP samples from all trials in the training dataset. However, we also tested our models without shuffling the data to use consecutive samples

Table 14: DBP and SBP estimation performance compared with other work. Reprinted with permission from [1].

Work	DBP			SBP		
	R	RMSE (mmHg)	MAE (mmHg)	R	RMSE (mmHg)	MAE (mmHg)
Window-based Features	0.77	2.63	1.95	0.86	3.44	2.51
Beat-to-beat Features	0.64	3.88	2.95	0.74	5.11	3.84
Window-based Features (Unshuffled)	0.5	3.34	2.59	0.62	5.0	3.74
[4]	0.57	3.52	4.31	0.54	5.45	8.21
[5]	0.79	2.2	-	0.85	3.1	-
[6]	0.84	7.47	-	0.81	5.17	-

Table 15: The comparison of the BP error for different sensors. Reprinted with permission from [1].

Bio-Z Sensors Placement	**DBP**		**SBP**	
	R	**RMSE (mmHg)**	**R**	**RMSE (mmHg)**
Ulnar pair of sensors only	0.73	2.8	0.82	3.8
Radial pair of sensors only	0.69	3.0	0.79	4.1
Average of single sensor only	0.65	3.1	0.75	4.4

in the training and testing our models. The RMSE increases for unshuffled data to 3.34 and 5.0 mmHg for DBP and SBP respectively, because the unshuffled data results in an increase in the difference between the BP values in the training and testing datasets. In our collected data, there is a variation of BP ranges from one trial to another because of the time duration between the trials, fatigue of the subject, removal of invalid data or other external factors. The measured average BP difference between closest pairs in the training and testing dataset is doubled from 0.08 mmHg for the shuffled data to 0.16 mmHg for the unshuffled data. In addition, the correlation between this BP difference and the measured BP error is 0.4 and 0.44 for DBP and SBP respectively. Therefore, the larger BP error measured from the unshuffled data is due to the larger BP difference between the BP values in training and testing datasets. This implies that the accuracy of BP estimation improves with larger training dataset that uniformly covers all BP ranges.

In comparison with other prior investigations using PTT from ECG and PPG signals in Table 14, our method offers better performance in all metrics compared to [4] and similar performance compared to [5]. In addition, the BP RMSE of our method is better by 4.9 mmHg for DBP and 1.7 mmHg for SBP compared to the previous work [6] that estimates BP from wrist Bio-Z.

We also investigated the BP estimation performance with a smaller number of sensors as shown in Table 15. The performance degrades when using two sensors only on the radial or the ulnar arteries compared to the full array of 4 sensors. Similarly, using two sensors is better than using only 1 sensor. This shows the importance of sensing the pressure pulse from multiple sensors from both wrist arteries for more accurate BP estimation.

4.6. Discussion

The results of this pilot study presented in the previous section show that BP can be estimated from the wrist using features extracted from an array of bio-impedance sensors with a small error for both SBP and DBP. We can conclude that our approach that employed information from both arteries can improve the accuracy of BP estimation from the wrist, which helps in achieving an accurate wearable device for cuffless BP monitoring. However, these results were achieved under specific assumptions. First, the results were shown for 10 healthy subjects with a limited range of age for only post-exercise BP variations for one day. Our approach requires detailed validation with a larger number of subjects including hypertensive people for different blood pressure modulation mechanisms. In addition, the long-term validity of the developed BP models can be tested on different days with a new attachment of the electrodes, which was shown in a previous cuffless BP method [69]. Second, a unique model was trained for each subject to capture the individual variations of BP parameters from the wrist arteries for better BP estimation performance. However, calibration data is required to be measured from each user to build its unique model. Third, the location of the wrist arteries was detected by measuring the blood flow using an ultrasound Doppler device in order to place the sensors directly over the arteries which is not applicable to an easy-to-use wearable device. In addition, each time the user wears the wearable device, the sensors can be placed on a different location on the wrist which may be far from the arteries and could result in using a wrong model. Therefore, a method is required for automatic artery detection each time the user wears the device. Our future solution for this problem is to use a larger array of sensors that covers both arteries. Signals will be monitored from each sensor on the array and based on some specific metrics, the sensors close to the artery can be detected. Fourth, fixed posture with a specific position of the participant's wrist on the bench was used during the whole data collection process. The change of posture and wrist position relative to the heart causes changes in the BP. These BP changes can be corrected using a motion sensor placed on the wrist to detect the height of the wrist relative to the heart and the posture through activity recognition methods. Finally, we used wet electrodes in the data collection, which have a large size and are not applicable for long-term usage because of the skin irritation and dryness of the gel over time. Using smaller dry metal electrodes solves this problem and helps in developing an array of electrodes on a small area of 5cm x 5cm which can fit in a wrist band as we proposed in [70]. However, dry electrodes may suffer from motion artifacts more than wet electrodes, which can cause signal corruption during wrist and body movements. However, studies showed that taking BP readings every 30 minutes is enough to predict cardiovascular disease. Therefore, a wrist-worn device with a motion sensor can detect when the wrist is at rest to start measuring the Bio-Z signals for a few seconds without motion artifacts, which is enough for accurate BP reading. In addition, sleeping time is more important than daytime for BP measurements, meanwhile it an excellent time to measure valid data without motion artifacts.

4.7. Conclusions

In this chapter, we presented a method for cuffless blood pressure monitoring from the wrist using an array of bio-impedance sensors. Two pairs of sensors were placed on the radial and ulnar arteries of the wrist to capture the vascular properties of the two arteries. We showed our low noise circuits for accurate bio-impedance sensing from the wrist. Systolic and diastolic blood pressure were measured using AdaBoost regression model based on different features extracted from the bio-impedance signals. In this pilot study, data was collected from 10 human subjects after exercising to evaluate the performance of our method for post-exercise BP variations. The results showed a large correlation coefficient and small root mean square error of 2.6 and 3.4 mmHg for diastolic and systolic blood pressure respectively. Leveraging window-based features and an array of sensors provided a smaller error compared to using sample-based features and a pair of sensors on only one artery. In this chapter, we proposed a new method for continuous blood pressure measurement in a comfortable form factor such as smart watches, which can contribute to more effective monitoring and management of cardiovascular disease.

5. NOVEL BIO-IMPEDANCE SENSING METHODS FOR IMPROVED BLOOD PRESSURE MONITORING

5.1. Overview

Continuous monitoring of cardiac parameters such as blood pressure (BP) and pulse transit time (PTT) from wearable devices can improve the diagnosis and management of the cardiovascular disease. Continuous monitoring of these parameters depends on monitoring arterial pulse wave based on the blood volume changes in the artery using non-invasive sensors of bio-impedance (Bio-Z). In this chapter we present two novel methods for enhancing the measurement of the arterial pulse wave in order to improve PTT and BP monitoring.

For the first method, PTT and BP monitoring require the measurement of multiple pulse signals along the artery through the placement of multiple sensors within a small distance. Conventionally, these Bio-Z sensors are excited by a single shared current source, which results in low directivity and distortion of pulse signal due to the interaction of the different sensors together. For a localized pulse sensing, each sensor should focus on a certain point on the artery to provide the most accurate arterial pulse wave, which improves PTT and BP readings. In this method, we propose a multi-source multi-frequency method for multi-sensor Bio-Z measurement that relies on using separate current sources for each sensor with different frequencies to allow the separation of these signals in the frequency domain, which results in isolation in the spatial domain. The effectiveness of the new method was demonstrated by a reduction in the inter-beat-interval

(IBI) root mean square error (RMSE) by 19% and an increase of average PTT by 15% compared to the conventional method.

For the second method, local blood pulsatile sensors from wrist-worn devices are affected by the change of sensing location relative to the arteries due to movements of the wearable device which degrade the BP estimation accuracy. This chapter presents a cuffless BP monitoring method based on a novel bio-impedance (Bio-Z) sensor array using a wristband that provides a robust blood pulsatile sensning and blood pressure estimation without calibration methods for the sensing location. The wristband is flexible and has a wearable form factor that includes an array of small built-in electrodes that conforms with the wrist shape to provide high-quality biosensing of the blood activity from multiple locations on the wrist. We use a convolutional neural network (CNN) autoencoder that reconstructs an accurate estimate of the arterial pulse signal independent of sensing location from a group of six Bio-Z sensors within the sensor array. Furthermore, we propose new BP features extracted from the dicrotic notch and the histogram of the arterial pulse signal to improve the accuracy of BP estimation. We rely on an Adaptive Boosting regression model which maps the features of the estimated arterial pulse signal to systolic and diastolic BP readings. Subject-specific BP models are created to capture the individual properties of the arterial blood pulsation. The performance of the BP monitoring system was demonstrated for 6 hours of BP data collected from 4 participants. The data included large BP changes of about 50 mmHg repeated 12 times for each participant at four different sensing locations. BP was accurately estimated at a fixed location with an average correlation coefficient and root-mean-square error (RMSE) of

0.80 and 5.0±0.5 mmHg for diastolic BP and 0.79 and 6.6±0.7 mmHg for systolic BP, respectively. Furthermore, our proposed methods of the sensor array with the CNN autoencoder improved BP estimation at different sensing locations by 34.1% for correlation coefficient and 15.9% for RMSE compared to using a single sensor method.

5.2. Multi-source Multi-frequency Bio-impedance Measurement Method for Localized Pulse Wave Monitoring[4]

5.2.1. Introduction

For PTT and BP measurements from the wrist, we need to place multiple Bio-Z sensors at the wrist arteries within a small distance that focus on specific points on the artery to measure localized PTT and subsequently BP [1, 21, 24]. The conventional method of measuring PTT from multiple Bio-Z sensors is based on measuring multiple voltage signals excited by a single shared current source [41]. In this case, multiple Bio-Z voltage electrodes are placed in between a pair of current electrodes that are connected to a shared current source which results low directivity of the measured pulse signal. The measured voltage signal corresponds to the target pulse signal at the voltage sensing site, but distorted by unwanted signal due to the impedance change within the tissue area of the other sensors as shown in Figure 56(a). Therefore, each measured pulse signal using a single current source will represent an average of the pulse activity over a wide area of the

---

[4] Part of this chapter is reprinted with permission from "Multi-source Multi-frequency Bio-impedance Measurement Method for Localized Pulse Wave Monitoring," by B. Ibrahim, A. Talukder and R. Jafari, 2020. *42nd Annual International Conference of the IEEE Engineering in Medicine & Biology Society (EMBC)*, 2020, pp. 3945-3948, Copyright 2020 by IEEE.

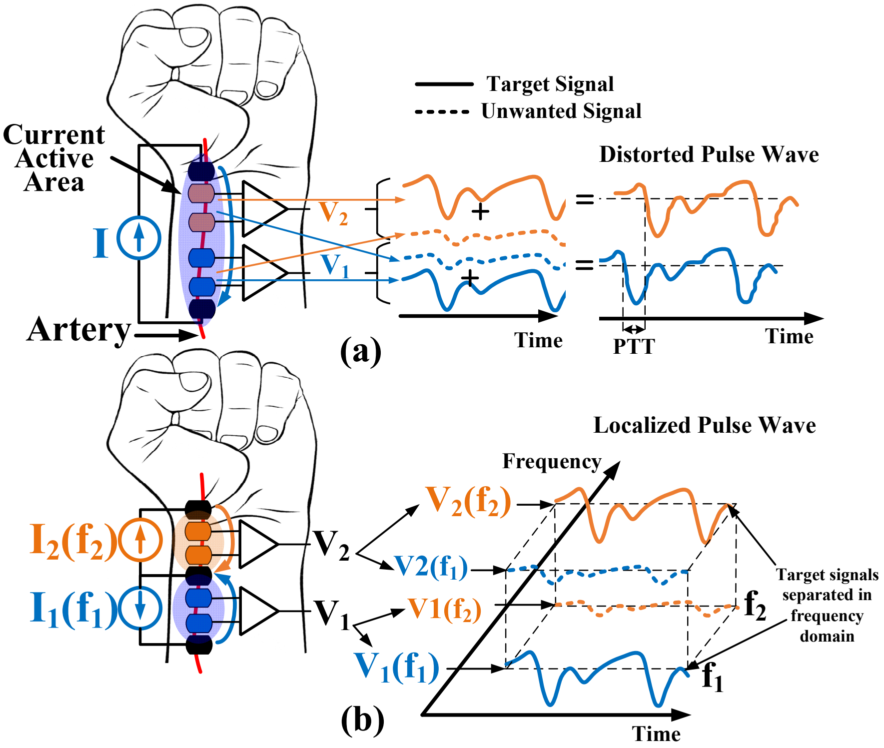

Figure 56. (a) Conventional Bio-Z sensing for PTT using single current source. (b) Proposed multi-source multi-frequency bio-impedance sensing method for localized pulse wave monitoring. Reprinted with permission from [2]

artery that results in low directivity and distortion of the pulse signal that reduces the accuracy of PTT and BP features, which cause higher error in BP estimation.

In this chapter, we propose using a separate current source for each Bio-Z voltage channel with different current injection frequencies for each current source as shown in Figure 56(b). Each current source is responsible for injecting current signal in a certain location at each voltage sensor. Each voltage channel will combine the target signal from the corresponding current source in addition to other unwanted signals from all other current sources. If a single frequency used for all current sources, we will not be able to separate the target signal from the unwanted signals. In our method, we are using different frequencies for the current sources, in addition to bandpass filters at the voltage sensing side to pass only the target signal from the corresponding current source at the sensing location while removing all the other unwanted signals from the other locations activated by the other sources. Therefore, the separation of current signals in the frequency domain will result in spatial isolation between the different Bio-Z sensors. Consequently, this method measures localized pulse signal with more focus on a specific point on the artery, which leads to sharper Bio-Z pulse with improved BP features. The sharper Bio-Z pulse leads to lower IBI error compared to a reference pulse signal for each Bio-Z signal and higher PTT values between the Bio-Z sensors. Lower IBI error leads to an improvement in the detection of pulse characteristics, which improves the BP accuracy. In addition, larger PTT values result in BP estimation with less sensitivity to the PTT error and thus more accurate BP monitoring.

In this chapter, Section 5.2.2 explains the hardware and signal processing methodology. Section 5.2.3 covers the reporting and discussion of the experimental results. The conclusion is presented in Section 0.

5.2.2. Methods

5.2.2.1. Bio-Z & PTT Measurement Hardware

We used our custom multi-source Bio-Z measurement system to monitor PTT by using two pairs of Bio-Z sensors to track the bio-impedance change along the radial artery and three electrodes had been used to inject multi-frequency AC currents. The system is based on an ARM Cortex M4 MCU that controls the generation of the AC currents with programmable amplitude and frequency by using two 16-bit DACs. Based on the experimental testing of the Bio-Z sensor on radial artery at 2 to 16 kHz, the frequencies were chosen to be 10.42 kHz and 11.72 kHz with frequency separation between them equal to 1.3 kHz, which is sufficient to use a bandpass filter to select the target carrier signal and filter out the other carrier with high attenuation. Two identical Howland current sources with similar schematics as shown in Figure 57(a) worked as V-to-I converter to transform each DAC voltage waveform into the current signal. Howland current source is a unity gain difference amplifier based on LT6375 chip from Analog Devices which produces a current dividing the input voltage by a load resistance. The GND terminal of the load of the Howland current source is shared between the two sources and connected to an additional electrode placed between two pairs of Bio-Z sensors. The sensing path for each Bio-Z sensor included instrumentation amplifier (IA) which is AD8421 from Analog Devices with a low noise spectral density of 3.5 nV/√Hz at 1 kHz to obtain RMS error in Bio-Z measurements less than 1mΩ. The IAs are followed by an ADC that samples the Bio-Z signals at a sampling rate of 78.125 ksps as shown in Figure 57(b). All the channels f the ADC were sent to the MCU, then stored in the PC as binary files through a USB bridge from FTDI. The carrier from the DAC output was used to demodulate the ADC signals using MATLAB code. The signals were followed by a low-pass filter with a cut-off frequency of 6.0 Hz to remove high-frequency noises. A PPG signal from the finger was used as a reference pulse signal which was measured using a finger clip device connected with AFE4490 EVM by Texas Instruments. To analyze the improvement of the method a single frequency current injection circuit has been used. Through MCU, an AC current at 10.42 kHz has been injected using a DAC and a V-to-I board. Two pairs of Bio-Z sensors were used to estimate PTT.

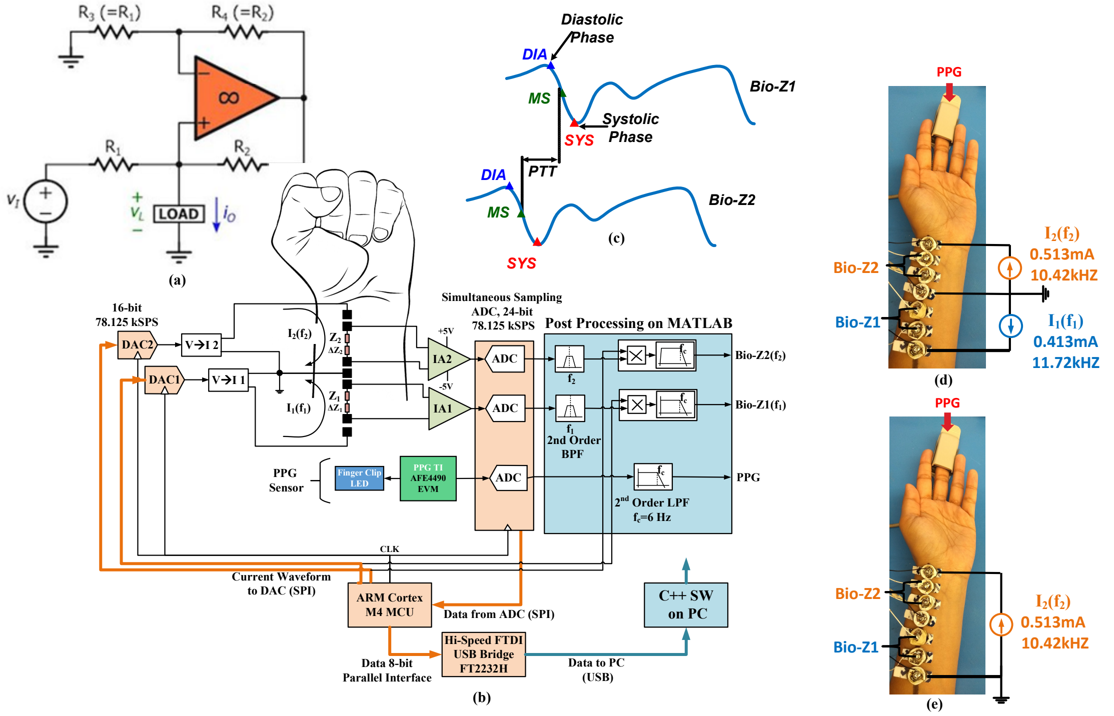

Figure 57. (a) Howland current source, (b) PTT measurement circuit schematic including PPG, (c) estimation of PTT form the time delay of two Bio-Z signals, (d) the placement of Bio-Z electrodes on the wrist for multi-source current injection, (e) the placement of Bio-Z electrodes on the wrist for single current source injection. Reprinted with permission from [2].

5.2.2.2. Bio-Z Features

The Bio-Z sensors are placed on a wrist to extract certain features and points from each pulse signal. When the heart pumps blood into the arteries, the Bio-Z signal falls from the peak point (DIA) which represents the diastolic phase to the foot point (SYS) which represents the systolic phase passing a maximum slope point (MS) as shown in Figure 57(c). As a new pulse arrives, there may be some smaller peaks and foots showing the reflection of blood through the wrist arteries.

PTT is the time difference that pulse needs to reach one point from another, thus PTT can be measured directly from the delay between the two Bio-Z signals on the wrist. As the distance between the electrodes is very small and the circuit is highly sensitive, a slight variation of movement can cause different delays in their peak and foot points. In order to ensure the highest accuracy, PTT has been estimated from the differences of the maximum slope points (MS) between two Bio-Z signals.

Root mean square error (RMSE) of inter beat interval (IBI) was also extracted from the pulse signals to monitor the quality of the signal. IBI is estimated as the difference between two consecutive MS. The IBI of Bio-Z has been compared with the IBI of the reference PPG to get the RMSE error as follows:

$$\text{IBI RMSE Error} = \sqrt{\frac{\sum_{i=1}^{n}(|IBI\ Bioz_i - IBI\ PPG_i|)^2}{n}} \tag{5.1}$$

5.2.3. Experimental Results

The Bio-Z sensor was first calibrated using reference resistors that simulate the body to form a relation between the measured voltage and the reference resistance. The wrist tissue resistance and skin resistance were considered as 55.6 Ω and 2.1 kΩ respectively based on our measurements using wet ECG electrodes that have been used to inject current and to receive signals from the wrist. Each DAC and current source was calibrated at each current injection frequency. The radial artery has been detected using Huntleigh Dopplex MD2 Doppler, which measures blood flow in the arteries. The electrodes were placed with 15mm distance between each other.

The data was collected under IRB approval IRB20170086D using gel electrodes with size of 0.8x1.5 cm from four participants with five trials while seated on a chair at rest; each

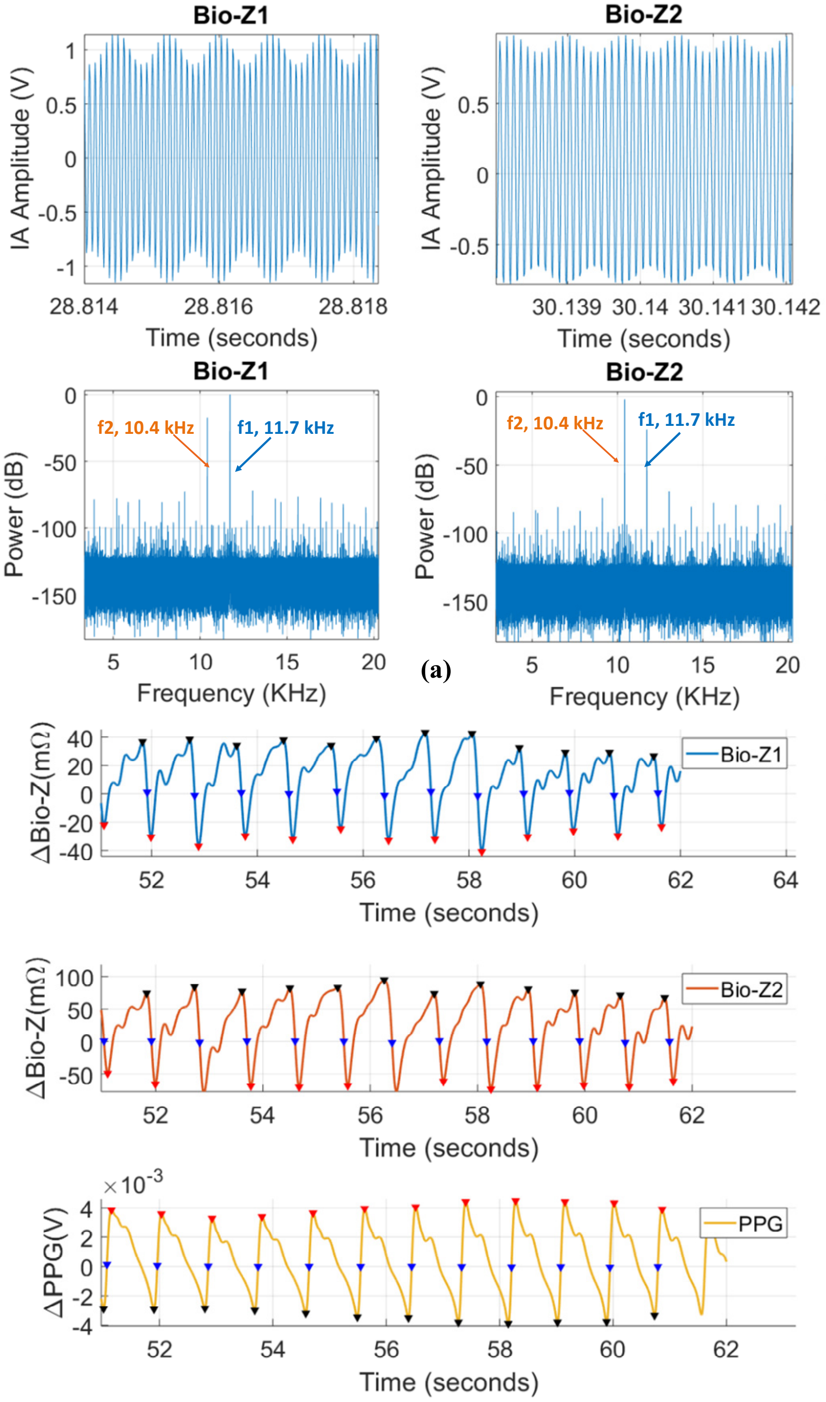

(a)

(b)

Figure 58. (a) The IA voltage output in time domain and its power spectral density showing the 2 frequency components, (b) The pulse signal from Bio-Z1, Bio-Z2 and PPG in time domain. Reprinted with permission from [2].

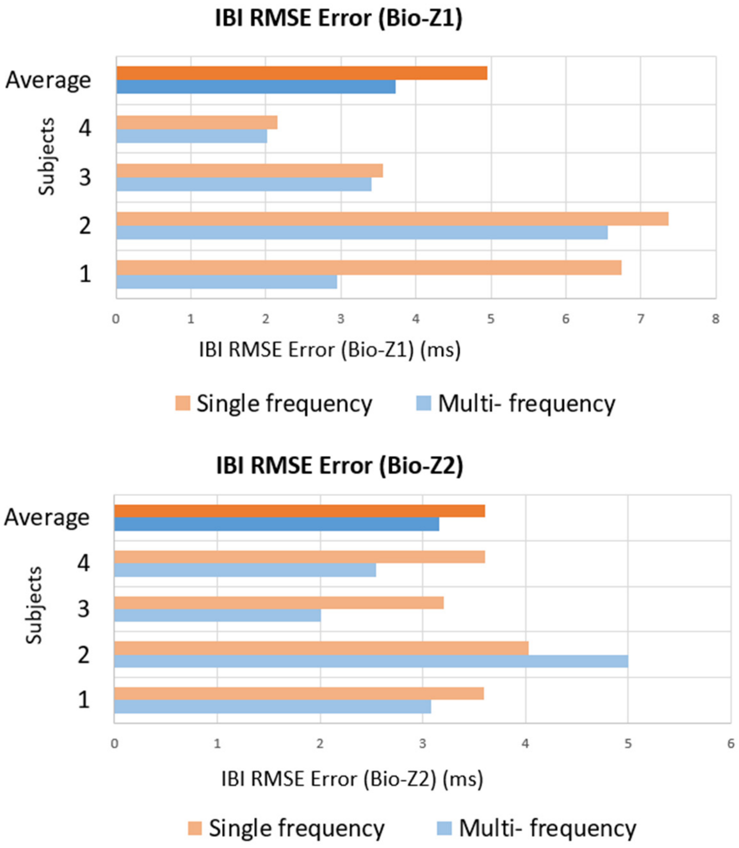

Figure 59.Average IBI RMSE of Bio-Z1 and Bio-Z2 along with individual subject values. Reprinted with permission from [2].

trial was one minute to provide an average of 345 heart beats per subject. The multi-frequency current was injected with an amplitude of 413µA at frequency 11.72 kHz at Bio-Z1 sensor and 513µA at frequency 10.42 at Bio-Z2 sensor. The injected current amplitudes were selected to be compliant with safety standards [30]. For comparison, the same procedure has been repeated with the same placement of electrodes for all four subjects using single frequency AC current with an amplitude of 513µA at frequency 10.42 kHz. The data for multi-frequency current method and single frequency current collected sequentially after each other keeping the same electrode attachment to minimize

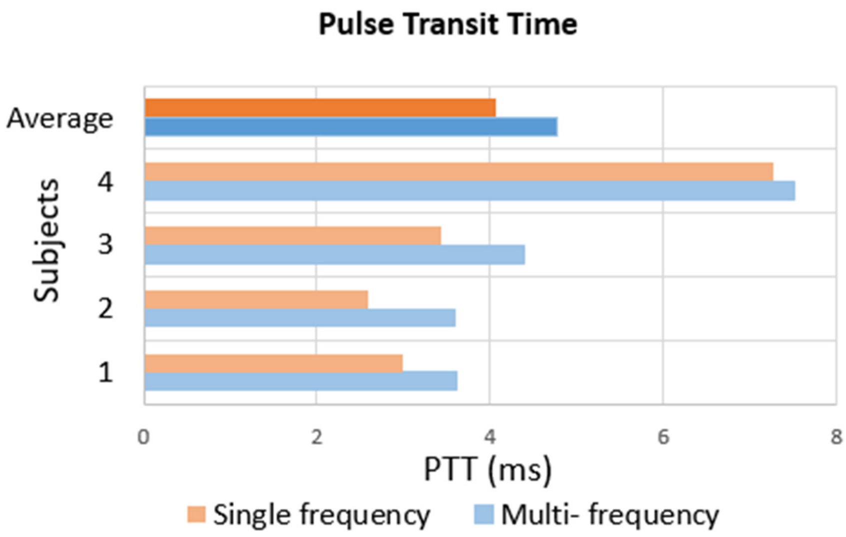

Figure 60. The average PTT with individual subject values. Reprinted with permission from [2].

any physical change over time. As expected the main frequency component of Bio-Z1 is 11.72 kHz but it also has a significant component of 10.4 kHz; Bio-Z2 also shows the opposite pattern in the frequency domain as shown in Figure 58(a). In Figure 58(b), the pulse signal of Bio-Z1 and Bio-Z2 are shown with the PPG signal over time. The average IBI RMSE error for all subjects was less in the case of multi-frequency current injection for both Bio-Z as shown in Figure 59. In the case of Bio-Z1, the average IBI RMSE error decreased by 25% from 4.96 ms to 3.73 ms and for Bio-Z2, it decreased by 12% from 3.61 ms to 3.16 ms as shown in Table 16. According to the blood flow direction towards the hand, Bio-Z1 showed the decreasing slope indicating blood arrival before Bio-Z2. The average PTT for multi-frequency current method is 4.78 ms which is 15% higher than the single frequency current injection which is 4.07 ms as shown in Figure 60. The proposed method requires an additional electrode, which can fit in the original form-factor through using slightly smaller electrodes.

Table 16: Average IBI RMSE Error and average PTT. Reprinted with permission from [2].

Method	Average IBI RMSE Error		Average PTT
	Bio-Z1	Bio-Z2	
Multi-frequency	3.73 ms	3.16 ms	4.78 ms
Single-frequency	4.96 ms	3.61 ms	4.07 ms

5.3. Calibration-Free Algorithms for the Sensing Location based on CNN Autoencoder

5.3.1. Introduction

In chapter 4, we showed that using pulsatile activity from Bio-Z signals and using features extracted from multiple sensors at different arteries improve BP estimation compared to a single sensor. However, the Bio-Z sensors were based on conventional Ag/AgCl wet electrodes, which due to lack of wearability and dryness of the contact surface gel, are not appropriate for long-term data collection. In this work, we present an electrode array consists of small 48 built-in silver electrodes embedded in a 2-dimensional matrix of 6 by 8 that are robust against the aforementioned issues and demonstrate constant skin-electrode impedance with negligible fluctuations over time. Accurate mapping of Bio-Z pulses to BP substantially depends on accurate detection of dynamic time-dependent behavior of the wrist arterial pulsatile. Therefore, the wrist-worn sensor array is designed in a flexible wristband, which conforms with the wrist shape and provides a robust contact with the skin for reliable current injection and voltage sensing.

Our previous work was constrained by placing the 4 sensors precisely on the wrist arteries for the whole study after detecting the location of the arteries. The fixed sensing location provided low-error BP predictions because the BP models were trained and tested at the same sensing location based on consistent pulse signals. However, the sensor in a wrist-worn device changes its location frequently due to user movements and placing the device at different locations. Each sensing location provides different morphology for the pulse signal based on the tissue transfer function between the artery and sensor at the skin. Therefore, the change in sensing location affects the measured pulse signal and the BP models. As a result, BP models behave poorly by changing the sensing location. The solution to this problem can be expensive and complicated by calibrating the BP models for sensing location by collecting data from multiple locations and training multiple BP models for all possible locations. Then for BP predictions, the sensing location is detected to select the suitable BP model for predicting BP as a function of the sensing location. This approach requires collecting a lot of data at different sensing locations which is inconvenient to the user. In addition, complicated algorithms are required for detecting the sensing location and predicting BP. Therefore, we propose in this study a new simple and reliable method for accurate BP detection independent of the sensing location without the need for complex calibration algorithms for the sensing location.

In this chapter, we use the Bio-Z sensor array in a novel method to accurately estimate the true pulsatile activity of the artery independent of the sensing location. The BP models that are trained by features extracted from the estimated arterial pulse signal provide consistent and reliable BP predictions with different sensing locations. This calibration-free method for the sensing location relies on combining the pulse signals from multiple sensing locations to reconstruct the true arterial pulse signal independent of the sensing location. The reconstruction method depends on an autoencoder which is an

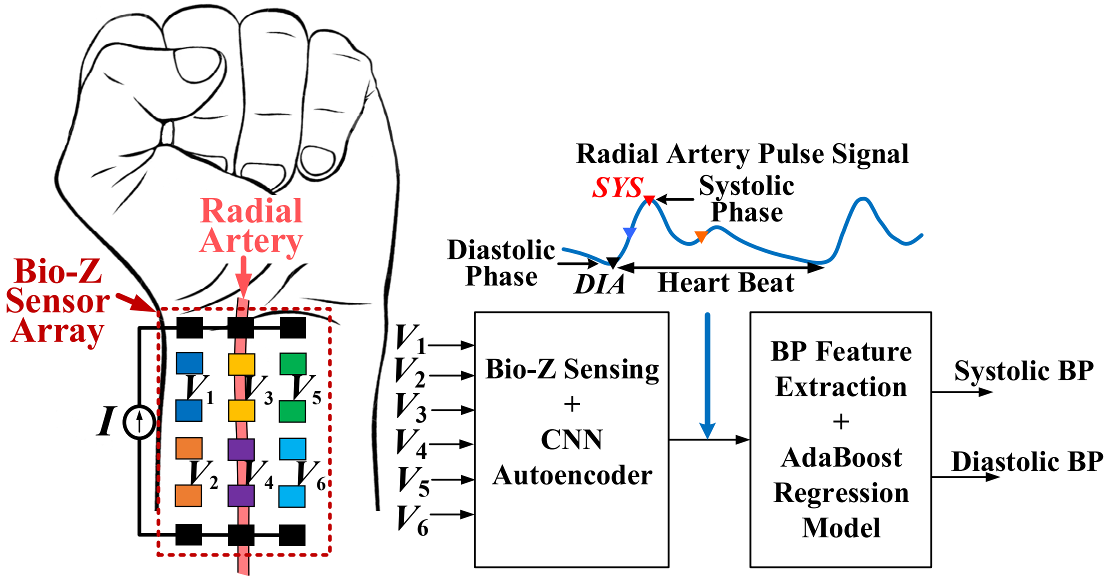

Figure 61. The proposed wrist worn device for the cuffless blood pressure (BP) monitoring based on an array of 6 bio-impedance (Bio-Z) sensors and convolutional neural network (CNN) autoencoder algorithm to provide the arterial pulse signal. The systolic and diastolic BP are predicted based on AdaBoost regression model trained by BP features extracted from the estimated arterial pulse signal.

unsupervised machine learning algorithm that can compress a high-dimension input into its lower dimension representation. The estimated lower dimension signal is equivalent to the target pulsatile activity. The autoencoder is implemented using a convolutional neural network (CNN) which can effectively learn the transfer function between the artery and each sensor based on the training data of Bio-Z pulse signals without any labels. As a result, the autoencoder can reconstruct the artery's pulsatile signal which is used to BP feature extraction and predictions. In addition, we propose new additional set of features that focus on reliable representation of the significant parts in the pulse morphology for more accurate BP prediction. The new set of features include the histogram of the pulse amplitude in addition to the complete characteristics of the dicrotic notch which is the secondary peak point in the middle of the heartbeat pulse morphology. We show that these features are highly correlated with BP and can significantly improve the BP predictions.

In this work, we show the development of the hardware and signal processing algorithms for a cuffless BP system based on a wrist-worn device. The system includes an array of 6 Bio-Z sensors activated from 3 electrode columns in the wristband of the electrode array as shown in Figure 61. The wristband is connected to our custom multi-channel Bio-Z sensing hardware for high-resolution Bio-Z sensing. The proposed CNN autoencoder reconstructs the radial arterial pulse signal from the raw pulse signals from the 6 Bio-Z sensors. This study demonstrates using AdaBoost regression models based on the features extracted from the arterial pulse signal to estimate SBP and DBP based on the significant BP features in the morphology of the estimated arterial pulse signal. We show in this work that the Bio-Z sensor array combined with the CNN autoencoder method can estimate reliable pulsatile activity that improves the BP estimation accuracy at different sensing locations compared to the use of a single Bio-Z pulse signal.

5.3.2. Methods

5.3.2.1. Introduction

The proposed method for cuffless BP measurements from a wrist-worn device rely on using small-form factor of non-invasive sensors that measure blood pulsatile activity from the arteries and transform them into BP models using regression models. The sensors need to be placed as close as possible to the artery for accurate and consistent measurement of the arterial pulsation that results reliable BP estimation. The change of sensing location away from the artery results in changes in pulse signal morphology and BP results. These changes are significant for the small-form factor sensors that are integrated into a wrist-worn device because they suffer from frequent position displacements on the wrist due to user movements of the arm and when the user takes off the device and re-attaches it to the wrist at a different location. These continuous displacements affect the measured pulse signal and the accuracy of BP estimation.

The arterial pulsation sensing can be modeled by source signal (Y) that represents the arterial pulse located deep inside the tissue at the location of the artery. The sensor placed on the skin measures the signal V which is the output of the transfer function (h) with the input is arterial pulsation Y that represents the effect of the tissue and the distance between the sensor and the artery as shown in Figure 62(a). Therefore, transfer function (h) changes for different locations of the sensor on the skin relative to the artery's location which causes changes in the sensor output signal (V). Since, the BP estimation relies on the morphology of the pulse signal, the changes occur in the sensor output with location increase the BP error. In order to reduce the effect of the sensing location on the estimated signal, we propose using multi-sensor pulse signal estimation from multiple locations around the target artery instead of single point measurement as shown in Figure 62(b).. Each sensor output is a function of the source arterial pulse signal with the function varies with sensing location. The estimated multi-sensor pulse signals are used for the reconstruction of the arterial pulse autoencoder. The autoencoder is an unsupervised machine learning algorithm that finds the lower-dimension representation of the high-dimension input signals. This method provides accurate pulsatile activity of the artery

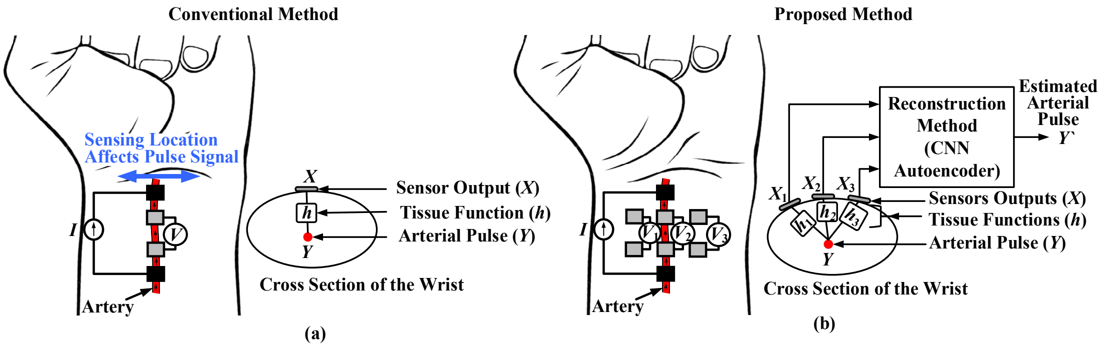

Figure 62. (a) The conventional method of measuring the pulsatile activity based on a single measurement that is affected by the sensing location and degrades BP performance. (b) the proposed method of using multi- sensor pulse signal estimation that are used for reconstruction of the arterial pulse using CNN autoencoder. This method provides accurate pulsatile activity of the artery independent on the sensing location which improves the BP estimation at different locations.

independent on the sensing location which improves the BP estimation at different locations.

5.3.2.2. Sensing Model

In order to understand the transfer function (*h*), we created a model the explains the measured signal (*V*) as a function of the arterial pulsation. The blood pulsation in the artery causes changes in blood volume which leads to a change in impedance. The measured voltage signal is the multiplication of injected current and the tissue impedance. The amplitude of the measured pulse signal due to blood pulsation over a local segment on the artery is affected by the distance between the sensor and the artery. The pulse amplitude decreases as the distance between the sensor and the artery increases. In addition, the length of the segment that is measured on the artery is affected by the current distribution in the tissue which is maximum at the sensor location and decreases as the distance from the sensor increases. We can conclude from these observations that the relation between the measured signal $V(t)$ and the artery pulsation

The model consists of the signal $Y(t)$ that represents the blood pulsation in the artery which is the target signal for sensing. The pulse signal $Y(t)$ flows through the artery in the direction of blood flow. We can model the artery by dividing it along the blood flow direction into N elements as shown in Figure 63. Assume the signal $Y(t)$ represents the pulse signal at the first artery element ($n=0$) and the signal is delayed by each element with time delay t_d. Therefore, the signal at each element can be modeled as a delayed version of the original pulse $Y(t)$ and represented by $Y(t-nt_d)$ at element n. The measured signal $V(t)$ is modeled as the summation of the signals for all elements multiplied by a weight b_n that represents the effect of the tissue between the element and the sensor and this weight decreases as the distance between the sensor and the element increases. This model can be represented mathematically by this equation

$$X(t) = b_0 Y(t) + b_1 Y(t - t_d) + b_2 Y(t - 2t_d) + \cdots + b_{N-1} Y(t - (N-1)t_d)$$

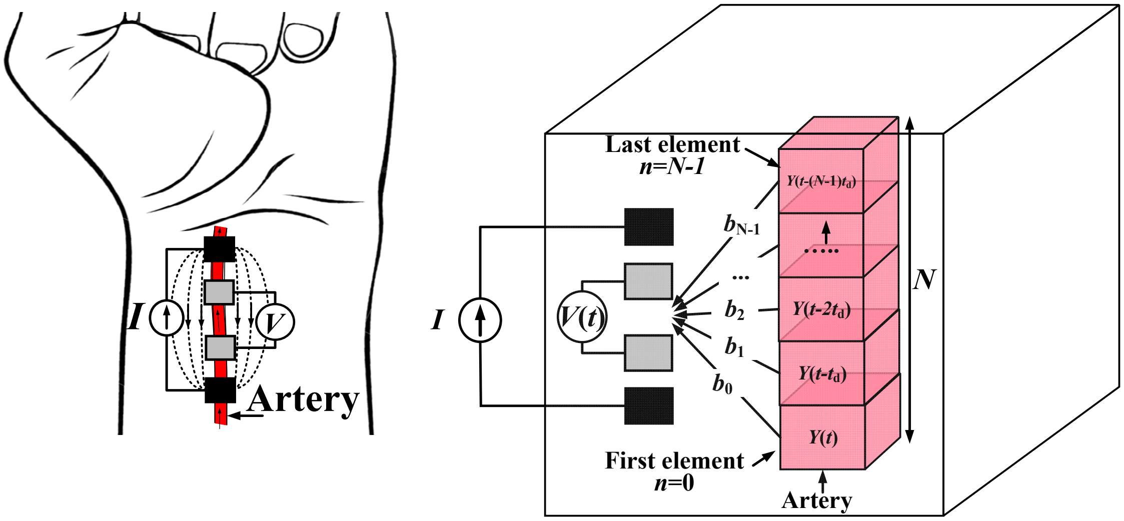

Figure 63. The Bio-Z pulsatile sensing model that represents the artery by N small segments and the pulsatile activity as $Y(t)$ that propagates in the artery with delay t_d for each artery's segment. The sensed signal $V(t)$ is the weighted sum of the pulse signal at each element which is equivalent to a linear filter for the transfer function (h).

This is the equation of a filter with impulse response consists of the weights b_n .This shows that the transfer function (*h*) between the artery pulse signal (*Y*) and the sensor output on the skin (*X*) can be considered as a linear filter. Based on this conclusion, we designed the reconstruction algorithm that can estimate the linear functions *h* for each sensor location which leads to the estimation of the source arterial pulse signal *Y* as explained in the following sections.

5.3.2.3. Arterial Pulse Estimation using Autoencoder

Based on the explained sensing model, each pulse signal from the sensor output X_i at the skin is related to the source signal of the pulsatile activity *Y* at the artery deep inside the tissue through the discussed transfer function of a filter *h* that is defined by certain weights b_n and depends on the sensing location. Our objective is to reconstruct the hidden arterial pulse signal *Y* from the measured pulse signals from multiple sensors outputs X_i at different sensing locations for i=1 to *K* where *K* is the number of sensors.

We propose using the unsupervised machine learning algorithm of autoencoder to estimate the arterial pulse signal *Y* from the input pulse signals X_i. The autoencoder is capable of estimating a lower dimension representation, called the code, from the higher dimension inputs. The autoencoder consists of an encoder network that encodes the inputs from the input layer into a lower dimension representation in the hidden layer which is decoded by the encoder network to reconstruct the inputs at the output layer as shown in Figure 64. The layers of the encoder and decoder networks are implemented as neural networks and their weights are estimated through the gradient descent optimization method to minimize the error between the input and output layers by minimizing the loss

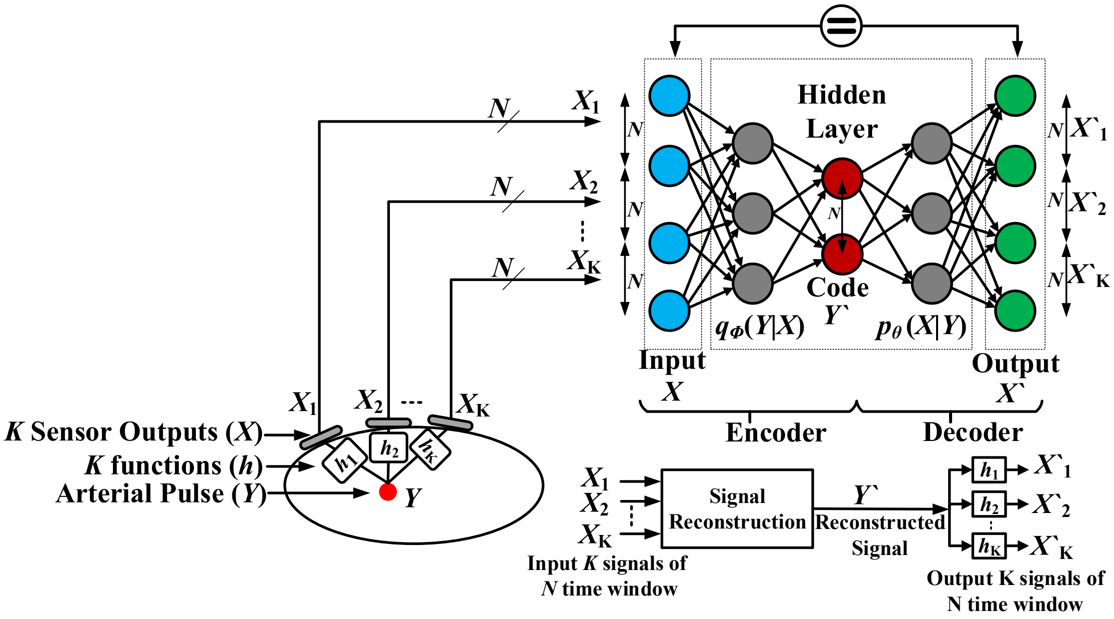

Figure 64. The proposed method of using an autoencoder to find a lower-dimension representation of the inputs from multiple sensors placed on the skin around the artery. The lower-dimension representation is the output of the encoder and represents the estimated arterial pulse signal. The decoder network is responsible of regeneration of the inputs at the output layer. The decoder network represents the linear transfer function of the artery to the sensor and the encoder represents the reconstruction function of the arterial pulse from the input observations.

function which is the square error between the input and output layers. As the number of sensors K and the dimension of the input increases, the accuracy of the code estimation increases.

The autoencoder can accurately estimate the arterial pulse signal when the decoder network is equivalent to the transfer functions h that maps the Y at hidden layer to the measured pulse signals X_i and in this case, the encoder network represents the target reconstruction function that reconstructs the arterial pulse from the input observations. This goal is achieved by implementing the encoder and decoder networks as convolutional neural network (CNN) with a linear activation layer which consists of a window of weights that sweeps the input dimensions similar to the operation of the filter that model the pulse transfer function. The input pulse signals are divided into overlapping time segments which are considered the input samples for the training of the CNN networks of the autoencoder. After the gradient descent optimization and minimizing the loss function, the weights of the encoder CNN are used to estimate the arterial pulse signal from the input signals which is used to extract the BP features for BP estimation using the regression models.

5.3.2.4. System Overview

The proposed wrist-worn BP monitoring system relies on an array of Bio-Z sensors from multiple locations on the wrist. The Bio-Z sensor array consists of six channels of Bio-Z sensing bio-instrumentation that interface with the body through a flexible wristband that conforms with the skin and includes a 2D array of metal electrodes to provide good contact with the skin for high-quality signal monitoring. The Bio-Z hardware includes injection of small AC current and voltage sensing from multiple pairs of electrodes. The measured voltage signals are pre-processed to extract raw Bio-Z signal which is followed by pulse detection algorithms to extract the pulse signals, denoted as ΔBio-Z. Then, the proposed CNN autoencoder combines the multiple Bio-Z pulse signals to estimate the arterial pulse signal called $\Delta\text{Bio-Z}_{AE}$ which is used for BP prediction. The next step includes the detection of the characteristic points of the pulse signals that are used to extract the BP features. Then, AdaBoost regression models are used to estimate

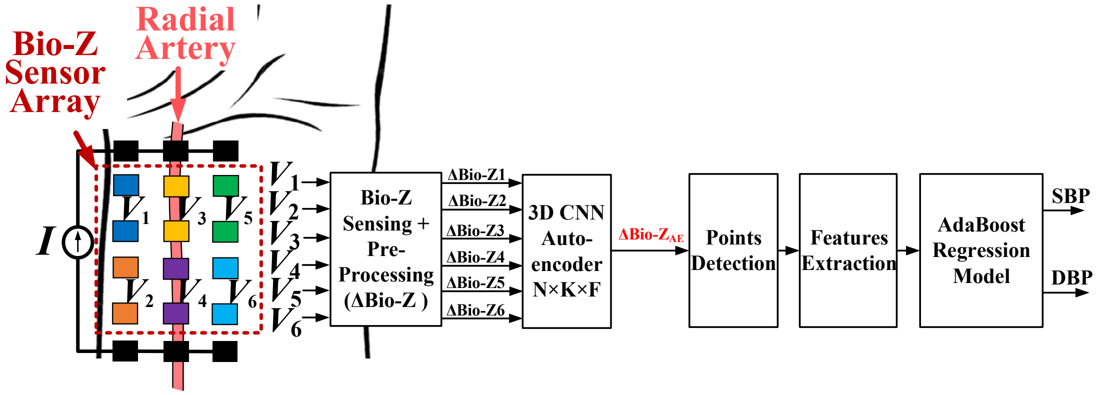

Figure 65. The wrist-worn BP monitoring system based on the Bio-Z sensor array on the wrist connected to the Bio-Z sensing hardware. The Bio-Z signal processing generate the pulse signals (ΔBio-Z) for each sensor which are used to estimate the arterial pulse signal (ΔBio-Z$_{AE}$) based on CNN autoencoder. The systolic BP (SBP) and diastolic BP (DBP) are predicted by AdaBoost regression model based on feature extracted from the characvterstic points of the estimated arterial pulse signal.

systolic and diastolic BP after training by Bio-Z and reference BP data collected simultaneously as explained in the following sections as shown in Figure 65.

5.3.2.5. Bio-impedance Signal Pre-Processing

5.3.2.6. CNN Autoencoder

For generalization, we assume we have *K* sensor signals that will be combined with the CNN autoencoder to reconstruct the arterial pulse signal denoted as ΔBio-Z$_{out}$ at the intermediate layer which the encoder output.

In order to arrange the input data for the CNN autoencoder, each pulse signal of ΔBio-Z is divided into separate heartbeats that have different amplitude and number of samples according to the heartbeat duration. The number of samples per heartbeat is equalized and downsampled to *L* samples for each heartbeat in the dataset per subject by interpolation of each heartbeat at new *L* time samples with equal time steps that span each heartbeat. The downsampling of the signals helps in reducing significantly the number of autoencoder parameters. Consequently, all the heartbeats are normalized in duration with the same time grid. In addition, the amplitude of the heartbeats is normalized by dividing the amplitude of the whole heartbeat by its peak-to-peak amplitude, so that the amplitude of all pulses has the same amplitude range.

The input K heartbeats sequence is divided into time segments of N heartbeats with a time step of 10% of the heartbeat period L. Then, each time segment is arranged in a 3D array of N heartbeats $N \times K \times L$ with N is the number of heartbeats, K is the number of sensors and L is the length of the pulse. This 3D array is the input to the autoencoder as shown in Figure 66. The encoder CNN network consists of a 3D convolution window with dimensions of $N \times K \times \mathrm{F}$ and stride of 1, where F is a fraction of L. The decoder network consists 1D CNN network repeated $N \times K$ times with a convolution window size of F and stride of 1. All CNN networks have a linear activation layer and zero biases to match the

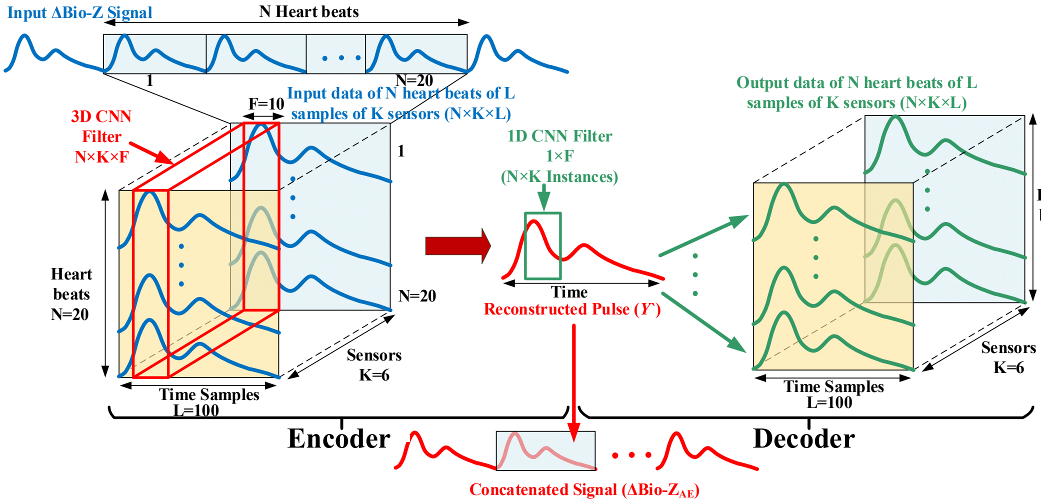

Figure 66. The description of the CNN autoencoder network structures and data arrangement. The input data are arranged in $N \times K \times L$ array and the encoder network includes a 3D filter with $N \times K \times F$ size and the decoder network 1D CNN network repeated $N \times K$ times with a convolution window size of F.

Table 17: The CNN autoencoder parameters.

CNN autoencoder parameters	Value
K	6
L	100
N	20
F	10

linear filter model that was adopted for the transfer function from arterial pulse to the sensor measurement. The total parameters to be trained for the autoencoder using this implementation is $2\times N\times K\times L$. The CNN autoencoder is implemented with Keras functions in Python. The autoencoder is training using Adam optimizer as a stochastic gradient descent algorithm with mean squared error as loss function. In order to ensure the continuity of the final encoder output ΔBio-Z_{out}, the encoder CNN is applied again after training with the input data as the concatenation of all the 3D arrays of the input data along the time axis. In addition, the encoder CNN coefficients are upsampled to the original heartbeat sampling rate and reapplied on the original heartbeat data before downsampling in order to generate the encoder output ΔBio-Z_{out} in the original high sampling rate to provide high time resolution in the next steps of point detection and feature extraction. In this study, the CNN autoencoder parameters are selected according to Table 17.

5.3.2.7. Bio-impedance BP Features Extraction

Based on the DIA, MS, SYS, IP, DN, and DP characteristic points, the features extracted from the bio-impedance pulse signal are categorized into sets of time, amplitude, area, dicrotic and histogram. The time intervals between DIA and MS, SYS, and IP are the time parameters for each signal normalized by the inter-beat interval (T_{IBI}) which is

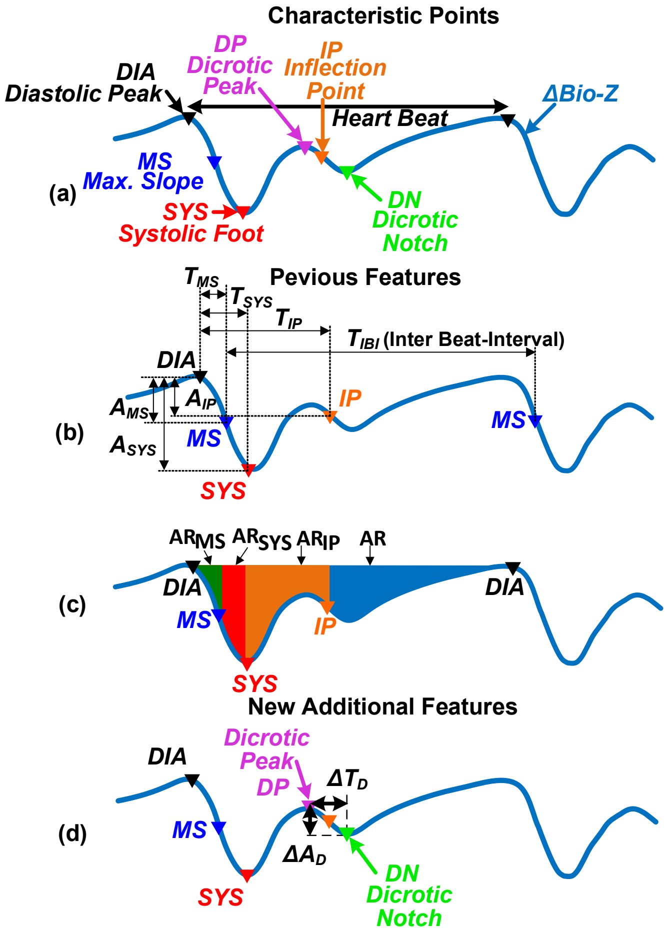

Figure 67. (a) ΔBio-Z signal over one heart beat with illustration of its six characteristic points. The points are diastolic peak (DIA), maximum slope (MS), systolic foot (SYS), inflection point (IP), dicrotic peak (DP) and dicrotic notch (DN), (b) The previous features of time and amplitude for a single bio-impedance signal from the diastolic peak to the rest of points, (c) The area features for a single bio-impedance signal from the diastolic peak to the rest of points, and (d) The new additional features proposed in this work in order to include the changes that occur in the dicrotic notch and peak points around the IP point in the BP estimation models.

the period of the heartbeat between successive MS points. Besides, the amplitude parameters for each bio-impedance pulse are the amplitude differences from DIA to MS and IP points normalized by pulse foot to peak amplitude A_{SYS}. Moreover, the area under the bio-impedance signal from DIA to the MS, SYS, and IP points represent the area

Table 18: Wrist Bio-Z features.

Feature Set	Feature Description	Number of Features
Time	The time interval from the DIA point to the MS, SYS and IP points, which are T_{MS}, T_{SYS} and T_{IP}, as shown in Figure 67(b), normalized by T_{IBI}.	3
Amplitude	These are the difference in amplitude from DIA point to the MS and IP points, which are A_{MS} and A_{IP} as shown in Figure 67(b), normalized by the pulse foot to peak amplityde A_{SYS}	2
Area	The areas under the ΔBio-Z curve starting from the DIA point to the MS, SYS and IP of points, which are AR_{MS}, AR_{SYS}, AR_{IP} normalized by full pulse area AR as shown in Figure 67(c). The area under the curve represents the total peripheral resistance.	3
Dicrotic	New added features for the dicrotic peak to notch amplitude ΔA_D and time ΔT_D normalized by A_{SYS} and T_{IBI} respectively as shown in Figure 67(d).	2
Histogram	The population of 5 amplitude bins which are the the division of the normalized pulse amplitude into 5 equal intervals.	5
Total		15

parameters for each signal normalized by the full pulse area. These sets of features were used in previous work and we introduce a new set of dicrotic features in this work. The dicrotic set of features are added to include the amplitude and time between dicrotic peak and notch normalized by A_{SYS} and T_{IBI} respectively which are highly correlated with BP changes. The final set of features is a new propsoed feature for the pulse amplitude histogram based on the population of 5 amplitude bins which are the the division of the normalized pulse amplitude into 5 equal intervals. The time, amplitude, area, dicrotic and histogram parameters are shown in Figure 67 (b), (c), and (d) and explained in Table 18.

The aforementioned features are substantially related to the cardiac output and the arterial stiffness of the wrist arteries and so, are highly correlated with BP. The time interval between the systolic foot and the inflection point measures the arterial stiffness, and besides, the area under the curve represents the total peripheral resistance of the blood vessel [63]. In addition, the ratio between the amplitudes of the systolic foot and inflection point relative to the diastolic peak determines the intensity of the reflection wave. In this regard, the features can accurately model the vascular properties of the wrist arteries and will be the basis for estimating the DBP and SBP.

5.3.2.8. BP Prediction Model

An advanced regression model is employed to translate the features extracted from bio-impedance signals to BP. Besides, since the DBP and SBP rely on different features, a separate regression model is utilized for each of them. In order to improve the accuracy of BP estimation, the individual variations of each participant's vascular properties are acquired. Therefore, the subject-specific models are trained for each participant in our study using a limited number of training window samples. AdaBoost is the regression model we used for our BP estimation. It is a meta-algorithm which by training a sequence of weak models through a weighted sum of different subsets of the training data set, improves the prediction power of the algorithm and boosts the performance of decision trees. In fact, AdaBoost is an ensemble technique that attempts to convert a set of weak classifiers into a strong one. The hyper-parameters of the AdaBoost models consist of the number of the decision trees and the tree depths, which were selected as 32 and 8, respectively. For each model, the tree depth with the minimum testing error is selected to provide the best model complexity that avoids both overfitting and underfitting. The Bio-Z and BP data are splitted by different configurations as explained in the Experimental Results section.

5.3.3. Results

5.3.3.1. Experimental Measurements

The human subject experiments for BP estimation were performed under the approval of the Institutional Review Board of the University of Texas A&M (IRB no. IRB2017-0335D). A total of N=4 subjects with age range from 20 to 25 years have participated in this study. In order to train and test the subject-specific BP models, we collected the wrist Bio-Z data from our sensor array simultaneously with reference BP data from a standard BP device. The Bio-Z signals were measured by the electrode array wristband with a size of 46×64 mm for the electrode array that was connected to the Bio-Z sensing hardware implemented in our custom Bio-Z XL board as shown in Figure 68(a). The wristband includes 6×8 array of silver electrodes with a size of 5×5 mm and 8.2 mm center-to-center spacing between electrodes as shown in Figure 68 (b). The electrode array was placed at the bottom side of the wrist to be close to the radial and ulnar arteries of the wrist for effective sensing of the arteries pulsatile activity. Three adjacent columns of the electrode array were utilized for Bio-Z sensing to measure 6 Bio-Z channels from different sensing locations around the radial artery. The Bio-Z current signal was injected in three columns by the electrodes at the top and bottom rows to provide the best current distribution for the three columns. The six bio-Z voltage signals were measured from the middle pairs in the three columns as shown in Figure 68 (c).

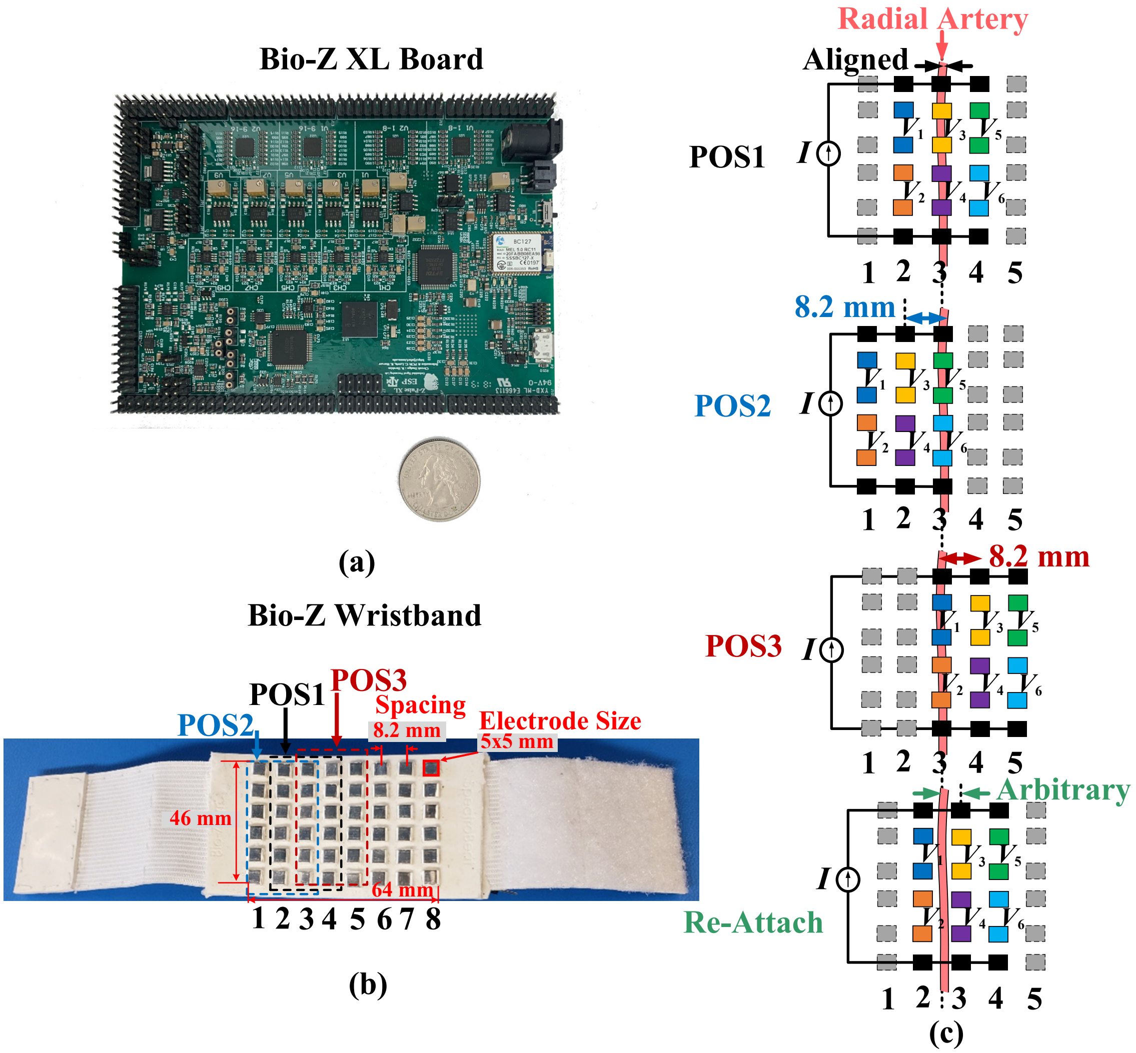

Figure 68. (a) Our custom Bio-Z sensing hardware (Bio-Z XL), (b) Our custom electrode array wristband that is connected to the Bio-Z XL board for Bio-Z data collection from the wrist, (c) The electrode configuration for the 6 Bio-Z signals that are collected at four different sensing locations which are POS1, POS2, POS3 and Re-Attach with the illustration of the used electrode columns and the distance relative to the radial artery for each sensing location.

Data collection was done during applying significant BP changes temporarily to evaluate our methods in predicting extreme BP changes. The experiment relied on repeating multiple trials of BP maneuvers that include elevation of BP temporarily above the normal level followed by BP recovery to normal values. The BP maneuvers we utilized for this study were based on using handgrip exercise and cold pressor test to elevate BP. In addition, we collected data at different sensing locations to evaluate the performance of the proposed BP estimation algorithms by changing the sensing location after training the BP model.

In order to provide sufficient data for BP model training, we collected 90 minutes of Bio-Z and BP data with around 6000 heartbeats from each participant divided among 12 trials of BP maneuvers and 4 sensing locations called POS1, POS2, POS3 and Re-Attach. The first 6 BP trials were measured at the initial sensing location POS1 from columns 2,3, and 4 with the middle column 3 aligned with the radial artery as shown in Figure 68(c). In order to consider the effect of different sensing locations on the BP estimation, we repeated the data collection at different sensing locations relative to the

Table 19: The description of the 4 sensing locations POS1, POS2, POS3 and Re-Attach and the corresponding electrode configuration, sensing distance from the radial artery and the number of BP trails for each sensing location.

Sensing Position	Electrode Configuration (Columns Used)	Sensing Location (Distance from the center electrode column to the radial artery)	Number of BP trials
POS1 (Initial)	2,3,4	0 mm (aligned with the radial artery)	6
POS2	1,2,3	8.2 mm left to the radial artery	2
POS3	3,4,5	8.2 mm right to the radial artery	2
Re-Attach	2,3,4	Arbitrary distance within 8.2 mm left or right to the radial artery	2

artery. We selected two fixed sensing locations by shifting the sensing electrode columns by 1 column to the left and the right of the radial artery without taking off the sensor band from the wrist. The selected electrode configuration provides displacement in sensing location by 8.2 mm to the left and the right of the radial artery. These two new sensing locations are defined as POS2 and POS3 as shown in Table 19. In addition to the fixed change in sensing location, we also considered an additional arbitrary sensing location by taking off the wrist band and re-attaching it again to the wrist at a random location such that the artery is between the electrode columns 2 and 4. The data was collected for 2 BP trials at the new sensing locations POS2, POS3, and Re-Attach which is enough data for testing the models that are trained for POS1.

During the experiment, the participant sits on a chair with his left arm on a bench at rest to minimize the effect of the motion artifacts on the Bio-Z and BP signals, and to keep the wrist at a constant height relative to the heart as shown in Figure 69(a). Before placing the wristband on the participant's wrist, we locate and mark the radial artery's location using Huntleigh Dopplex MD2 Bi-Directional Doppler which measures the velocity of blood flow using a high sensitivity probe. The mark of the radial artery is used to align the sensing location of the Bio-Z electrodes in the wrist band with the artery's location. The array band is placed on the wrist according to the initial sensing configuration POS1 which is based on electrode columns 2,3 and 4 with the center column 3 is aligned with the radial artery. In addition to the wrist-worn sensor array, we used the Finapres NOVA system, which continuously measures BP uses a finger pressure cuff placed on the middle finger of the left hand and automatically calibrated with the standard

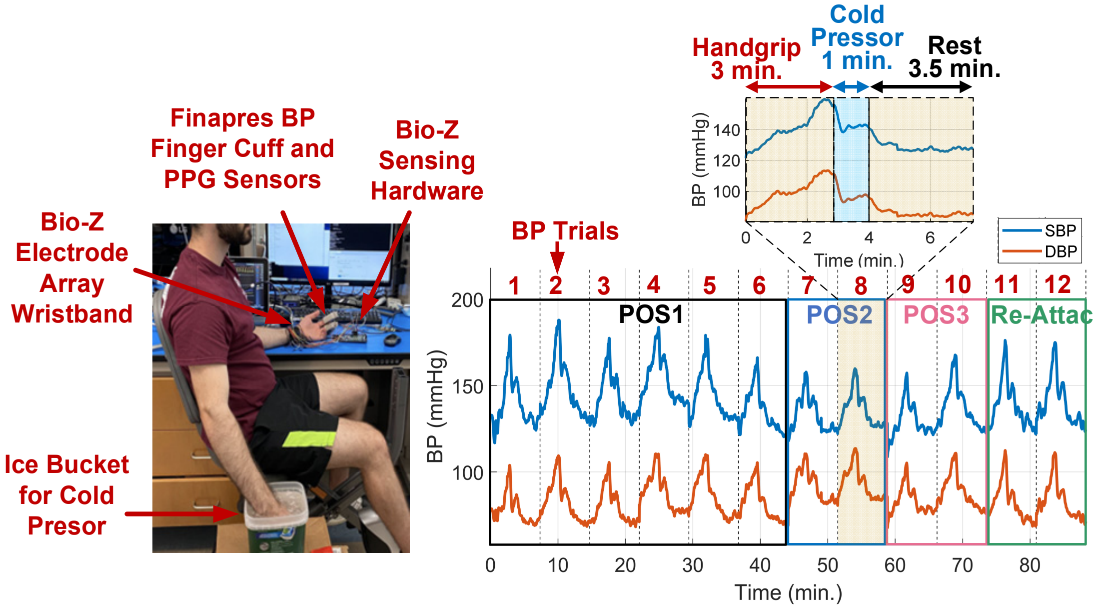

(a) (b)

Figure 69. (a) The data collection setup showing the participant placing his left arm on the bench with the attached Finapres BP finger cup, PPG finger clip and our Bio-Z electrode array wristband that is connected to our custom Bio-Z sensing hardware (Bio-Z XL) while the participant's right arm is placed in the ice bucket for the cold pressor that followed hand grip exercise using the same hand. (b)The systolic BP and diastolic BP change during around 90 minutes of the experiment of a single participant which includes 12 repeated trials to increase BP by 3 minutes of handgrip exercising, 1 minute of cold pressor test followed by 3.5 minutes at rest for BP recovery for each trial.

brachial pressure cuff. Finally, in order to avoid movement of the left hand which holds all the sensors, and therefore to prevent the motion artifacts and noise; the handgrip exercise and cold pressor tests are carried out using the right hand of the participant. The SBP and DBP readings are extracted from the maximum and minimum BP values at the peak and foot points of the reference BP signal for each heartbeat. The beat-to-beat SBP and DBP readings were smoothed by a moving average window of 20 heartbeats.

Each trial to change BP consists of 7.5 minutes. The trial starts by handgrip exercising for 3 minutes, followed by a cold pressor test for 1 minute by immersing the right hand in an ice water container, and ends by 3.5 minutes at rest. During each trial, starting from normal BP, an increase in BP occurs gradually with handgrip until it reaches its peak value by the end of the 3 minutes of the exercise. After that, BP starts to decrease and the cold pressor jumps in to slow down the drop in BP by trying to elevate the BP again. After that, the BP recovers back slowly to normal BP during the resting period as shown in Figure 69(b).

The choice of handgrip exercise compared to other exercising methods such as cycling or running on a treadmill provides a large enough BP increase of about 50 mmHg above normal BP with minimum wrist movements to decrease motion artifacts in the collected data. We chose the cold pressor test to follow handgrip exercise in order to include different physiological mechanisms of BP changes from exercising for more general BP models. Also, BP drops suddenly in healthy subjects after handgrip exercise; therefore, the cold pressor helps to keep BP high for a longer time. This is preferable in order to provide more data points at high BP for better training and testing of the BP models. The handgrip exercise and cold pressor test are the best BP maneuvers that can change BP with minimal increase in heart rate, so that the model is focused on BP changes rather than heart rate changes.

We collected Bio-Z and BP data from 4 participants over 12 BP trials with a total time of 90 minutes from 4 different sensing locations with around 6000 heartbeats from each participant. Furthermore, the SBP and DBP readings from the reference BP monitoring system were smoothed by a moving average window of 20 heartbeats.

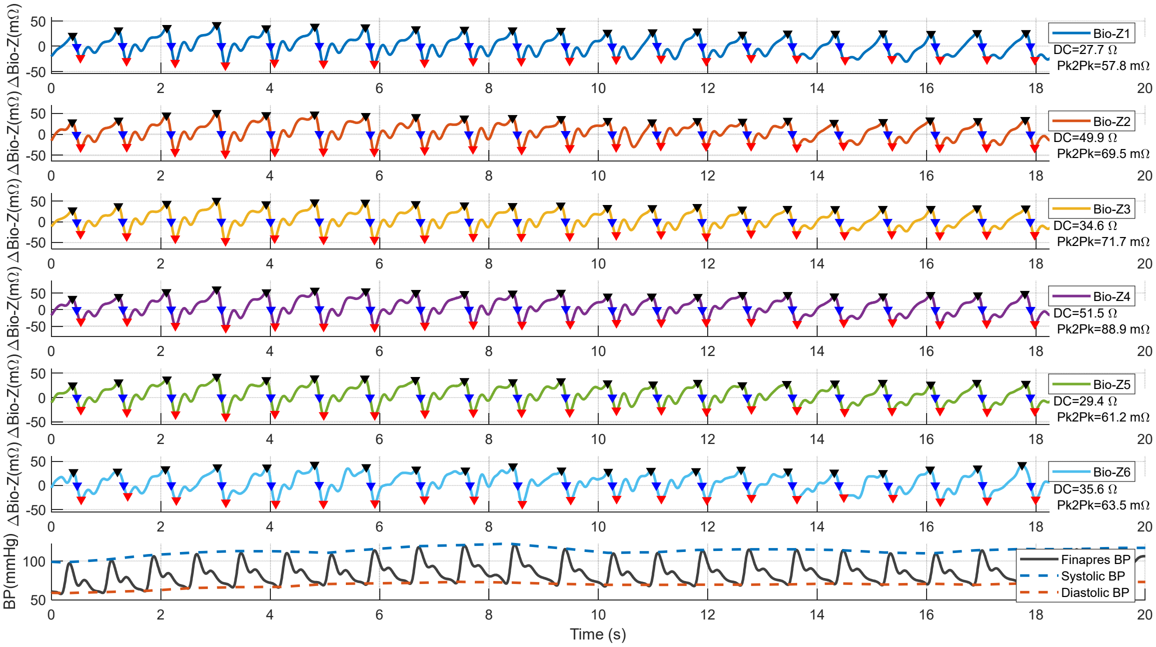

Figure 70. An example of the experimental data collected by the Bio-Z XL board and the electrode array wrist band for the 6 sensing locations at the wrist around the radial artery simultaneously with continuous BP signal from the reference Finapres BP device. The data illustrates the Bio-Z pulse signal (ΔBio-Z) after removing the DC component by the signal pre-processing algorithms and after characteristic points detection. The plot highlights the DIA peak (black), MS (blue) and SYS foot (red) points. The reference systolic and diastolic BP are shown as the interpolation of the peak and foot points of the continuous BP signal from Finapres.

Figure 70 shows an example of the experimental data collected by the Bio-Z XL board and the electrode array wrist band for the 6 Bio-Z channels at POS1 at the wrist around the radial artery. The data illustrates the high-quality Bio-Z pulse signal (ΔBio-Z) for all channels after removing the DC component of static tissue impedance by the signal pre-processing algorithms. The plot highlights the DIA peak (black), MS (blue) and SYS foot (red) points for each heartbeat that are estimated by the characteristic points detection algorithms with high accuracy and consistency for different pulse morphologies. The plot shows the average DC component and peak-to-peak value of the pulse (Pk2Pk) over 2.5 minutes time segment for each signal that varies from 27.4Ω to 43.5Ω and from 46.0mΩ to 120.7mΩ respectively. The largest signal occurs in the middle column at sensor 4 because of its alignment with the radial artery and the higher current density at the middle column. In addition, Figure 70 shows the reference BP signal from the Finapres device as measured simultaneously with the Bio-Z signals. The reference systolic and diastolic BP are shown for every heartbeat as the interpolation of the peak and foot points of the continuous BP signal from Finapres.

5.3.3.2. Pulse Morphology Variation with BP

The proposed method of this study relies on extracting the significant features in the blood pulsatile activity in the Bio-Z signals measured from the wrist arteries that are a function of BP and can be used as the input features for the BP regression models that are trained based on the subject pulsatile properties. In order to show the change of Bio-Z pulse morphology with BP, we categorized the Bio-Z pulses into 3 groups based on BP by dividing the range of mean arterial pressure (MAP) dataset into 3 equal BP ranges of high, moderate and low MAP. The Bio-Z pulse signal (ΔBio-Z) is inverted to be proportional to blood volume changes and divided into separate heartbeat segments at the diastolic (DIA) point. The timestamps of the pulse segment for each heartbeat are normalized with respect to the heartbeat time period. The amplitude of the pulse segment is normalized by considering the DIA point as zero amplitude and dividing the amplitude of the whole heartbeat amplitude by its peak point which is the systolic (SYS) point, so that the amplitude of all pulses varies in the range of 0 to 1. In order to get the mean of the pulses for each BP group, the pulse samples are aligned in time by resampling all the

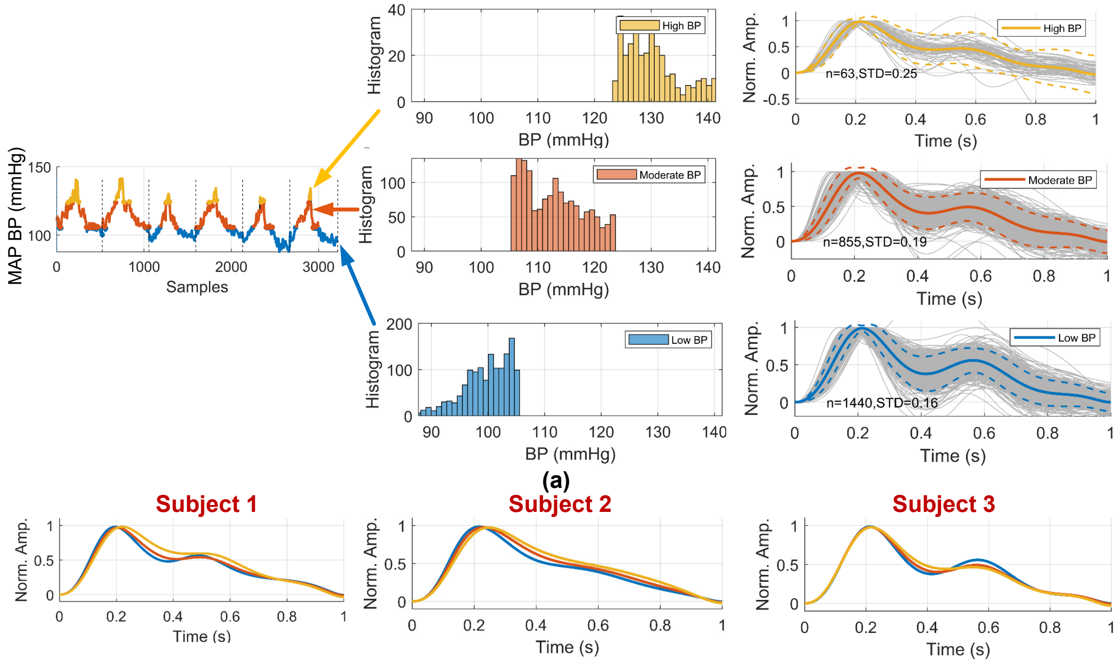

(a)

(b)

Figure 71. (a) The mean arterial pressure (MAP) of subject 1 is divided into 3 groups: low (less than 105 mmHg), moderate (from 105 to 125 mmHg) and high (above 125 mmHg) ranges showing the BP histogram for each group and the corresponding normalized Bio-Z pulses with the mean and 20 and 80 percentiles indicators. (b) The mean of bio-impedance pulses for each BP range for 3 different participants that show the variation of bio-impedance pulse morphology with BP and from one subject to another.

heartbeat segments at the same time samples. The resampling is done by linear interpolation to get the new time samples.

The mean pulse of each BP group is plotted in Figure 71(a). Also, the 20% and 80% percentiles of the pulses are plotted to show the spread of the pulses within each BP group. The mean pulse of the three BP groups to show the difference between pulse morphology over BP indicated by the change in the rising slope and the amplitude and time of the dicrotic notch that are used as our features for BP models to detect BP from Bio-Z signal. In addition, Figure 71(b) plots the mean pulse for three participants to show the same trend happens for different participants but with different pulse morphology for each participant. It demonstrates the importance of using personalized BP models to capture the differences in pulse morphology that changes with BP from one participant to another. Also, there is a significant change in pulses from beat to beat which can be solved by averaging the Bio-Z pulses through a moving average window over a number of heartbeats.

5.3.3.3. Arterial Pulse by CNN Autoencoder

The next step in the proposed algorithms towards BP prediction is the estimation of the arterial pulse signal from the 6 input ΔBio-Z signals using the CNN autoencoder algorithm. The output signal from the CNN autoencoder, defined as $\Delta\text{Bio-Z}_{AE}$, is the estimation of the pulsation in the radial artery based on filtering the input signals with CNN weights that are learned from the ΔBio-Z data and represent the transfer functions between pulsation in the artery to the sensors on the skin. An example of the CNN autoencoder output $\Delta\text{Bio-Z}_{AE}$ is shown in Figure 72 compared to the 6 input ΔBio-Z signals. The estimated signal has high-quality pulse morphology that is consistent over multiple beats and is considered as the accurate arterial pulse signal. The BP prediction with regression models relies on the features extracted from this estimated arterial pulse signal. The effectiveness of the proposed method in arterial pulse estimation is assessed by the improvement that occurs in BP estimation by this signal compared to the baseline method that relies on the raw input ΔBio-Z pulse signals.

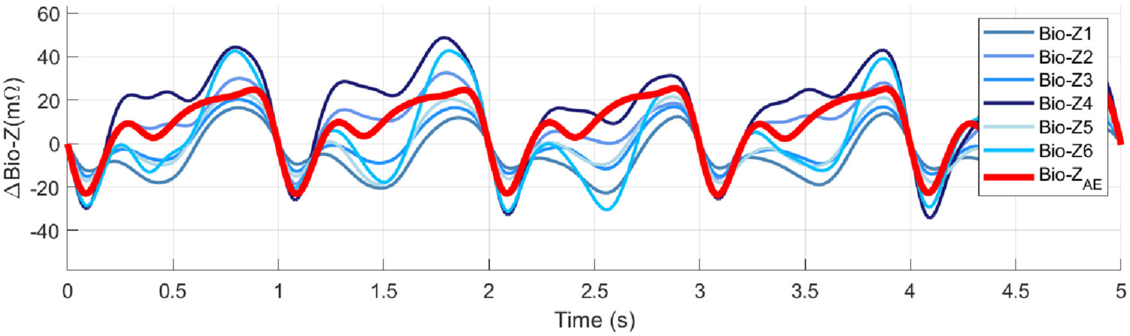

Figure 72. The plot of the CNN autoencoder output of radial artery's pulsation signal (ΔBio-Z_{AE} in red) which estimated from the input Bio-Z pulse signals (ΔBio-Z in blue) measured from different sensing locations at the wrist by learning the transfer function from the artery to each sensing location from the training data. The plot shows the high quality and consistency of the estimated arterial pulse signal compared to the input signals.

5.3.3.4. BP Models

The data were collected from 4 healthy participants using our developed wristband and sensing hardware and were captured over 12 consecutive BP trials of 7.5 minutes for each trial. As a result, the measurements were conducted over a total period of 90 minutes for each participant. The DBP and SBP were estimated using separate regression models based on the ensemble learning method of AdaBoost, which builds the prediction by combining several weak learners' outputs through a weighted sum of different subsets of the training data set. The BP AdaBoost model is trained by the BP features that are extracted from the wrist ΔBio-Z signals after processing with the CNN autoencoder. The ΔBio-Z signals are measured simultaneously with the reference BP signal measured from the Finapres BP reference device. We used subject-specific models that were trained for each subject based on the subject's data to capture the unique arterial properties for each individual. The performance of the models was evaluated using the BP root-mean-square error (RMSE), and correlation coefficient (R). We used three different training and testing methods to evaluate the BP prediction performance that varies in splitting the data between training and testing and the number of training iterations within each method as shown in Figure 73 and Table 20.

The first method of 20-fold cross-validation trains and tests the model using POS1 data only by splitting the data into 20 folds with 19 folds (95% of POS1 data) for training and 1 fold (5% of POS1 data) for testing. The 19 folds of training data are equivalent 5.7 BP trials or 42.75 min. of POS1 data. The testing data is continuous BP samples for about 70% of single BP trial or time segment of 2.25 min. of POS1 data that circulate for all the folds to cover the whole POS1 data and avoid the bias for training the model with a certain part of the data. The performance of this method is evaluated by the average of all 20 folds.

The second method evaluates the BP model performance for a longer continuous time segment of POS1 data by using leave one complete trial out cross-validation method. In this method, the POS1 data is splitted into 5 BP trials of POS1 data (37.5 min.) for training data and the remaining single BP trial of POS1 (7.5 min.) for the testing data. The

Table 20: The comparison of the training methods 20-fold cross-validation, leave one trial out and testing different location in terms of the used time segments, sensing location and autoencoder model.

BP Model Training/Testing Method	No. of Trained Models	Training Data				Testing Data			
		Time (min.)	Percentage of POS1 data	Location	AE Model	Time (min.)	Percentage of POS1 data	Location	AE Model
20-fold cross-validation	20	42.75	95%	POS1	AE1	2.25	5%	POS1	AE1
Leave on trial out	6	37.5	83.3%	POS1	AE1	7.5	16.7%	POS1	AE1
Testing different location	1	30	66.7%	POS1	AE1	15	33.3%	POS1	AE1
						15	33.3%	POS2	AE2
						15	33.3%	POS3	AE3
						15	33.3%	Re-Attach	AE4

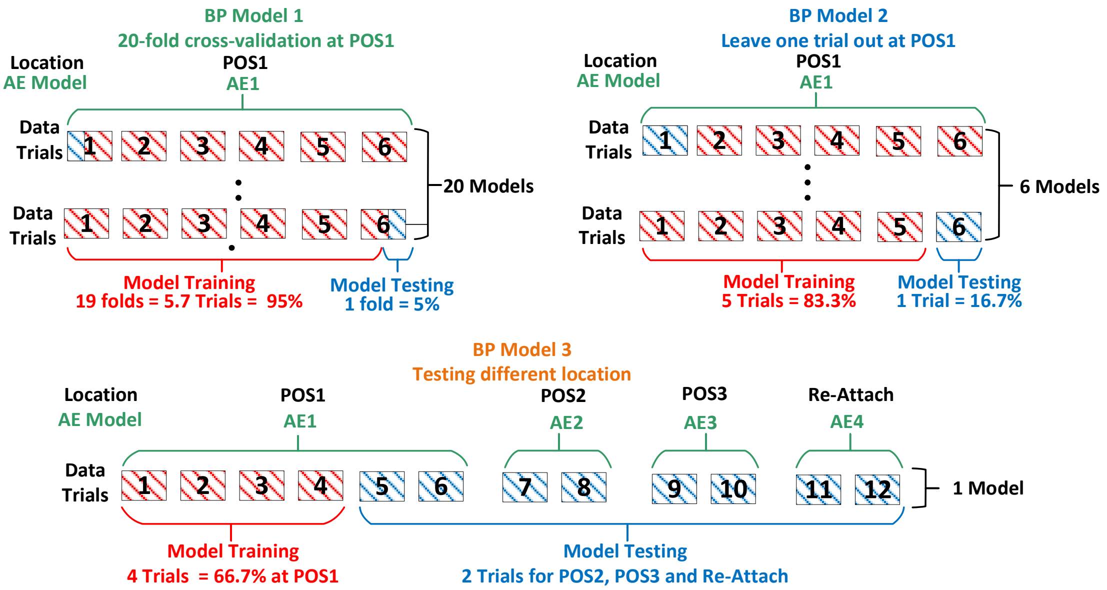

Figure 73. The visual illustration of the three training methods used in this work: 20-fold cross validation, leave one trial out and testing different location showing the split of the BP trials between training and testing data and the corresponding sensing locations and CNN autoencoder models.

BP trial used for testing data loops all the six BP trials of POS1 data and the performance of this method is evaluated by the average of the 6 testing BP trials.

The third method evaluates the BP performance for different sensing locations and for longer time segments by training the model with the first 4 BP trials of POS1 data (30 min.) and testing the model with the remaining 8 BP trials for the four locations (POS1, POS2, POS3 and Re-Attach) by taking the average of each 2 trial for each location which are 15 min. time segment. The arterial pulse signal (ΔBio-Z_{AE}) is estimated for each location by four separate CNN models denoted by AE1, AE2, AE3 and AE4 for the locations POS1, POS2, POS3 and Re-Attach respectively.

Table 21: The BP estimation performance using the proposed method with the 20-fold cross validation for each subject.

Subject	Number of Samples	DBP							SBP						
		RMSE (mmHg)	R	ME (mmHg)	BP Mean (mmHg)	BP Range (mmHg)	BP Min (mmHg)	BP Max (mmHg)	RMSE (mmHg)	R	ME (mmHg)	BP Mean (mmHg)	BP Range (mmHg)	BP Min (mmHg)	BP Max (mmHg)
1	3206	5.4	0.81	0.1	73.1	42.1	57.0	99.1	5.9	0.79	0.2	137.3	46.5	120.2	166.7
2	3483	4.4	0.80	0.0	77.9	37.0	66.0	103.0	5.8	0.76	-0.3	120.1	46.9	102.6	149.5
3	3121	4.5	0.91	0.3	83.0	42.8	67.7	110.5	7.1	0.86	0.2	138.3	63.7	116.8	180.5
4	2670	5.5	0.68	0.5	82.3	41.5	68.5	110.1	7.3	0.75	0.6	137.7	55.0	120.1	175.1
Average	3120	5.0	0.80	0.2	79.1	40.8	64.8	105.7	6.6	0.79	0.2	133.3	53.0	114.9	167.9
STD	292	0.5	0.08	0.2	4.0	2.3	4.6	4.8	0.7	0.04	0.3	7.6	7.0	7.3	11.7

The DBP and SBP values were predicted for 4 subjects by applying the proposed regression models based on the pulse signal estimated by the CNN autoencoder. The BP performance for each subject using the first training method of 20-fold cross-validation is numerically presented in Table 21 and graphically illustrated in Figure 74. The proposed

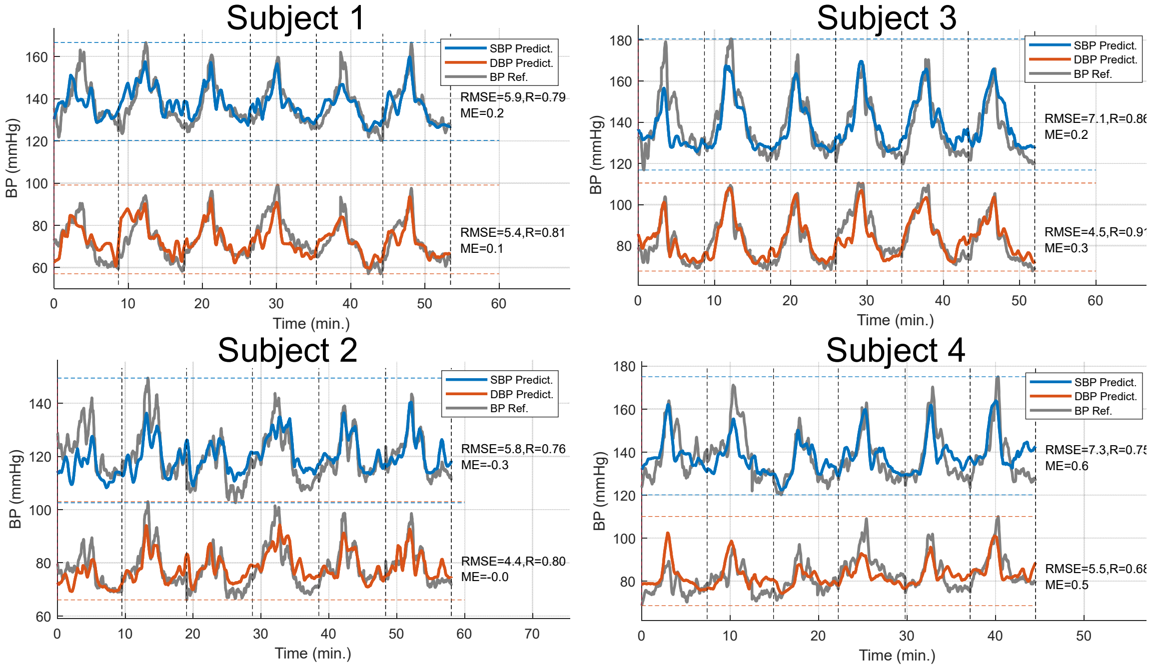

Figure 74. The plot of SBP (blue) and DBP (orange) predictions versus reference BP from Finapres (gray) over time for each subject for the first 6 BP trials (BP trials from 1 to 6) of POS1 using the proposed method with 20-fold cross validation.

method is tested for extreme BP values by introducing large changes in each subject BP using handgrip exercising followed by cold pressor. The DBP varies across the 4 subjects with an average range of 40.8 mmHg between a minimum and maximum values of 64.8 mmHg and 105.7 mmHg with STD of 2.3 mmHg, 4.6 mmHg and 4.8 mmHg, respectively. While the SBP varies with an average range of 53.0 mmHg between a minimum and maximum values of 114.9 mmHg and 167.9 mmHg with STD of 7.0 mmHg, 7.3 mmHg and 11.7 mmHg, respectively. The average BP performance using 20-fold cross-validation for the DBP is illustrated by an average RMSE of 5.0 mmHg and a substantial average correlation coefficient of 0.80 with respective insignificant STDs of 0.5 mmHg and 0.08 demonstrate high accuracy estimation of the DBP from bio-impedance features in comparison with the DBP acquired by the reference BP monitoring system. In addition, an average of the mean error (ME) of 0.2 mmHg shows the precision in BP estimation by our developed wrist-worn sensor array.

On the other side, an average RMSE of 6.6 mmHg with an average correlation coefficient of 0.79 and respective STDs of 0.7 mmHg and 0.04 were estimated for the SBP. In addition, the mapping algorithm resulted in an average BP mean value of 133.3 mmHg and an average ME of -0.2 mmHg with STD of 7.6 mmHg and 0.3 mmHg, respectively. Figure 74 shows the estimated SBP and DBP plotted in comparison to the reference BP for the study participants for the time duration of 45 min. of POS1 data. The insignificant values of RMSE and ME along with the remarkable correlation coefficient illustrates consistency between the predicted SBP and DBP values and the reference BP measurements.

In addition, the breakdown of the contribution of all steps in the proposed algorithm including using AE only, AE with adding new features and finally adding the BP averaging are compared with the baseline method for 20-fold cross-validation as shown in Table 22. The performance of DBP and SBP estimation with the proposed method is compared by the baseline method. The baseline performance is calculated from the average of the two sensors in the middle electrode column which have the largest pulse signals and best performance among all the electrode columns. The proposed method with 20-fold cross-validation shows significant improvement in RMSE and correlation coefficient and each step in the proposed method is partially responsible for this improvement. For the 20-fold cross-validation method, using CNN autoencoder causes BP to improve compared to the baseline from 6.6 mmHg and 0.64 to 6.0 mmHg and 0.71 for the DBP and from 9.0 mmHg and 0.57 to 8.1 mmHg and 0.67 for the SBP. Using new proposed features with CNN autoencoder causes BP to improve to 5.7 mmHg and 0.74 for the DBP and 7.5 mmHg and 0.73 for the SBP. Finally using the complete proposed method by adding the BP averaging cause BP performance to achieve its maximum of 5.0 mmHg and 0.80 for the DBP and 6.6 mmHg and 0.79 for the SBP.

Table 22: The average BP estimation performance for all subjects using the 20-fold cross validation and the proposed method compared to the baseline method.

The Method	**DBP**		**SBP**	
	RMSE (mmHg)	**R**	**RMSE (mmHg)**	**R**
Baseline	**6.6**	**0.64**	**9.0**	**0.57**
AE	**6.0**	**0.71**	**8.1**	**0.67**
AE + New features	**5.7**	**0.74**	**7.5**	**0.73**
The Proposed Method (AE + New features + BP avg.)	**5.0**	**0.80**	**6.6**	**0.79**

Table 23: The subject average BP estimation performance for the leave one trial out cross validation using the proposed method compared to the baseline method.

The Method	**DBP**		**SBP**	
	RMSE (mmHg)	**R**	**RMSE (mmHg)**	**R**
Baseline	**6.8**	**0.63**	**9.1**	**0.57**
AE	**6.3**	**0.67**	**8.2**	**0.66**
AE + New features	**5.9**	**0.72**	**7.8**	**0.71**
The Proposed Method (AE + New features + BP avg.)	**5.2**	**0.77**	**6.9**	**0.76**

The training method of leave one trial out shows the effect of decreasing the training data and increasing the testing data to one complete trial. The BP performance of the proposed method using leave on trial out is shown in Table 23. The RMSE and

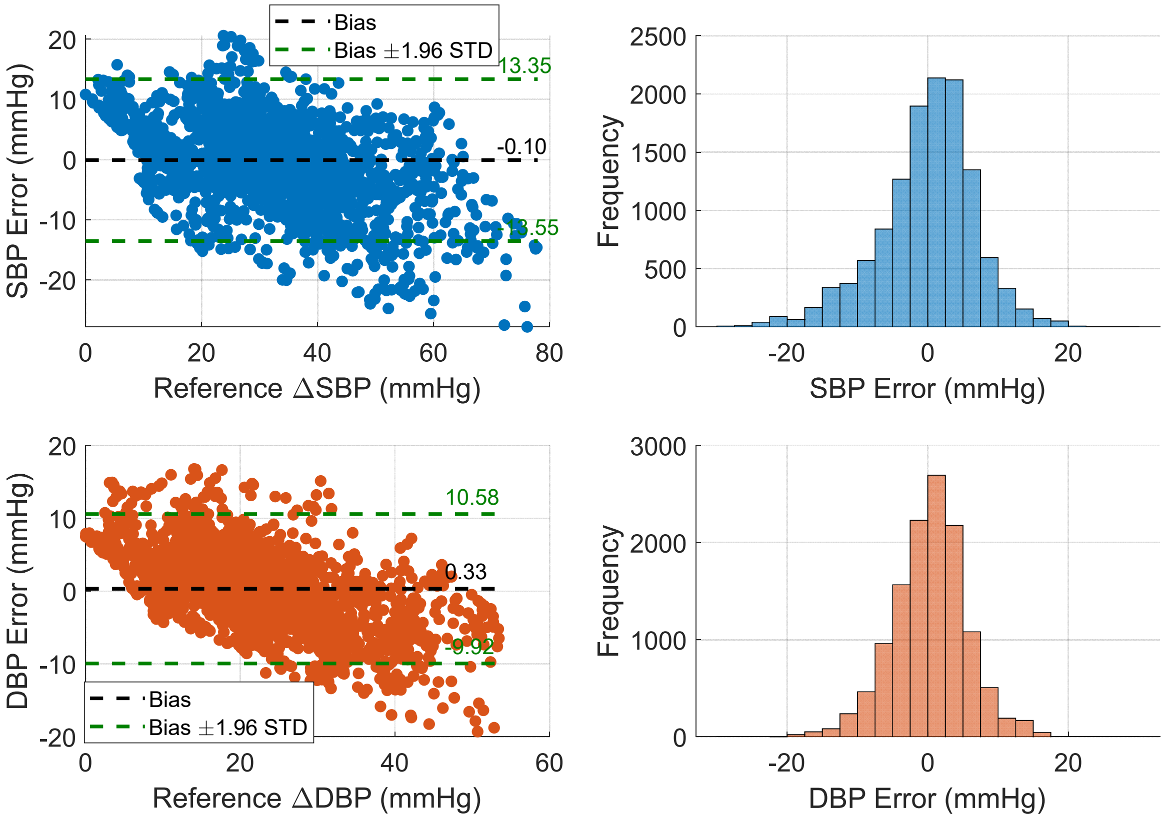

Figure 75. The plot of SBP (blue) and DBP (orange) predictions versus reference BP from Finapres (gray) over time for each subject for the first 6 BP trials (BP trials from 1 to 6) of POS1 using the proposed method with 20-fold cross validation.

Table 24: The DBP and SBP error distribution for the three BP error ranges under the thresholds 5 mmHg, 10 mmHg and 15 mmHg according to BHS standard for the leave one trial out cross validation using the proposed method.

		≤5 mmHg	**≤10 mmHg**	**≤15 mmHg**
Our Result	**DBP**	**69%**	**94%**	**99%**
	SBP	**60%**	**86%**	**96%**
BHS	**Grade A**	**60%**	**85%**	**95%**
	Grade B	**50%**	**75%**	**90%**
	Grade C	**40%**	**65%**	**85%**

correlation coefficient is 5.2 mmHg and 0.77 for the DBP and 6.9 mmHg and 0.76 for the SBP with only slight degradation compared to the 20-fold cross-validation method.

For the proposed method with leave one trial out cross validation, the BP error scatter plot and histograms for SBP and DBP are plotted in Figure 75 showing the small mean error of 0.33 and -0.1 mmHg for DBP and SBP respectively. The figure shows the DBP error range from -20 to 18 mmHg and for SBP error is from -25 to 20 mmHg with the majority of error lies around zero error. The DBP and SBP error distribution for the three BP error ranges under the thresholds 5 mmHg, 10 mmHg and 15 mmHg are shown in Table 24 according to the British Hypertension Society (BHS) standard [71]. The results in the table show the BP performance is consistent with grade A in BHS standard for both DBP and SBP.

The BP performance of the last method of testing on different locations using the proposed method compared to the baseline method is shown in Table 25. The third training method shows the effectiveness of the proposed method when training the model on POS1 data and testing the model on other positions POS2, POS3 and Re-attach. The baseline method has the best performance when the model is trained and tested on the same location

Table 25: The subject average BP estimation performance using the proposed method compared to the baseline method for different locations.

Testing Location		Baseline				Proposed Method			
		DBP		SBP		DBP		SBP	
		RMSE (mmHg)	R	RMSE (mmHg)	R	RMSE (mmHg)	R	RMSE (mmHg)	R
Same Location	**POS1**	**7.2**	**0.67**	**8.2**	**0.64**	**5.8**	**0.79**	**6.2**	**0.85**
Diferent Location	**POS2**	**8.9**	**0.56**	**10.2**	**0.52**	**6.8**	**0.74**	**8.9**	**0.67**
	POS3	**8.8**	**0.46**	**12.3**	**0.43**	**7.1**	**0.75**	**11.5**	**0.67**
	Re-Attach	**10.6**	**0.49**	**11.7**	**0.47**	**8.2**	**0.68**	**10.3**	**0.52**
	Average	**9.4**	**0.50**	**11.4**	**0.47**	**7.4**	**0.72**	**10.2**	**0.62**

of POS1 which is RMSE and correlation coefficient of 7.2 mmHg and 0.67 for DBP and 8.2 mmHg and 0.64 for SBP. The baseline method performs poorly when tested on different locations with RMSE and correlation coefficient of 9.4 mmHg and 0.50 for DBP and 11.4 mmHg and 0.47 for SBP for the average of the three locations. The proposed method improves the BP performance at different locations by RMSE and correlation coefficient of 7.4 mmHg and 0.72 for DBP and 10.2 mmHg and 0.62 for SBP with an average improvement of 34.1% in correlation coefficient and 15.9% in RMSE compared to the baseline method at different locations. The BP performance of the proposed method at different locations is close to the baseline method at the same location of POS1 by a factor of 92%. The degradation in BP performance in this case compared to the 20-fold cross-validation and the leave on trial out due to the reduction in the training data from 95% and 83.3% to 66.7% of POS1 data and the increase in the testing time segment from 2.25 min. and 7.5 min. to 15 min.

5.3.4. Discussion

In this study, we demonstrated the feasibility and effectiveness of predicting systolic and diastolic BP values from the bio-impedance signals detected from the wrist's radial artery. The signals are acquired through a non-invasive cuffless wristband with a flexible sensor array. Bio-impedance sensing is a safe and promising technique which unlike the PPG optical sensing, presents substantial penetration depth to detect the arterial pulsation on the wrist. In order to translate the bio-impedance data to BP, a CNN autoencoder algorithm was proposed to estimate the arterial pulse signal from the input six Bio-Z signals measured from the wrist. In addition, a mapping algorithm based on a subject-specific AdaBoost regression model was developed and trained by the bio-impedance features extracted from the estimated pulse signal. The extracted features represent the arterial pulse morphology and is substantially dependent on the cardiac activity and the vascular properties of ulnar and radial arteries; therefore, are highly correlated with BP.

An important aspect of the developed wrist-worn sensor array is that it is built based on dry electrodes. Conventional Ag/ AgCl wet electrodes reduce the wearability of the wristband, and besides, as the conductive gel of the wet electrodes dries over time, the electrode-skin impedance increases drastically. This in turn, affects the amplitude of the applied current signal. Consequently, instead of injecting a sinusoidal signal with specific frequency and amplitude to the wrist skin, a saturated wave across the voltage sensing electrodes will be measured. The proposed wristband developed based on dry silver electrodes provides an electrode-skin impedance with minimum fluctuations over time and ensures the detection of arterial pulse with excellent signal quality and high SNR ratio. As a result, they provide the bio-impedance data collection, continuously and consistently in long term. The long-term and continuous reading of BP opens a new horizon in the prognosis and prevention of cardiovascular disorders and diseases, and potentially impacts the mortality rate of CVDs. Furthermore, the wristband was developed based on a configurable electrode array of 6×8 nodes. Our approach was to make it practical to configure which nodes to be utilized for current injection and voltage sensing functions over the array. Therefore, regarding the location of the radial artery on the wrist, different pairs of electrodes for bio-impedance signal detection can be selected. While the configurability of the electrode array improves the flexibility of the sensing system, the feature can be utilized for smart and automatic localization of the arteries, too.

The proposed cuffless BP system was shown its effectiveness in predicting BP for continuous-time segments up to 15 min. and for large BP changes up to 53.0 mmHg with acceptable accuracy. The BP prediction methods were reliable for two different types of BP maneuvers which are exercising and cold pressor. In addition, the effect of changing the sensing location on the BP prediction performance was shown for the first time and we were able to improve the results by 34.1% in correlation coefficient and 15.9% in RMSE by using our proposed methods of CNN autoencoder to estimate the arterial pulsation independent on the location in addition to the proposed new features and BP averaging technique. For additional improvements for the BP predictions, the sensor array can be extended to add the signals from the ulnar artery to the current signals from the radial artery. We only used 3 columns from the 8 columns of the sensor array in our wristband. Additional 3 columns can be used around the ulnar artery to utilize the full array band and to generate an estimation of the arterial pulse at the ulnar artery. Adding the features extracted from the ulnar pulse signal to the BP regression models will improve the BP performance and decrease the error. The results show that the BP performance improves by increasing the size of the training data which helps in achieving more accurate weights for the regression models and the CNN autoencoder. Therefore, further improvements can be achieved in BP predictions by increasing the number of BP trials for model training with larger BP ranges to improve the accuracy of BP models.

One particular requirement for the context-aware cuffless BP monitoring system based on bio-impedance sensor array is that a specific data interpretation model for each subject needs to be developed. In fact, since the vascular properties of ulnar and radial arteries vary from one subject to another, a general model cannot be utilized. To illustrate the variance in the arterial pulse morphologies among the participants, the MAP as a variable which is determined by the subject-specific cardiac output and vascular resistance was investigated in this study. As shown in Figure 71(b), the mean values of bio-impedance pulses for different subjects show the variation of bio-impedance pulse morphology with BP from one subject to another. Therefore, a regression model based on AdaBoost technique was used for each participant. AdaBoost showed a higher correlation coefficient between the estimated and the reference BP and a lower RMSE in comparison with the Support Vector, Random Forest, Linear, Gradient Boosting, and Decision Tree regression models [1]. Since mapping the bio-impedance features to BP values is a nonlinear problem, the AdaBoost algorithm provides the most accurate results.

Another requirement for the developed system to estimate SBP and DBP values from bio-impedance data is simultaneous and continuous BP monitoring by a reference device on every heartbeat. Since the proposed data training model is subject-specific, a solid and reliable BP reference reading is inevitable. With respect to this requirement, we used Finapres NOVA system, which uses the standard brachial pressure cuff for self-calibration and continuously measures BP using a finger pressure cuff placed on the middle finger. The Finapres reference system has the U.S. Food and Drug Administration (FDA) approval and besides, has received significant attention as a reference device for continuous BP measurements [1, 17, 65, 67].

The time length of bio-impedance data collection has a direct impact on the data optimization process and the accuracy of BP estimation from the extracted characteristic points. In other words, longer data collection will increase the correlation coefficient between the estimated and the measured BP and will decrease the RMSE between them. Another significance of long-term data collection is the feasibility of training data based on deep neural network (DNN) algorithms. DNN is a multilayer neural network with the objective of learning from the extensive amount of data and identifying patterns towards making decisions. As a result, it can add artificial intelligence to the training model. In the particular case of our research, DNN can obtain the knowledge underneath BP and replace subject-specific models and features with a generalized model. Therefore, the requirement of training data based on a personalized model will be dropped. Our current hardware system does not have a wearable form factor and best-case scenario, the time length of collected data will be limited to a few hours. Therefore, in order to facilitate long-term bio-impedance data collection and to continuously read BP, a wearable system with the form factor of a smart watch needs to be implemented. Such a system can acquire the required amount of data as the input to a new training model based on DNN and as a result, a generalized model for mapping bio-impedance extracted features to BP values can be investigated.

5.4. Conclusions

In this chapter, we introduced the multi-source multi-frequency bio-impedance measurement method that provides localized pulse signal sensing. The results showed the effectiveness of the multi-frequency Bio-Z measurement method compared to the single-frequency method by measuring pulse signals with lower IBI error and larger PTT values. The proposed method of localized current injection for each sensing location improves the accuracy of BP feature extraction and estimation results. In addition, we estimated BP with calibration-free method for sensing location based on CNN autoencoder that can reconstruct the arterial pulse wave from multiple Bio-Z pulse signals. The reconstructed pulse signal is consistent at different locations which provide more reliable and accurate BP independent of sensing location relative to the arteries. Based on experimental data of 6 hours of BP data from 4 subjects, the proposed method showed less BP error at all sensing locations by improving the correlation coefficient by 34.1% compared to the original method of using a single pulse signal.

6. CONCLUSIONS

In this dissertation, we presented a new method for cuffless blood pressure monitoring from the wrist using an array of bio-impedance (Bio-Z) sensors.

In chapter 2, we presented the design of the proposed custom Bio-Z sensing board (Bio-Z XL) including the circuits and the signal processing algorithms that provide multi-channel measurements of Bio-Z pulse signals with a resolution of 1 mΩ. The sensing hardware can provide current amplitude up to 1 mA and frequency up to 22 kHz. The Bio-Z signal pre-processing is shown including filtering, demodulation, DC removal, and the characteristic points detection algorithms. The design of a custom electrode array wristband is presented that includes 6×8 small size silver electrodes that provide flexible Bio-Z sensing configuration by the connection with the Bio-Z XL board.

In chapter 3, we proposed a Bio-Z simulation platform using a 3D grid of the time-varying impedance voxels to model the tissue and pulse wave in the arteries by simulations in the SPICE environment in parallel with the sensing circuits. The proposed methods modeled the propagation of current through the small elements in the grid and the distribution of voltage at each node including the DC voltage of tissue and pulse signal from blood flow. The model was validated against Bio-Z measurements for the effect of different electrode locations relative to the artery, current frequency injection, and electrode size on the sensed pulse signal. The proposed method was used to quantify the penetration of the bio-impedance signals inside the tissue for different arterial depths. The proposed simulation platform can serve as an important tool to understand the propagation of pulse wave in the tissue and to improve Bio-Z sensing methods for measuring hemodynamic parameters and guide circuit designers and algorithm developers.

In chapter 4, we showed a proof-of-concept of our cuffless BP estimation methods from an array of Bio-Z sensors. Two pairs of sensors were placed on the radial and ulnar arteries of the wrist to capture the vascular properties of the two arteries. We showed our low noise circuits for accurate bio-impedance sensing from the wrist. Systolic and diastolic blood pressure were measured using AdaBoost regression model based on different features extracted from the bio-impedance signals. In this pilot study, data was collected from 10 human subjects after exercising to evaluate the performance of our method for post-exercise BP variations. The results showed a large correlation coefficient and small root mean square error of 2.6 and 3.4 mmHg for diastolic and systolic blood pressure respectively. Leveraging window-based features and an array of sensors provided a smaller error compared to using sample-based features and a pair of sensors on only one artery.

In chapter 5, we introduced novel Bio-Z sensing methods to improve PTT and BP monitoring. We presented the multi-source multi-frequency bio-impedance measurement method that provides localized pulse signal sensing. The results showed the effectiveness of the multi-frequency Bio-Z measurement method compared to the single-frequency method by measuring pulse signals with lower IBI error and larger PTT values. The proposed method of localized current injection for each sensing location improves the accuracy of BP feature extraction and estimation results. In addition, we estimated BP with calibration-free method for sensing location based on CNN autoencoder that can reconstruct the arterial pulse wave from multiple Bio-Z pulse signals. The reconstructed pulse signal is consistent at different locations which provides more reliable and accurate BP independent of sensing location relative to the arteries. Based on experimental data of 6 hours of BP data from 4 subjects, the proposed method showed less BP error at all sensing locations by improving the correlation coefficient by 34.1% compared to the original method of using a single pulse signal.

In this dissertation, we proposed new methods for continuous monitoring of hemodynamic parameters such as blood pressure in a comfortable form factor such as smart watches, which can contribute to more effective monitoring and management of the cardiovascular disease.

REFERENCES

[1] B. Ibrahim and R. Jafari, "Cuffless Blood Pressure Monitoring from an Array of Wrist Bio-Impedance Sensors Using Subject-Specific Regression Models: Proof of Concept," *IEEE transactions on biomedical circuits and systems,* vol. 13, no. 6, pp. 1723-1735, 2019.

[2] B. Ibrahim, A. Talukder, and R. Jafari, "Multi-source Multi-frequency Bio-impedance Measurement Method for Localized Pulse Wave Monitoring," in *2020 42nd Annual International Conference of the IEEE Engineering in Medicine & Biology Society (EMBC)*, 2020: IEEE, pp. 3945-3948.

[3] B. Ibrahim, D. A. Hall, and R. Jafari, "Pulse Wave Modeling Using Bio-Impedance Simulation Platform Based on a 3D Time-Varying Circuit Model," *IEEE Transactions on Biomedical Circuits and Systems,* vol. 15, no. 1, pp. 143-158, 2021.

[4] M. Kachuee, M. M. Kiani, H. Mohammadzade, and M. Shabany, "Cuffless Blood Pressure Estimation Algorithms for Continuous Health-Care Monitoring," *IEEE Trans Biomed Eng,* vol. 64, no. 4, pp. 859-869, Apr 2017, doi: 10.1109/TBME.2016.2580904.

[5] F. Miao *et al.*, "A Novel Continuous Blood Pressure Estimation Approach Based on Data Mining Techniques," *IEEE J Biomed Health Inform,* Apr 28 2017, doi: 10.1109/JBHI.2017.2691715.

[6] T. H. Huynh, R. Jafari, and W. Y. Chung, "An Accurate Bioimpedance Measurement System for Blood Pressure Monitoring," *Sensors (Basel, Switzerland),* vol. 18, no. 7, 2018.

[7] C. Poon and Y. T. Zhang, "Cuff-less and noninvasive measurements of arterial blood pressure by pulse transit time," in *Engineering in Medicine and Biology Society, 2005. IEEE-EMBS 2005. 27th Annual International Conference of the*, 2006, pp. 5877-5880.

[8] C. Vlachopoulos, M. O'Rourke, and W. W. Nichols, *McDonald's blood flow in arteries: theoretical, experimental and clinical principles*. CRC press, 2011.

[9] T. K. Bera, "Bioelectrical Impedance Methods for Noninvasive Health Monitoring: A Review," *J Med Eng,* vol. 2014, p. 381251, 2014, doi: 10.1155/2014/381251.

[10] M. c. Cho, J. Y. Kim, and S. Cho, "A Bio-Impedance Measurement System for Portable Monitoring of Heart Rate and Pulse Wave Velocity Using Small Body Area," vol. 1, pp. 3106-3109, 2009.

[11] P. Su, X. R. Ding, Y. T. Zhang, J. Liu, F. Miao, and N. Zhao, "Long-term blood pressure prediction with deep recurrent neural networks," in *Biomedical & Health Informatics (BHI), 2018 IEEE EMBS International Conference on*, 2018, pp. 323-328.

[12] F. Miao, Z. Liu, J. Liu, B. Wen, and Y. Li, "Multi-sensor Fusion Approach for Cuff-less Blood Pressure Measurement," *IEEE journal of biomedical and health informatics,* 2019.

[13] J. Muehlsteff, X. Aubert, and M. Schuett, "Cuffless estimation of systolic blood pressure for short effort bicycle tests: the prominent role of the pre-ejection period," in *Engineering in Medicine and Biology Society, 2006. EMBS'06. 28th Annual International Conference of the IEEE*, 2006, pp. 5088-5092.

[14] S. S. Thomas, V. Nathan, C. Zong, K. Soundarapandian, X. Shi, and R. Jafari, "BioWatch: A Noninvasive Wrist-Based Blood Pressure Monitor That Incorporates Training Techniques for Posture and Subject Variability," *IEEE Journal of Biomedical and Health Informatics,* vol. 20, pp. 1291-1300, 2016, doi: 10.1109/JBHI.2015.2458779.

[15] A. M. Carek, J. Conant, A. Joshi, H. Kang, and O. T. Inan, "SeismoWatch: Wearable Cuffless Blood Pressure Monitoring Using Pulse Transit Time," *Proceedings of the ACM on Interactive, Mobile, Wearable and Ubiquitous Technologies,* 2017.

[16] Y. Wang, Z. Liu, and S. Ma, "Cuff-less blood pressure measurement from dual-channel photoplethysmographic signals via peripheral pulse transit time with singular spectrum analysis," *Physiological measurement,* vol. 39, no. 2, p. 025010, 2018.

[17] A. Chandrasekhar, C. S. Kim, M. Naji, K. Natarajan, J. O. Hahn, and R. Mukkamala, "Smartphone-based blood pressure monitoring via the oscillometric finger-pressing method," *Science translational medicine,* vol. 10, no. 431, p. eaap8674, 2018.

[18] J. Liu, B. P. Yan, Y.-T. Zhang, X.-R. Ding, P. Su, and N. Zhao, "Multi-wavelength photoplethysmography enabling continuous blood pressure measurement with compact wearable electronics," *IEEE Transactions on Biomedical Engineering,* vol. 66, no. 6, pp. 1514-1525, 2018.

[19] N. Luo *et al.*, "Flexible piezoresistive sensor patch enabling ultralow power cuffless blood pressure measurement," *Advanced Functional Materials,* vol. 26, no. 8, pp. 1178-1187, 2016.

[20] C. Wang *et al.*, "Monitoring of the central blood pressure waveform via a conformal ultrasonic device," *Nature biomedical engineering,* vol. 2, no. 9, p. 687, 2018.

[21] B. Ibrahim and R. Jafari, "Continuous Blood Pressure Monitoring using Wrist-worn Bio-impedance Sensors with Wet Electrodes," in *2018 IEEE Biomedical Circuits and Systems Conference (BioCAS)*, 2018, pp. 1-4.

[22] B. Ibrahim, D. A. Hall, and R. Jafari, "Bio-impedance spectroscopy (BIS) measurement system for wearable devices," in *Biomedical Circuits and Systems Conference (BioCAS), 2017 IEEE*, 2017: IEEE, pp. 1-4.

[23] B. Ibrahim, D. A. Hall, and R. Jafari, "Bio-impedance Simulation Platform using 3D Time-Varying Impedance Grid for Arterial Pulse Wave Modeling," in *2019 IEEE Biomedical Circuits and Systems Conference (BioCAS)*, 2019: IEEE, pp. 1-4.

[24] B. Ibrahim, A. Akbari, and R. Jafari, "A novel method for pulse transit time estimation using wrist bio-impedance sensing based on a regression model," in

Biomedical Circuits and Systems Conference (BioCAS), 2017 IEEE, 2017, pp. 1-4.

[25] B. Ibrahim, V. Nathan, and R. Jafari, "Exploration and validation of alternate sensing methods for wearable continuous pulse transit time measurement using optical and bioimpedance modalities," in *Engineering in Medicine and Biology Society (EMBC), 2017 39th Annual International Conference of the IEEE*, 2017: IEEE, pp. 2051-2055.

[26] F. Simini and P. Bertemes-Filho, *Bioimpedance in biomedical applications and research*. Springer, 2018.

[27] S. Gabriel, R. Lau, and C. Gabriel, "The dielectric properties of biological tissues: III. Parametric models for the dielectric spectrum of tissues," *Physics in medicine & biology,* vol. 41, no. 11, p. 2271, 1996.

[28] J. R. Matthie, "Bioimpedance measurements of human body composition: critical analysis and outlook," *Expert review of medical devices,* vol. 5, no. 2, pp. 239-261, 2008.

[29] T. K. Bera, "Bioelectrical impedance methods for noninvasive health monitoring: a review," *Journal of medical engineering,* vol. 2014, 2014.

[30] "Medical electrical equipment, Part 1: General requirements for basic safety and essential performance, ANSI/AAMI ES60601-1:2005/A1:2012," in "ANSI/AAMI ES60601-1:2005/A1:2012," ANSI/AAMI ES60601-1:2005/A1:2012, ANSI/AAMI ES60601-1:2005/A1:2012.

[31] J. G. Webster, *Medical instrumentation: application and design*. John Wiley & Sons, 2009.

[32] S. S. Thomas, V. Nathan, C. Zong, K. Soundarapandian, X. Shi, and R. Jafari, "BioWatch: A noninvasive wrist-based blood pressure monitor that incorporates training techniques for posture and subject variability," *IEEE journal of biomedical and health informatics,* vol. 20, no. 5, pp. 1291-1300, 2016.

[33] M. Garbarino, M. Lai, S. Tognetti, R. Picard, and D. Bender, "Empatica E3 - A wearable wireless multi-sensor device for real-time computerized biofeedback and data acquisition," 2014, doi: 10.4108/icst.mobihealth.2014.257418.

[34] Y. Zhang, R. Xiao, and C. Harrison, "Advancing hand gesture recognition with high resolution electrical impedance tomography," in *Proceedings of the 29th Annual Symposium on User Interface Software and Technology*, 2016: ACM, pp. 843-850.

[35] A. Pantelopoulos and N. G. Bourbakis, "A Survey on Wearable Sensor-Based Systems for Health Monitoring and Prognosis," *IEEE Transactions on Systems, Man, and Cybernetics, Part C (Applications and Reviews),* vol. 40, no. 1, pp. 1-12, 2010, doi: 10.1109/tsmcc.2009.2032660.

[36] S. Majumder, T. Mondal, and M. J. Deen, "Wearable Sensors for Remote Health Monitoring," *Sensors (Basel),* vol. 17, no. 1, Jan 12 2017, doi: 10.3390/s17010130.

[37] B. Ibrahim, R. Jafari, and A. Akbari, "A Novel Method for Pulse Transit Time Estimation Using Wrist Bio-Impedance Sensing Based on a Regression Model," *2017 IEEE Biomedical Circuits and Systems (BioCAS),* 2017.

[38] Y. L. Zheng *et al.*, "Unobtrusive sensing and wearable devices for health informatics," *IEEE Trans Biomed Eng,* vol. 61, no. 5, pp. 1538-54, May 2014, doi: 10.1109/TBME.2014.2309951.

[39] S. Björklund *et al.*, "Skin membrane electrical impedance properties under the influence of a varying water gradient," *Biophysical journal,* vol. 104, no. 12, pp. 2639-2650, 2013.

[40] R. Mukkamala *et al.*, "Toward ubiquitous blood pressure monitoring via pulse transit time: theory and practice," *IEEE Transactions on Biomedical Engineering,* vol. 62, no. 8, pp. 1879-1901, 2015.

[41] M.-C. Cho, J.-Y. Kim, and S. Cho, "A bio-impedance measurement system for portable monitoring of heart rate and pulse wave velocity using small body area," in *2009 IEEE International Symposium on Circuits and Systems*, 2009: IEEE, pp. 3106-3109.

[42] B. Ibrahim, D. A. Hall, and R. Jafari. "BioZPulse Simulation Platform." http://www.github.com/TAMU-ESP/BioZPulse-Sim-Platform (accessed 2019).

[43] P. Avci *et al.*, "Low-level laser (light) therapy (LLLT) in skin: stimulating, healing, restoring," in *Seminars in cutaneous medicine and surgery*, 2013, vol. 32, no. 1: NIH Public Access, p. 41.

[44] J. Olsen, J. Holmes, and G. B. Jemec, "Advances in optical coherence tomography in dermatology—a review," *Journal of biomedical optics,* vol. 23, no. 4, p. 040901, 2018.

[45] K. Sel, B. Ibrahim, and R. Jafari, "ImpediBands: Body Coupled Bio-Impedance Patches for Physiological Sensing Proof of Concept," *IEEE Transactions on Biomedical Circuits and Systems,* 2020.

[46] M. Ring, C. Lohmueller, M. Rauh, and B. M. Eskofier, "A Two-Stage Regression Using Bioimpedance and Temperature for Hydration Assessment During Sports," in *2014 22nd International Conference on Pattern Recognition*, 2014: IEEE, pp. 4519-4524.

[47] B. Ibrahim, D. Mrugala, and R. Jafari, "Effects of Bio-Impedance Sensor Placement Relative to the Arterial Sites for Capturing Hemodynamic Parameters," in *2019 41st Annual International Conference of the IEEE Engineering in Medicine and Biology Society (EMBC)*, 2019: IEEE, pp. 6569-6573.

[48] W. Wang, M. Tang, M. McCormick, and X. Dong, "Preliminary results from an EIT breast imaging simulation system," *Physiological Measurement,* vol. 22, pp. 39-48, 2001, doi: 10.1088/0967-3334/22/1/306.

[49] A. Tizzard, L. Horesh, R. J. Yerworth, D. S. Holder, and R. H. Bayford, "Generating accurate finite element meshes for the forward model of the human head in EIT," *Physiological Measurement,* vol. 26, no. 2, pp. S251-S261, 2005/03/30 2005, doi: 10.1088/0967-3334/26/2/024.

[50] P. Kauppinen, J. Hyttinen, and J. Malmivuo, "Sensitivity Distribution Simulations of Impedance Tomography Electrode Combinations," *International Journal of Bioelectromagnetism,* vol. 7, pp. 344-347, 2005.

[51] R. Abdelbaset, M. El Dosoky, and M. T. El-Wakad, "The effect of heart pulsatile on the measurement of artery bioimpedance," *Journal of Electrical Bioimpedance,* vol. 8, no. 1, pp. 101-106, 2019.

[52] O. P. Gandhi, J. F. Deford, and H. Kanai, "Impedence Method for Calculation of Power Deposition Patterns in Magnetically Induced Hyperthermia," *IEEE Transactions on Biomedical Engineering,* vol. BME-31, no. 10, pp. 644-651, 1984.

[53] M. Eberdt, P. K. Brown, and G. Lazzi, "Two-Dimensional SPICE-Linked Multiresolution Impedance Method for Low-Frequency Electromagnetic Interactions," *IEEE Transactions on Biomedical Engineering,* vol. 50, pp. 881-889, 2003, doi: 10.1109/TBME.2003.813534.

[54] C. Dimas, N. Uzunoglu, and P. P. Sotiriadis, "A Parametric EIT System Spice Simulation with Phantom Equivalent Circuits," *Technologies,* vol. 8, no. 1, p. 13, 2020.

[55] M. Kejarwal, K. Kaster, J. Jurist, and J. Pakanati, "Breast cancer detection using electrical impedance tomography: spice simulation," presented at the Proceedings of the Annual Conference on Engineering in Medicine and Biology, 1993.

[56] A. Morimoto, E. Yasuno, Y. Kinouchi, Y. Ohmine, A. Tangoku, and T. Morimoto, "Spatial resolution in the electrical impedance tomography for the local tissue," in *2005 IEEE Engineering in Medicine and Biology 27th Annual Conference*, 2006: IEEE, pp. 6638-6641.

[57] T. Dai and A. Adler, "Blood impedance characterization from pulsatile measurements," presented at the Canadian Conference on Electrical and Computer Engineering, 2006.

[58] Y. M. Chi, T.-P. Jung, and G. Cauwenberghs, "Dry-contact and noncontact biopotential electrodes: Methodological review," *IEEE reviews in biomedical engineering,* vol. 3, pp. 106-119, 2010.

[59] J. U. Kim, Y. J. Lee, J. Lee, and J. Y. Kim, "Differences in the properties of the radial artery between Cun, Guan, Chi, and nearby segments using ultrasonographic imaging: a pilot study on arterial depth, diameter, and blood flow," *Evidence-Based Complementary and Alternative Medicine,* vol. 2015, 2015.

[60] A. Tonks, J. Lawrence, and M. Lovie, "Comparison of ulnar and radial arterial blood-flow at the wrist," *The Journal of Hand Surgery: British & European Volume,* vol. 20, no. 2, pp. 240-242, 1995.

[61] E. Kazanavicius, R. Gircys, A. Vrubliauskas, and S. Lugin, "Mathematical methods for determining the foot point of the arterial pulse wave and evaluation of proposed methods," *Information Technology and control,* vol. 34, no. 1, 2005.

[62] D. Hughes, C. F. Babbs, L. Geddes, and J. Bourland, "Measurements of Young's modulus of elasticity of the canine aorta with ultrasound," *Ultrasonic Imaging,* vol. 1, no. 4, pp. 356-367, 1979.

[63] M. Elengdi, "On the analysis of fingertip photo plethysmogram signal," *Current cardiology reviews,* pp. 14-25, 2012.

[64] Finapres.com. "FMS Finapres Medical Systems. The Finapres NOVA has received 510(k) clearance from the US FDA!, 2017." www.finapres.com

[65] J. Maver, M. Strucl, and R. Accetto, "Autonomic nervous system activity in normotensive subjects with a family history of hypertension," *Clinical Autonomic Research,* vol. 14, no. 6, pp. 369-375, 2004.

[66] H. J. Timmers, J. M. Karemaker, W. Wieling, H. A. Marres, H. T. Folgering, and J. W. Lenders, "Baroreflex and chemoreflex function after bilateral carotid body tumor resection," *Journal of hypertension,* vol. 21, no. 3, pp. 591-599, 2003.

[67] A. Voss, R. Schroeder, S. Truebner, M. Goernig, H. R. Figulla, and A. Schirdewan, "Comparison of nonlinear methods symbolic dynamics, detrended fluctuation, and Poincare plot analysis in risk stratification in patients with dilated cardiomyopathy," *Chaos: An Interdisciplinary Journal of Nonlinear Science,* vol. 17, no. 1, p. 015120, 2007.

[68] T. R. Dawber, H. E. THomas Jr, and P. M. McNamara, "Characteristics of the dicrotic notch of the arterial pulse wave in coronary heart disease," *Angiology,* vol. 24, no. 4, pp. 244-255, 1973.

[69] P. Su, X.-R. Ding, Y.-T. Zhang, J. Liu, F. Miao, and N. Zhao, "Long-term blood pressure prediction with deep recurrent neural networks," in *2018 IEEE EMBS International Conference on Biomedical & Health Informatics (BHI)*, 2018: IEEE, pp. 323-328.

[70] B. Ibrahim, J. McMurray, and R. Jafari, "A Wrist-Worn Strap with an Array of Electrodes for Robust Physiological Sensing," in *2018 40th Annual International*

Conference of the IEEE Engineering in Medicine and Biology Society (EMBC), 2018, pp. 4313-4317.

[71] E. O'brien, B. Waeber, G. Parati, J. Staessen, and M. G. Myers, "Blood pressure measuring devices: recommendations of the European Society of Hypertension," *Bmj,* vol. 322, no. 7285, pp. 531-536, 2001.